EXPLORING THE TUNABILITY OF MARTENSITIC TRANSFORMATION IN SHAPE MEMORY ALLOYS VIA COHERENT SECOND PHASE

by

Shivam Tripathi

A Dissertation

Submitted to the Faculty of Purdue University

In Partial Fulfillment of the Requirements for the degree of

Doctor of Philosophy

School of Materials Engineering

West Lafayette, Indiana

December 2021

THE PURDUE UNIVERSITY GRADUATE SCHOOL
STATEMENT OF COMMITTEE APPROVAL

Dr. Alejandro Strachan, Co-Chair

School of Materials Engineering

Dr. Michael S. Titus, Co-Chair

School of Materials Engineering

Dr. David F. Bahr

School of Materials Engineering

Dr. Maria Okuniewski

School of Materials Engineering

Approved by:

Dr. David F. Bahr

Dedicated to my parents and brothers for their unconditional love, support and encouragement

ACKNOWLEDGMENTS

First, I would like to thank my advisors Prof. Alejandro Strachan and Prof. Michael Titus, for their encouragement, support and guidance in matters both personal and professional during my time at Purdue University. Your knowledge, ideas, advice, attention, and encouragement has been invaluable. I am extremely fortunate to have you as my first professional mentors, and you have made me a better researcher and a person. I would also like to thank my committee members Prof. David F. Bahr and Prof. Maria Okuniewski for their time and advice.

Thank you to my mentors MD Mahbubul Islam, David Guzman, Sam Reeve, and Karthik Guda Vishnu for holding my hand through a diffcult transition from student to researcher, and instilling a core set of principles that have proven invaluable to me over time. I would specially like to thank Karthik Guda Vishnu and Saaketh Desai for all the insightful discussions throughout my PhD, we made a wonderful team. Thank you to Strachan and Titus group members Brenden W Hamilton, Michael Sakano, Sae Matsunaga, Zacary McClure, Saswat Mishra, Juan Carlos Verduzco, Shukai Yao, Thomas Mann and Ching-chien Chen for their constant support and help. I am hoping to continue to work with you all throughout my professional career.

A big thank you to my friends Shubhra Paliwal, Pekham Dey, Saaketh Desai, Shikhar Mishra, Ankit Patel, Saswat Mishra, Saumya Sangoi, Sri Tapaswi Nori, Shayani Parida, and Sasmita Rout. You all were there to support me through the good times and bad. I could not have asked for a better peer group and support system.

Lastly, I would also like to take this opportunity to express my undying gratitude to my parents and my brothers for their constant love and support. You are a pillar of strength to me and your unending love and support helped me maintain balance.

TABLE OF CONTENTS

LIST OF TABLES

LIST OF FIGURES

ABSTRACT

Shape memory alloys (SMAs) belong to an important class of active materials. Beyond shape memory, these alloys exhibit super-elasticity and pseudo-plasticity, all originating from a reversible phase transformation from a high-temperature austenitic phase to a low temperature martensitic phase. Their unique thermo-mechanical properties make these SMAs desirable for a wide range of applications in automobiles, robotics, aerospace, construction, and medicine. Only a fraction of the known metallic alloys exhibits martensitic transformations, and a relatively small subset exhibits shape memory. Given this limited pool of SMAs, tunability of this martensitic transformation and, hence, thermo-mechanical properties is a way to move forward for effectively designing the next-generation SMAs for specific applications. The modification in composition has always been at the heart of designing new SMAs for future applications. However, a relatively recent discovery of incorporating a second non-transforming phase in base martensitic materials to tune martensitic transformation to achieve unprecedented thermo-mechanical properties has shown great promise.

The objective of this work is to utilize the second phase to provide design guidelines for next-generation SMAs and to understand the detailed physics behind the experimentally observed unprecedented thermo-mechanical properties in SMAs as a result of the incorporation of coherent second phases. We first investigate Mg-Sc shape memory alloys that are attractive for a wide range of applications due to their low density. Unfortunately, the use of these alloys is hindered by a low martensitic transformation temperature (173 K). We observe from first-principles calculations that epitaxial strains arising from appropriate substrate or coherent second phase selection increase the martensitic transformation and operational temperature to room temperature. Next, we develop a novel approach to induce martensitic transformation in composite systems of two non-transforming materials. While we demonstrate this approach for the technologically relevant ultra-lightweight Mg/MgLi superlattices, however, our approach is general and will open a wide material space for the discovery and design of next-generation SMAs.

Finally, to bridge the gap between computationally studied single-crystalline materials and experimentally studied polycrystalline systems, we characterize the role of nanoscale pre-

cipitates on temperature- and stress-induced martensitic phase transformation in nanocrystalline $Ni_{63}Al_{37}$ SMAs using multi-million-atoms molecular dynamics simulations. Simulations provide the understanding of underlying atomistic mechanisms of experimentally observed unprecedented thermo-mechanical properties and the guidelines to design low-fatigue ultra-fine grain shape memory alloys. As a result of the exploration of novel thermomechanical properties in SMAs via coherent second phases, we also published a software package to discover coherent precipitates within a base multi-component system by coupling high-throughput equilibrium thermodynamics calculations with strain-based lattice matching.

1. INTRODUCTION

SMAs undergo reversible solid to solid phase transformation between high-temperature, high-symmetry phase (austenite) to low-temperature, low-symmetry phase (martensite), aka reversible martensitic transformation [1]. This reversible martensitic transformation can be induced via temperature and stress and is an underlying reason behind unique properties like shape-memory behavior, superelasticity , and pseudoplasticity. Importantly, this transformation occurs without atomic diffusion and is driven by the change in crystal shape and atomic shuffling. For martensitic transformation to be reversible, the space group of the martensite phase should be the sub-group of the space group of the austenite phase, which ensures that all variants of martensite transform to single austenite [2]. Consider an SMA in the high-temperature austenite phase; upon cooling, the material starts to transform to martensite phase at a martensitic start temperature (M_s), and temperature-induced transformation completes at a martensite finish temperature (M_f). Any mechanical deformation in the martensite phase below a critical limit for plastic deformation results in shape change via twin boundary motion, known as pseudoplasticity. The subsequent heating of this deformed structure starts to transform it back to austenite above austenite start temperature (A_s), and heating above austenite finish temperature (A_f) results in complete austenitic transformation and recovery of the original shape, known as shape-memory behavior. During mechanical loading in the austenite phase, stress-induced martensitic transformation starts above martensitic start stress (σ_{M_s}) and upon unloading, the material transforms back to austenite below austenite finish stress (σ_{A_f}) and recovers its original shape, this stress-induced martensitic transformation significantly reduces the permanent deformation for relatively high strains, and this phenomenon is known as superelasticity. Figure 1.1 shows the relationship between SM and SE for SMAs.

These unique thermo-mechanical properties of SMAs make them attractive for a wide range of applications in medicine [4], construction [5], micro-electro-mechanical systems (MEMS) [6], [7], automobile [8], and aerospace engineering [9]. For example, SMAs are used in the medicine industry as orthopedic bio-implants, artificial stents to prevent clogging of heart valves [10], see Figure 1.2 (a). They are being used as transmission valves

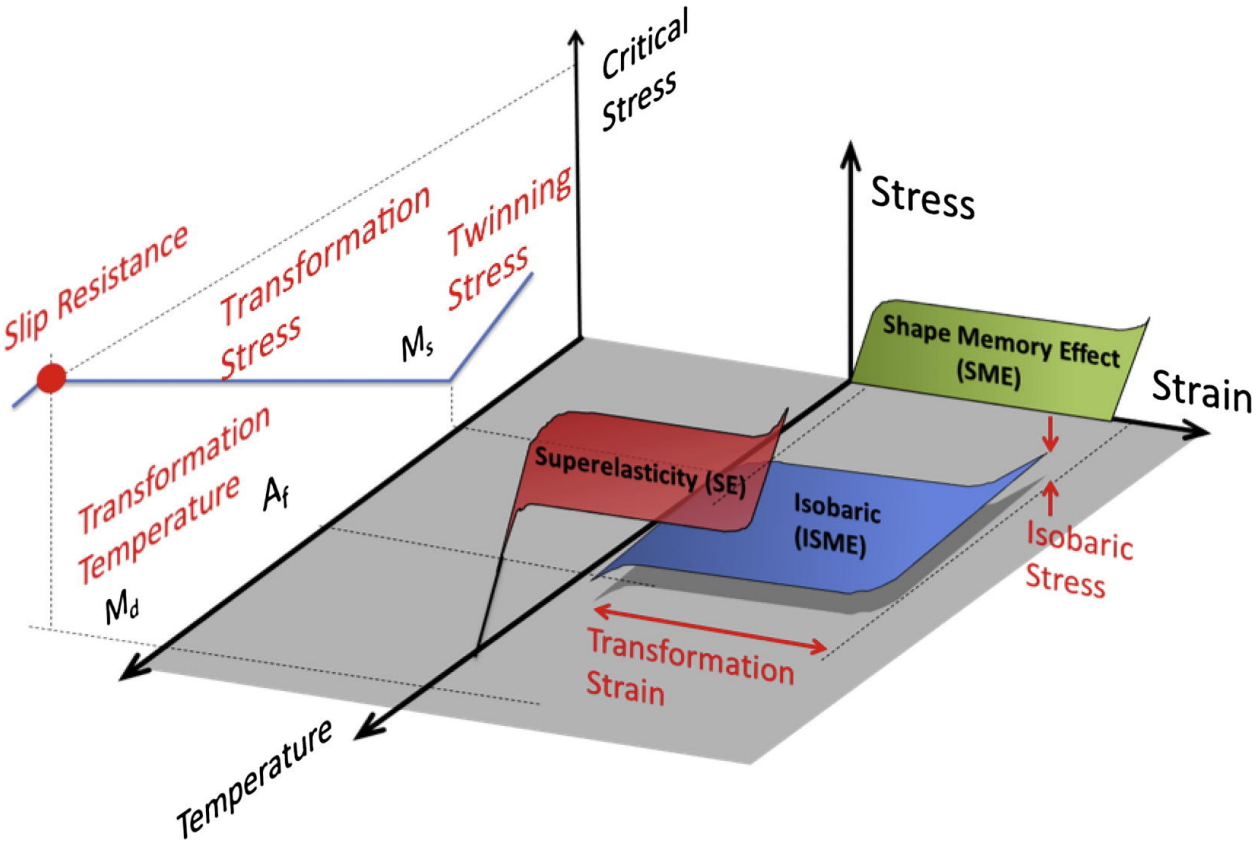

Figure 1.1. Schematic of martensitic behavior in a typical shape memory alloy (SMA). Taken from H. Sehitoglu, L. Patriarca, and Y. Wu, "Shape memory strains and temperatures in the extreme", Curr. Opin. Solid State Mater. Sci., vol. 21, pp. 113-120, 2017 [3], with permission from Elsevier.

in automobiles [11], see Figure 1.2 (b). Recently, NASA has shown that Ni-Ti-Hf based SMAs can be used for wing-flapping in aircrafts and that is expected to reduce weight by 80% compared to traditional mechanical assembly used for same purpose [12], see Figure 1.2 (c). SMAs are also being considered for tires of space rovers, and their superelasticity will prevent significant wear and tear originating from the uneven planetary surface compared to currently used Al-based tires [13], see Figure 1.2 (d). The global market size of SMAs is multi-billion dollars and growing rapidly [14]. Figure 1.3 shows the market growth of SMAs in the united states (U.S) over the years.

The application of SMAs is mainly based on two broad categories i) thermal memory and ii) mechanical memory. The thermal memory behavior originates from temperature-induced transformation and is used for actuator and coupling applications [10], [15], [16]. For these applications, the material's M_f should be higher than the working temperature. Mechanical deformation in the martensite phase at working temperature results in reorientation and growth of favorable martensite variants. The material remains in deformed shape even after removal of load; however, after subsequent heating of this deformed material above A_f, all martensite variants transform back to single austenite, and the material recovers its original shape. In the other class of applications where mechanical memory via superelasticity is harnessed, the working temperatures should be higher than A_f. On loading, the material undergoes stress-induced transformation to favorably oriented martensite variants and recovers its original shape after unloading. These applications include highly flexible components in medicine and engineering [10], [17] and typically require SMAs with a high superelasticity range. Hence, depending on the application and working temperature, a specific set of thermo-mechanical properties is needed. Figure 1.4 compares the various thermo-mechanical properties like M_s, superelasticity, thermal-hysteresis, and specific weight of some common SMAs [18]–[24]. Tuning of the underlying martensitic transformation undergirds the design of next-generation SMAs for specific applications. Composition modification via the addition of alloying elements and the change in processing conditions to tune microstructure has always been at the heart of designing new SMAs. The other powerful avenue to tune the properties of shape memory materials is the introduction of engineered second phases; these are known to strongly affect the martensitic transformation and, hence, thermo-mechanical

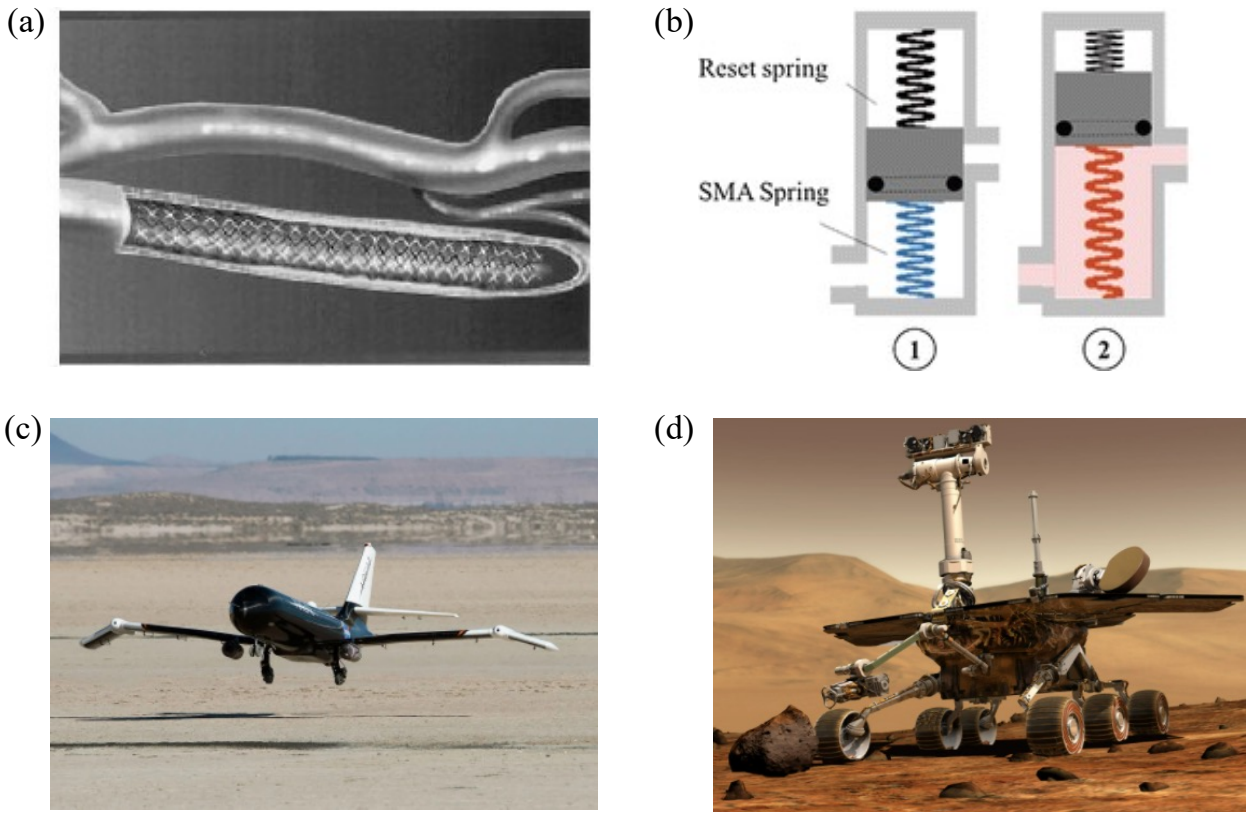

Figure 1.2. Applications of shape memory alloys (SMAs) (a) as an artificial stent in the medical industry (taken from Duerig, T., A. Pelton, and D. J. M. S. Stöckel."An overview of nitinol medical applications." Materials Science and Engineering: A 273 (1999): 149-160 [10] , with permission from Elsevier), (b) as transmission valves in automobiles (taken from Langbein, Sven, and Alexander Czechowicz. "Introduction to Shape Memory Alloy Actuators." Shape Memory Alloy Valves. Springer, Cham, 2015. 41-72. [11], with permission from Springer), (c) for wing-flapping in aircraft (taken from https://www.wired.com/story/how-nasa-tests-shapeshifting-plane-wings/ [12]), and (d) as tires for space rovers (taken from https://mars.nasa.gov/resources/3904/artists-concept-of-rover-on-mars/ [13])

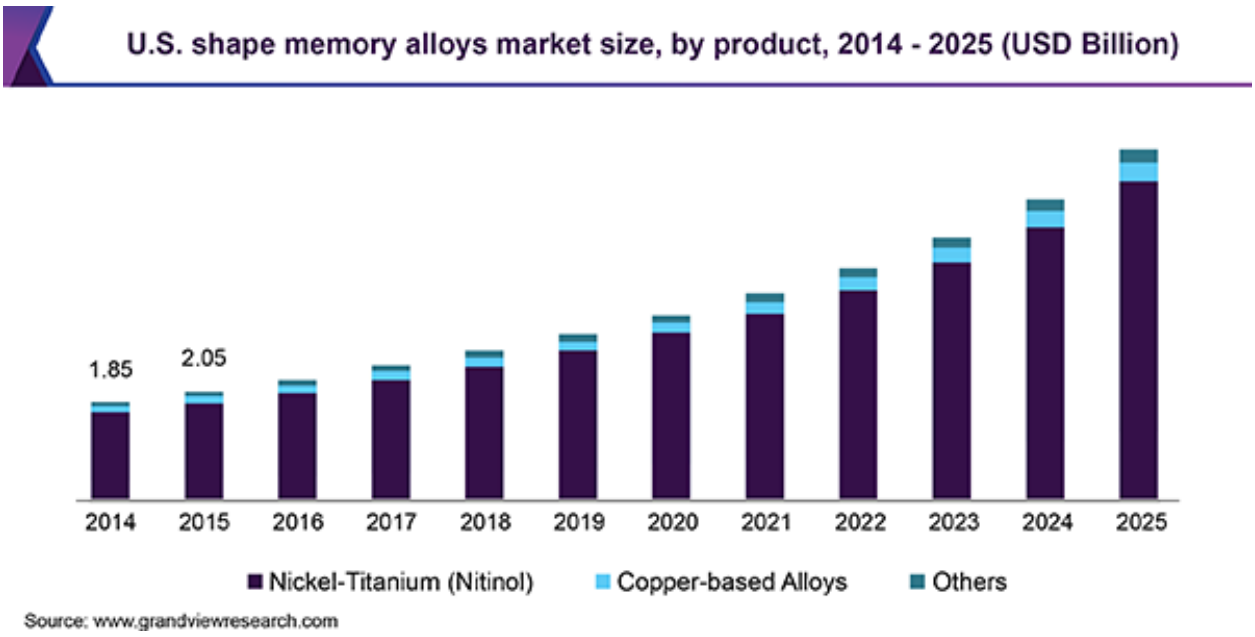

Figure 1.3. U.S shape memory alloys (SMAs) market size, by product, 2014-2025 (USD billions). Taken from https://www.grandviewresearch.com/industry-analysis/shape-memory-alloys-market [14]

properties. Section 1.1 and 1.2 discuss the effect of composition modification and coherent second phase on martensitic transformation in SMAs.

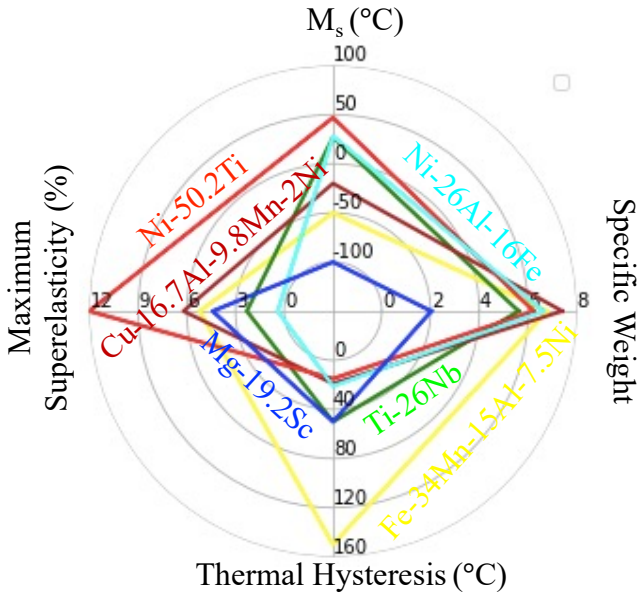

Figure 1.4. Comparison of M_s, superelasticity, thermal hysteresis, and specific weight for various SMAs. The values are taken from Ref. [18]–[24].

1.1 Tuning martensitic transformation via composition modification

Shape-memory behavior was first discovered in Au-Cd based alloy by Ölander et al. [25] but was not interpreted. The interest in these materials grew significantly after the discovery of the shape-memory effect in Ni-Ti alloys [26], [27]. Since then, various SMAs have been discovered. However, among the SMAs, the Ni-Ti alloys are still the most attractive and popular ones owing to their superior strength, ductility, bio-compatibility, and stability of transformation temperature [28]. NiTi undergoes a martensitic transformation from B2 austenite to B19' martensite. Rhombohedral R-phase and orthorhombic B19 are also observed as intermediate phases. As discussed earlier, the required thermo-mechanical properties of SMAs depend on the particular application. Thus, tuning the martensitic transformation of existing SMAs and understanding the underlying physics is of utmost importance and has been the focus for years. Wang et al. [27] first observed in 1965 that

the slight change in composition (50 to 51.2 at.% Ni) for binary Ni-Ti alloys alters the M_s temperature (339 to 211 K) significantly. The further studies correlated this change with elastic constants [29], [30], number of valence electrons [31], [32], magnetic effects [33], [34], point defects [35], the formation of intermediate phases [36], [37] and the latent heat of transformation [38]. Although not a single phenomenon captures the change in transformation temperature and it is a collective effect, however, this observation opened the door for tuning the characteristics of martensitic transformation by changing the relative composition in the binary alloy as well as adding the alloying elements. Frenzel et al. [38] provided the systematic study on the effect of concentration on martensitic transformation temperature in Ni-Ti, Ni-Ti-X (X = Cr, Cu, Hf, Pd, V, Zr), and Ni-Ti-Cu-Y (Y = Co, Pd). They found that the substitution of Ti by Cr or V significantly reduces the transformation temperature, and a similar but less pronounced effect was observed for Cu substitution on Ni sites. The addition of Hf, Pd, and Zr in place of Ti was found to increase the transformation temperature. While Ni substitution by Co in Ni-Ti-Cu alloy reduced the Ms, substitution by Pd was found to have a negligible effect in the same alloy system. The underlying physics behind these trends is not completely understood; nonetheless, these observations give the flexibility to design alloys according to required transformation temperatures for a particular application.

In temperature-induced transformation, SMAs also show thermal hysteresis, which originates from latent heat during transformation resulting in different values of martensite transformation temperatures during cooling and austenite transformation temperatures during heating. SMAs typically shows the two-well free energy landscape. At high temperatures, austenite is lower in energy, and while cooling, their energy becomes equal at some point, and a further reduction in temperature stabilizes the martensite, see Figure 1.5. To transform the material from austenite to martensite phase, undercooling is required to overcome the transformation barrier, compared to a temperature where the free energies of these phases are equal. Similarly, overheating is required during the reverse transformation from martensite to austenite, and as a result, these materials show thermal hysteresis during heating and cooling cycles. This thermal hysteresis is responsible for the degradation of these materials, aka functional fatigue, during cyclic heating and cooling and limits its lifetime. Several studies have focused on reducing this thermal hysteresis via tuning the martensitic

transformation. The value of thermal hysteresis depends on the geometric compatibility between the austenite and the martensite phase, and it was found to be directly correlated with the middle eigenvalue, λ_2, in deformation stretch tensor [2], [39]. Theoretically, $\lambda_2 = 1$ represents perfect structural compatibility between the phases and is expected to show no thermal hysteresis [2], [39].

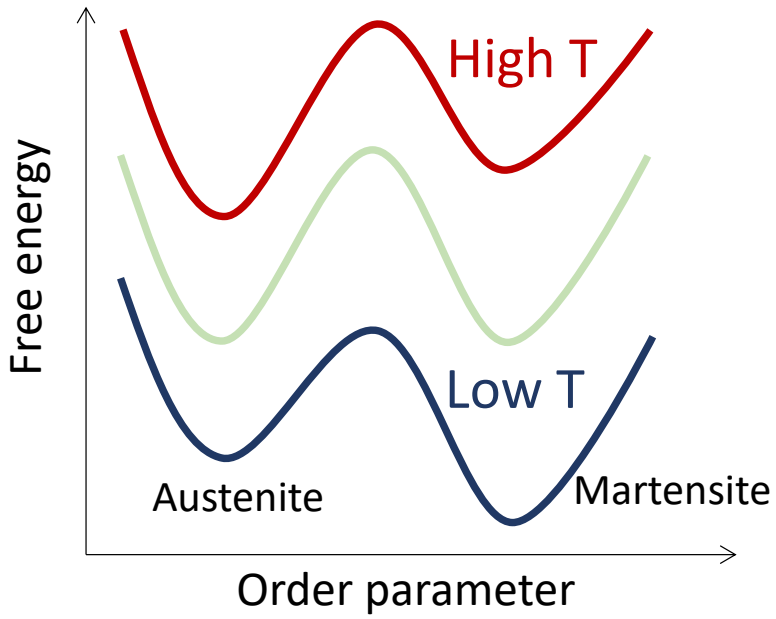

Figure 1.5. Schematic of free energy landscape as a function of temperature for a typical shape memory alloy (SMA)

Cui et al. [40] performed a high-throughput experimental study on Ni-Ti-Cu and Ni-Ti-Pd SMAs to search for SMAs with small thermal hysteresis. They confirmed that the thermal hysteresis is correlated with λ_2 proposed theoretically. They showed that the value of thermal-hysteresis can be tuned between 20 to 60 K by varying the relative composition in both Ni-Ti-Cu and Ni-Ti-Pd alloys. Dezhen et al. [41] used an adaptive design based approach to discover materials with very low thermal hysteresis in Ni-Ti-Cu-Fe-Pd based multi-component system. They combined first-principle calculations, machine learning models, and adaptive experimental design within an active learning setup to explore the design space of 800,000 compositions. $Ni_{46.7}Ti_{50}Cu_{0.8}Fe_{2.3}Pd_{0.2}$ alloy was discovered to have a thermal hysteresis of 1.84 K, which is 97% lower than the binary Ni-Ti alloys.

With growing interest in the application of SMAs in automobile and aerospace applications, designing low-density SMAs has attracted researchers' attention, considering the need for fuel efficiency. To achieve that, the design of porous NiTi [42], [43] and Ti-based SMAs [44], [45] were proposed, however, the reduction in density from these is not significant. Recently, Ogawa et al. [18], [46] discovered the shape-memory effect in Mg-based Mg-Sc alloys for the first time. Their density of these alloys is 1/3 of commercially used Ni-Ti based alloys. While their low density and high work per mass output make them attractive for aerospace and automobile applications, their low transformation temperature of ∼173 K is an obstacle for many applications. They had shown that martensitic transformation temperature can be tuned by varying the relative amount of Sc in the alloy, however, even for the best case, the transformation temperature was within the cryogenic regime. Zhao et al. [47] showed that the martensitic transformation temperature can be increased by doping rare-earth elements like Yb, La, and Gb. They observed Yb, La, and Gb doping increases the transformation temperature by 5, 6, and 18%, respectively, which is still not enough to make their operating temperature close to room temperature. Section 1.2 discusses the use of engineered coherent second phase to tune martensitic transformation in SMAs.

1.2 Tuning martensitic transformation via second phase

The coherent integration of non-transforming martensitic phase in base martensitic material is an another interesting avenue to tune the characteristics of martensitic transformation. This can be achieved by precipitation or creating superlattices between two phases/materials. Within the coherency limit, both the materials are forced to share a common lattice parameter at nanoscale epitaxially. This approach fundamentally depends on tuning the free-energy landscape (FEL) of base martensitic materials having two-well energy landscape. The addition of the non-transforming coherent second phase with single-well FEL or FEL with a small shoulder can significantly alter the FEL of martensitic material in this composite system. As a result, the relative stability between the austenite and martensite phases (correspond to transformation temperature), transformation barrier (correspond to hysteresis), transition order and stiffness of phases can be modified according to need

by choosing the appropriate second phase. Figure 1.6 shows the schematics of FEL engineering to tune transformation temperature, hysteresis, phase transition order and stiffness. A number of experimental and computational studies have shown that the unprecedented thermo-mechanical can be achieved by incorporating a coherent second phase in base martensitic materials. Section 1.2.1 and 1.2.2 discuss the state of the art for these in experimental and computation studies.

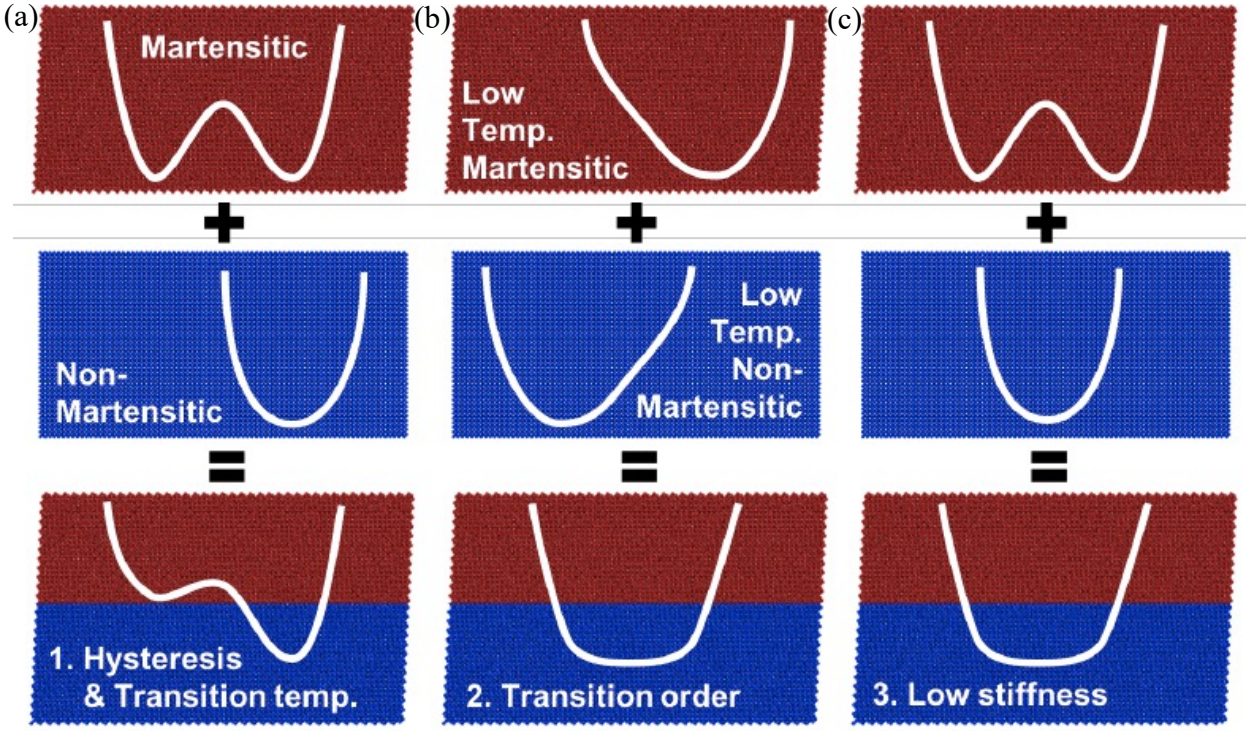

Figure 1.6. Examples of free energy landscape engineering combinations a) hysteresis and transition temperature modification, b) transition order conversion, and c) reduction of stiffness. Taken from Reeve, Samuel Temple. "Materials Design With Molecular Dynamics: Novel Properties in Martensitic Alloys Through Free Energy Landscape Engineering." Diss. Purdue University, 2018 [48].

1.2.1 Experimental Studies

As discussed earlier, the presence of a coherent second phase significantly alter the FEL and tune the characteristics of martensitic transformation. To incorporate the second phase,

superlattices configuration, and precipitation via heat treatment following the traditional metallurgical route are the most common approaches. In superlattices configuration, the only determining factor in altering the martensitic transformation is the modification in FEL in a composite system. However, the precipitation of second phases in material also alters the relative composition of the martensitic matrix along with tuning the FEL, and as discussed in Section 1.1, the slight change in composition can significantly change the characteristics of transformation like transformation temperatures. These two effects can support or compete with each other depending on the relative crystallography of the precipitate and matrix phases. While the modification in FEL only plays a role within the coherency limit, this change in chemistry is prevalent even when the precipitates grow and become incoherent.

Adharapurapu et al. [49] studied the effect of various aging temperatures and times on mechanically induced martensitic transformation by performing compressive stress-strain experiments. They found the precipitates sequence of Ni_4Ti_3 to Ni_3Ti_2 to Ni_3Ti for various aging heat treatments. Ni_4Ti_3 precipitates improved the strength but reduced ductility at an aging temperature of 500 °C. At an aging temperature of 600 °C, the presence of Ni_4Ti_3 precipitates led to maintaining the high strength for short aging times. However, at longer aging times, Ni_3Ti_2 precipitates started to form, and the amount of Ni_4Ti_3 precipitates decreased, resulting in the reduction of yield strength and improvement in ductility. A combination of Ni_3Ti_2 and Ni_3Ti precipitates at 700 °C resulted in a reduction in yield strength and higher ductility. At 800 °C, the presence of only Ni_3Ti precipitates was found, and their presence led to improvement in both strength and ductility. Meng et al. [50] found the increment in the martensitic transformation temperature due to the presence of $Ni_4(Ti, Hf)_3$ in Ni-Ti-Hf based SMAs. The nucleation of precipitates made the matrix Ni-lean, and this change in chemistry is the leading cause behind the increased transformation temperature. Ni_2TiAl Heusler precipitates increased the strength of Ni-Ti-Al alloys significantly [51], however, these precipitates suppressed the martensitic transformation completely due to the austenite phase stabilization by a change in FEL of the combined system [52]. Hsu et al. [53], [54] studied the effect of Ni_2TiAl Heusler precipitates on martensitic transformation in Ni-Ti-Hf-Al alloys. They found that the presence of Heusler precipitates reduces the transformation temperature for the aging temperature of 600 °C due to the austenite stabilizing behavior of precipitates.

However, at an aging temperature of 800 °C, the effect of reduction of Al content in the matrix dominates, and the transformation temperature was found to be increasing. Wang et al. [55] observed the presence of nanoscale concentration modulation of Nb in Ti-Nb based gum metals. As a result, these materials showed the elastically confined martensitic transformation and a tunable Young's modulus over a wide temperature range. The presence of the ultra-low function fatigue was observed for more than millions of cycles in Ni-Ti-Cu based SMAs due to the presence of Ti_2Cu precipitates [56]. The disordered omega precipitates in $L2_1$ matrix of Ni-Co-Fe-Ga SMAs led to non-hysteretic superelasticity response in these alloys [57]. They also found the transformation to be a continuous second-order type rather than a typical first-order martensitic transformation. Strength and functional fatigue were shown to improve significantly in the crystalline-amorphous nanocomposites of nanocrystalline NiTi due to suppression of transformation-induced dislocations in the crystalline region and shear bands in the amorphous region via mutual strengthening of the two phases in nanolaminates [58]. In addition to these experimental studies, Section 1.2.2 discusses various computational studies showing that the unprecedented thermo-mechanical properties can be achieved by incorporating a coherent second phase in SMAs.

1.2.2 Computational Studies

Computational studies play a huge role in understanding the underlying mechanisms behind experimentally observed novel phenomena and guiding future experiments. Several atomistic studies have characterized the effect of the coherent second phase on martensitic transformation in SMAs with an objective to achieve novel thermo-mechanical properties. Guda Vishnu et al. [59] showed that the hetero-epitaxial integration of non-transforming $Ni_{50}Al_{50}$ and martensitic $Ni_{63}Al_{37}$ in superlattices configuration can significantly tune the thermal hysteresis. $Ni_{63}Al_{37}$ shows a thermal hysteresis of 1200 K in bulk form, and it can be reduced by more than 90% for 50-50 $Ni_{50}Al_{50}/Ni_{63}Al_{37}$. Reeve et al. [60] extended this work to other nanostructure configurations like core/shell nanowires and nanoprecipitates, which can be achieved through standard metallurgical processes. They showed that a similar reduction in hysteresis and tunability of transformation temperatures can also be achieved

in these configurations. Desai et al. [61] provided a more systematic study by varying the characteristics such as lattice mismatch and stiffness of the coherent, nanoscale second phase in an atomistic model system in the molecular dynamics (MD) framework. They showed that the martensitic transformation temperature could be engineered, from 50% reduction to 200% increase in these composite systems compared to base martensitic material. They also illustrated the tunability of hysteresis and transformation strain over a wide range by varying the characteristics of the second phase. Reeve et al. [62] demonstrated the stabilization of a mechanically unstable, negative stiffness state of a martensitic alloy by its coherent integration with a compatible, stable second component. As a result, they achieved a very flat FEL in the epitaxial metamaterials of $Ni_{50}Al_{50}$ and $Ni_{63}Al_{37}$, hence, the ultra-low stiffness of 2 GPa comparable to polymers was found in fully dense nanostructured metals. While martensitic transformation is typically a first-order phase transformation, it has been shown that the epitaxial stress originating from the incorporation of a tailored second phase can modify the free energy landscape that governs the phase transition and change its order from first to second [63]. The continuous evolution of the transformation order parameter was observed in Ni-Al based system using high-fidelity MD simulations.

In addition to these atomistic simulations, many phase-field simulations based studies have also provided the insights behind the tunability of martensitic transformation using coherent second phases or nanoscale concentration modulation (CM). Spinodal decomposition underlies the nanoscale CM, and the specifics of CM can be tailored via adjusting the aging temperatures and times. Zhu et al. [64] systemically studied the effect of the wavelength, amplitude, and statistical distribution of CM on the characteristics of martensitic transformation in Ti-Nb based multifunction alloys using phase-field simulations. While the chemical driving force of martensitic transformation increased linearly with the amplitude of CM, it first increased rapidly, then slowly with an increase in the wavelength of CM. The longer wavelengths were also found to reduce the critical stress and hysteresis associated with mechanically induced martensitic transformation. Zhu et al. [65] also investigated the effect of Ni_4Ti_3 precipitates on martensitic transformation in Ni-rich NiTi alloys. The presence of precipitates led to the Ni concentration gradient in the B2 matrix, and as a result, the first order to more continuous transformation was observed. The effect of H-phase precipitations

on the underlying martensitic transformation in Ni-Ti-Hf based high temperature SMAs was studied by Yu et al. [66]. H-phase was found to be in a diamond shape at smaller sizes and grew to plate-like morphology with increasing size. They investigated the effect of both i) change in matrix chemistry resulting from precipitation and ii) elastic interaction between precipitates and matrix on the characteristics of martensitic transformation. In this alloy system, both the effects favored each other and increased the martensitic transformation temperature. With increasing aging time, the transformation temperature first increased rapidly, then a slight reduction followed by saturation.

In this thesis, we use density functional theory (DFT) and MD simulations to explore the tunability of martensitic transformation in various SMAs. Section 1.3 discusses the outline for the remainder of the thesis.

1.3 Dissertation Outline

The central theme of this thesis is to explore the tunability of martensitic transformation in SMAs by incorporating the non-transforming coherent second phase. The remainder of the document is organized as follows: In chapter 2, a brief description of density functional theory and molecular dynamics is presented. Chapter 3 focuses on characterizing the martensitic transformation in low-density Mg-Sc shape memory alloys. We also provide design guidelines to increase the transformation temperature of these to room or higher temperatures by utilizing epitaxial strains via appropriate substrate or coherent second phase. In chapter 4, a novel approach to induce martensitic transformation in the superlattices of two non-transforming materials is proposed and demonstrated for the first time. Chapter 5 provides a detailed atomistic understanding of the underlying physics behind the ultra-low fatigue observed in SMAs by incorporating a coherent second phase. We characterize the role of precipitates in a nanocrystalline sample via multi-million-atoms molecular dynamics simulations. We answer several persisting open science questions and provide guidelines to design low-fatigue ultra-fine grain SMAs. In chapter 6, an automated approach to discover coherent precipitates in multi-component alloys by incorporating high-throughput equilib-

rium thermodynamic calculations and strain-based lattice matching is discussed. Finally, in chapter 7, a summary has been provided.

2. THEORETICAL BACKGROUND

Computational material science and engineering play an essential role in understanding the experimental results with added control, and it is also utilized to reduce the time, effort, and cost involved in designing new materials. The idea of integrated computational materials engineering (ICME) [67] has attracted widespread attention in both industrial and academic settings for making materials development time and cost efficient. The computational material science methods span over various length and time scales, ranging from electronic structure calculation and MD simulations at the atomic scale, mesoscale methods such as phase-field simulations, and macroscopic scale methods such as Finite Element Methods. Each of these methods provides unique insight into materials phenomena and comes with its own limitations; for example, electronic structure calculation based simulations are more accurate but cannot simulate more than a few hundred atoms due to the restrictions imposed by the current computational infrastructure. MD simulations are used for simulating more than millions of atoms on a regular basis and are useful for predicting high temperature properties, however, their accuracy is limited by the used inter-atomic potential to describe atomic interactions. While retaining control of the underlying assumption, these methods can be instrumental in understanding the underlying materials' physics and chemistry, and their synergy with experiments can save time and cost significantly for next-generation materials development. In this thesis, we use electronic structure calculations within the DFT framework and MD simulations to understand the role of the coherent second phase on the characteristics of martensitic transformation in SMAs and provide design guidelines for lightweight and low-fatigue ultra-fine grain SMAs for future applications. Section 2.1 and section 2.2 provide brief theoretical background for DFT and MD, respectively.

2.1 Density Functional Theory

In quantum mechanics, a group of atoms can be fully described by their wavefunctions (ψ), and the materials' properties can be exactly determined and predicted from the time evolution of the wavefunctions of their constituent atoms. The time evolution of the wave-

function can be determined by solving the time-dependent Schrödinger equation [68], see Eq. 2.1.

$$\iota\hbar\frac{\partial\psi}{\partial t} = H\psi \tag{2.1}$$

Where $\hbar$ comes from Planck's constant, t represents time, and H is the Hamiltonian operator. However, Eq. 2.1 is too complex to solve even with the best supercomputers available in today's time. Hence, we need multiple levels of approximation to determine the materials' properties. In the first level Born-Oppenheimer [69] approximation, the ions can be assumed to move very slowly compared to the electrons due to their heavier masses. The electrons are expected to see a static environment, and they can equilibrate instantaneously with respect to the instantaneous positions of the ions which can be determined classically. Within this approximation, we can get away by solving the following time-independent Schrodinger equation:

$$H\psi = E\psi \tag{2.2}$$

Where E is the total energy of the system. The total H of the system can be described in terms of the kinetic energy of electrons and ions; and the electron-electron, electron-ion, and ion-ion interactions as follows [70]:

$$H_{tot} = \sum_{\mathrm{i}} \frac{P_{\mathrm{i}}^2}{2m_{\mathrm{i}}} + \sum_{\mathrm{j}} \frac{P_{\mathrm{j}}^2}{2M_{\mathrm{j}}} + \sum_{\mathrm{i}<\mathrm{i}'} \frac{\mathrm{e}^2}{|r_{\mathrm{i}} - r_{\mathrm{i}'}|} + \sum_{\mathrm{i,j}} \frac{-Z_{\mathrm{j}}\mathrm{e}^2}{|R_{\mathrm{j}} - R_{\mathrm{i}}|} + \sum_{\mathrm{j}<\mathrm{j}'} \frac{Z_{\mathrm{j}}Z_{\mathrm{j}'}\mathrm{e}^2}{|R_{\mathrm{j}} - R_{\mathrm{j}'}|} \tag{2.3}$$

Where r_{i}, P_{i}, and m_{i} are the position, momentum and mass of the electron; R_{j}, P_{j}, and M_{j} are the position, momentum and mass of the ion; Z_{j} denotes the atomic number and e is the charge of an electron. The exact solution of Eq. 2.2, with such a Hamiltonian, is very complex, and also making physical sense of the many-electron wavefunctions would be next to impossible. Thus, the DFT formalism to predict the system's ground state properties as an alternative to the ab-initio method is proposed. DFT maps the many-electron problem to ground state self-consistent one-particle problem with theoretically an exact solution. At 0 K, many ground state properties of materials like structure, stability, and lattice dynamics

can be calculated directly using DFT. The determination of excited states properties like transport and optical properties requires further approximations like finite-difference and perturbation methods within the DFT framework. Hohenberg and Kohn [71] and later Kohn and Sham [72] postulated and demonstrated that the ground state energy (E(ρ)) of the set of interacting electrons is the functional of ground state electron density ($\rho(r)$). Thus, within Kohn-Sham formalism, a problem of solving the Schrödinger equation for exact Hamiltonian of all electrons in a system of N interacting electrons can be transformed into a problem of solving one-electron Schrödinger equation in a fictitious system of non-interacting electrons that generate the same density as any given system of interacting electrons. This reduces the 3N dimensional problem for the N electrons system to 3 dimensions which, in principle, can be solved exactly. $\rho(r)$ can be defined in terms of Kohn-Sham one-particle orbitals ($\phi(r)$) as follows:

$$\rho(r) = \sum_{\mathrm{i}} \phi_{\mathrm{i}}^{*}(r)\phi_{\mathrm{i}}(r) \tag{2.4}$$

For the system of N electrons, $\rho(r)$ needs to satisfy the following condition:

$$N = \int \rho(r)dr \tag{2.5}$$

The E(ρ) of an interacting electron gas under the influence of an external potential ($v_{ext}(r)$) can be expressed within Kohn-Sham formalism as follows:

$$E(\rho) = \int v_{\mathrm{ext}}(r)\rho(r)dr - \frac{\hbar^2}{2m}\sum_{\mathrm{i}}\int \phi_{\mathrm{i}}^{*}(r)\nabla^2\phi_{\mathrm{i}}(r)dr + \frac{1}{2}\mathrm{e}^2\int\frac{\rho(r)\rho(r')}{|r-r'|}drdr' + E_{XC}(\rho) \tag{2.6}$$

Where the first term represents the potential energy due to interaction between electrons and ions, the second term is the kinetic energy of the non-interacting electrons, the third term represents the potential energy of the electrons, and the fourth term is an exchange and correlation energy which contains the effect of electron-electron interaction on kinetic and potential energies. Eq. 2.6 can be solved by finding the eigenvalues and eigenfunctions of the following self-consistent equation:

$$(-\frac{\hbar^2}{2m}\nabla^2 + \mathrm{e}^2\int\frac{\rho(r')}{|r-r'|}dr' + \frac{\partial E_{XC}}{\partial\rho(r)})\phi_\mathrm{i}(r) = \epsilon_\mathrm{i}\phi_\mathrm{i}(r) \tag{2.7}$$

Given E_{XC}, the exact electron density and ground state energy of the interacting system can be determined by solving Kohn-Sham equations. However, the exact XC functional is still unknown, and only approximations of this functional are currently in use and proven to be quite successful [73]. The local density approximation (LDA) [74] and the generalized gradient approximation (GGA) [75] are the most popular. LDA assumes the exchange-correlation energy to be a function of $\rho(r)$, and GGA considers it to be the function of both $\rho(r)$ and $\nabla\rho(r)$. DFT counts with a massive amount of implementation. The Vienna Ab-Initio Simulation Package (VASP) is used in this thesis to perform DFT simulations.

2.2 Molecular Dynamics

MD simulations are capable of providing atomistic insight into the temporal evolution of a system from a pre-defined initial state and are instrumental in predicting high-temperature excited state properties. The time evolution of all the atoms' positions (r_i) and velocities (v_i) from their t=0 values is determined by solving the classical Newtonian equation of motion for every atom in the system. In classical MD, the time evolution of atomic positions and velocities can be described as:

$$\dot{r_\mathrm{i}} = v_\mathrm{i} \tag{2.8}$$

$$\dot{v_\mathrm{i}} = \frac{F_\mathrm{i}}{m_\mathrm{i}} \tag{2.9}$$

Where the force F_i on an atom originates from its interaction with the rest of the system and can be defined through a potential energy function ϕ as:

$$F_\mathrm{i} = \sum_\mathrm{i}^N -\frac{\partial\phi(r_\mathrm{i})}{\partial r_\mathrm{i}} \tag{2.10}$$

The most accurate avenue to determine the potential energy functional is by solving the time-independent Schrodinger equation, and the approach is known as ab initio molecular dynamics (AIMD). AIMD is highly accurate, however, the computational cost involved in these simulations is enormous and limits its use to a few thousand atoms for a few hundreds of picoseconds. In classical MD, this potential energy functional is derived from the approximate interatomic potentials parameterized from previous experimental properties or properties obtained using quantum mechanical simulations or a combination of both. The central idea of an interatomic potential is to map the local atomic environment based descriptors to the energy of the system and the force acting on each atom. Based on the chosen descriptors and functional form of mapping equations, various types of interatomic potentials have been developed like Lennard-Jones [76], Morse [77], Embedded Atom Method (EAM) [78], Stillinger-Weber (SW) [79], etc. These interatomic potentials remove the need for solving the time-independent Schrodinger equation and reduce the computational cost significantly. Thus, MD simulations for the system with billions of atoms and longer time scales (up to nanoseconds) are performed on a regular basis using these approximate interatomic potentials. AIMD is most often used in cases where accuracy is a primary concern, or the cheaper interatomic potential is not available.

Once the forces on atoms are determined using the interatomic potential, the positions and velocities can be determined at time t by discretizing Newton's second law of motion and obtaining a numerical integration scheme. There are various integration schemes, and they mainly differ in the way the derivatives are approximated. The velocity Verlet scheme is the most common, and the time evolution of position and velocity within this scheme can be written as:

$$v(t + \frac{\Delta t}{2}) = v(t) + \frac{F(r(t))}{m}\frac{\Delta t}{2} \tag{2.11}$$

$$r(t + \Delta t) = r(t) + v(t + \frac{\Delta t}{2})\Delta t \tag{2.12}$$

$$v(t + \Delta t) = v(t + \frac{\Delta t}{2}) + \frac{F(r(t + \Delta t))}{m}\frac{\Delta t}{2} \tag{2.13}$$

Similar to the DFT, MD is also implemented in various simulation packages. In this thesis, we use a Large-scale Atomic/Molecular Massive Parallel Simulator (LAMMPS) for performing MD simulations. We use EAM interatomic potential to describe the interactions, which is discussed in section 2.2.1.

2.2.1 Inter-atomic Potential

The EAM potential was developed by Purja and Mishin [78] and is one of the most widely used interatomic model for metals. In EAM formalism, the local atomic environment is encoded in pairwise terms, containing the set of distances (r_{ij}), and it also includes an additional term for the embedding energy describing the effect of inserting an atom into the electron density of nearby atoms. The functional form of interatomic potential in EAM is as follows:

$$V(r_i) = \frac{1}{2}\sum_{j\neq i}\phi_{ij}(r_{ij}) + F_i(\rho_i) \tag{2.14}$$

$$\rho_i = \sum_{j\neq i} f_j(r_{ij}) \tag{2.15}$$

where ϕ_{ij} is the pairwise potential energy function and F_i is an embedding function that represents the energy required to place an atom into the electron cloud (ρ_i). f_j describes the contribution of the surrounding atoms to the electronic density at the position occupied by atom i. The EAM potential parametrized for NiAl systems is used in this study, and the specific details for this are discussed in Chapter 5.

3. TUNABILITY OF MARTENSITIC TRANSFORMATION IN MAGNESIUM-SCANDIUM SHAPE MEMORY ALLOYS

This chapter was adapted from Shivam Tripathi, Karthik Guda Vishnu, Michael S. Titus, and Alejandro Strachan. "Tunability of martensitic transformation in Mg-Sc shape memory alloys: A DFT study." Acta Materialia 189 (2020): 1-9. Copyright 2020 Elsevier [80].

Mg-Sc SMAs are attractive for a wide range of applications due to their low density. Unfortunately, the use of these alloys is hindered by a low martensitic transformation temperature (173K). We used density functional theory to characterize the energetics associated with the martensitic transformation in a Mg-Sc (19.44 at.% Sc) alloy from a disordered body centered cubic (BCC) austenite to a disordered orthorhombic martensite. The simulations predict lattice parameters and diffraction patterns in good agreement with experiments and the martensite phase to be 11±1 meV/atom lower in energy than austenite at zero temperature, consistent with the low martensitic transformation temperature. A local ordering analysis of various structures revealed the origin of stacking faults in the HCP ordering in the martensite phase. In addition, we explore the effect of epitaxial strain on the relative energy between the two phases with the objective of increasing the martensitic transformation temperature. Compressive strain along [100] and tensile strain along $[0\bar{1}1]$ on the closest packed plane (011) stabilize the martensite phase with respect to austenite. Bi-axial strain between 5 and 7% increases the zero-temperature energy difference between the phases by over 60%. Similar stabilization of the martensite phase can be achieved by the addition of pure Mg as a coherent second phase. Superlattices with 50 at.% Mg result in an energy difference of 18.1 meV/atom between the two phases at zero temperature. These results indicate that coherency strains can be used to increase the martensitic transformation and operation temperature of Mg-Sc alloys to room temperature.

3.1 Introduction

SMAs exhibit shape memory, super-elasticity and pseudo-plasticity, all originating from a reversible phase transformation from a high-temperature austenitic phase to a low-temperature martensitic phase [1]. These unique properties make them attractive for wide

range of applications. Recent work by Ogawa et al. [18], [46] opened the possibility for lightweight Mg-based SMAs. Their low density and high work per mass output make them attractive for applications in aerospace and automobile engineering. They observed shape memory behavior in a Mg-Sc alloy from a disordered BCC austenitic phase to an orthorhombic martensitic phase. However, the measured the transformation temperature of ∼173K for 19.2 at.% Sc is an obstacle for many applications. The authors also found that the further increase in Sc concentration completely suppresses the thermally induced martensitic transformation and only stress induced transformation can be obtained in alloys with 20.5 at.% Sc.

An atomic understanding of the phases and martensitic transformation in Mg-Sc alloys can contribute to our understanding of the potential and limitations of these materials and design composition with improved properties. Natarajan et al. [81] characterized the relative stability of different Mg-Sc phases with BCC, FCC and HCP ordering as a function of temperature and composition using density functional theory (DFT). They found that in alloys with Sc concentration between 12.5 to 25 at.%, the 0 K ground state exhibits HCP ordering and that the Sc atoms prefer a combination of zig-zag and hexagonal arrangement in equilibrium. However, a diffusion-less martensitic transformation from the high-temperature disordered BCC austenite will result in disordered martensite. Ogawa et al. [18] characterized the crystallography of this transformation using x-ray diffraction (XRD), but an atomic level characterization of the austenite, martensite and the transformation pathway between the two is still missing and is the focus of this paper. Here we report on ab initio simulations of the martensitic transformation in a Mg-Sc (19.44 at.% Sc) alloy from a disordered cubic phase to the orthorhombic martensite. The predicted structures are in good agreement with experimental XRD patterns, and the energy difference is consistent with the low transformation temperature.

In addition, we characterize the effect of epitaxial strain on the transformation with the objective of increasing the stability of the martensitic phase and, consequently, the martensite transformation temperature. This is motivated by prior work on metals and ceramics. Choi et al. [82] and Zhang et al. [83] showed that the transformation temperature in ferroelectric materials and the stability of tetragonal phase can be tailored using bi-axial and interfa-

cial strain, respectively. Molecular dynamics simulations demonstrated that the interfacial strain caused by coherent second phases can have an important effect on the martensitic transformation and associated properties in metallic alloys. Early work showed the possibility of controlling transformation temperature and thermal hysteresis in superlattice or nanolaminate configurations [59], and later work explored the effect of nanostructure [60]. Reeve et al. [62] also found that the ultra-low stiffness (as low as 2GPa) can be achieved in a composite of $Ni_{50}Al_{50}$ and $Ni_{63}Al_{37}$ organized in core/shell nanowires and nanolaminates configurations. In addition, various experimental investigations have also revealed that a coherent second phase can profoundly affect the shape memory behavior in Ni-Ti-Cu and Ti-Nb based alloys [55], [56]. For example, Chluba et al. [56] showed that the coherent precipitates of Ti_2Cu leads to ultralow fatigue in Ni-Ti-Cu based shape memory alloy, and an elastically confined martensitic transformation was observed in Ti-Nb based alloy as a result of nanoscale concentration modulation [55].

In this paper, we explore the effect of interfacial strain on the energetics associated with the martensitic transformation in a Mg-Sc (19.44 at.% Sc) alloy. Biaxial strain on the closest packed plane $(011)_A$ (6.8% compressive strain along [100] and 5.8% tensile strain along $[0\bar{1}1]$) are shown to increase the zero-temperature energy difference between the phases to 16.9 meV/atom compared to 10.5 meV/atom in bulk. Laminates with a martensite stabilizing phase, pure Mg along the closest pack plane $(011)_A$ also increases this difference to 18.1 meV/atom for 50% pure Mg. These results indicate that an appropriate amount of interfacial strain can increase the zero-temperature energy difference, hence the transformation and operating temperature.

3.2 Simulation and analysis details

3.2.1 Atomistic models and DFT simulation details

We used the VASP [84]–[87] to perform DFT calculations within the generalized gradient approximation of Perdew-Burke-Ernzerhof (PBE) [75]. Projector augmented wave (PAW) pseudopotentials [88], [89] parameterized for PBE with two valence electrons for Mg and three valence electrons for Sc are used. We used 450 eV energy cut off and gaussian

smearing for integrals in the first Brillouin zone with a smearing of $\sigma = 0.05eV$. Gamma-centered 7x5x5 k-mesh for sampling the reciprocal space is used for all the phases. The convergence criterion for electronic and ionic relaxation is used as the energy difference 10^{-4} eV and 10^{-5} eV, respectively. All our calculations were non spin-polarized.

We studied 108 atoms supercells (87 Mg, 21 Sc) of a Mg-Sc binary alloy with 19.44 at.% Sc content. The austenite (A) structure is based on a BCC structure with cell vectors: a=3[100] (x), b=3[0$\bar{1}$1] (y) and c=3[011] (z). The initial cell parameters were: 10.806 Å, 15.282 Å, and 15.282 Å. In order to obtain a chemically disordered structure, we generated two special quasi random structures (denotes as SQS-1 and SQS-2) [90] with identical correlation function values and one pseudo random structure (denoted as Random). Special quasi random structures are generated based on the algorithm developed by Van De Walle et al. [91] and implemented in the ATAT package [92]. The SQS approach is based on matching the pair, triplet, and quadruplet correlation functions with those of the true random structure. Values of correlation functions for our SQS structures, pseudo random and the true random structure are reported in Table 3.1.

Table 3.1. Values of Pairs, Triplet and Quadruplet correlation functions for SQS-1, SQS-2, Random and true random structures

	SQS-1 & SQS-2	**Random**	**True Random**
Pair (1^{st} NN)	0.37037	0.33333	0.37346
Pair (2^{nd} NN)	0.37037	0.35802	0.37346
Triplet	-0.22840	-0.16049	-0.22822
Quadruplet	0.13580	0.03704	0.13947

The orthorhombic martensite (M) structures were obtained from the austenite structures by applying compressive strain along [100] and tensile strain along [0$\bar{1}$1] and [011] as shown experimentally by Ogawa et al. [18]. The initial cell parameters for M were: 9.855 Å, 16.632 Å, and 15.669 Å. Details of relaxation of A and M are discussed in section 3.3.1. We use the energy of bulk relaxed austenite structure of SQS-1 as a reference throughout the paper.

3.2.2 Estimating martensitic transformation temperatures

The martensite transformation temperature can be obtained from first principles by computing the free energy of each phase as a function of temperature. Within the harmonic approximation this requires knowledge of the dispersion curve that can obtained at the DFT level in several ways [93], [94]. However, our main focus is on the stabilization of the martensitic phase and a simple estimate of its impact on transformation temperature will suffice. Thus, to estimate the martensitic transformation temperature from the calculated zero temperature energy difference between the phases, we use the empirical relation proposed in Refs. [95]–[97]:

$$M_S^* = n\frac{E_A - E_M}{k_B} \tag{3.1}$$

Where M_S^* is the martensitic transformation temperature, E_A and E_M denote the energy of austenite and martensite phase at 0 K, k_B is Boltzmann's constant and n is an adjustable proportionality constant of the order of one. Barman et al. [95] proposed this expression based on the correlation between the zero-temperature energy difference between austenite and martensite calculated by DFT and the experimentally measured transformation temperature in Ni-Mn-Ga alloys [98] and TiX alloys (X = Ni, Pd and Pt) [99] with values of n of 0.87 and 0.73, respectively. It was also used for Pt-Y-Ga alloys (Y = Cr, Mn and Fe) [96] and Ga-Mo-X alloys (X = Cr, Mn, Fe, Co and Ni) [97] with n=1 to predict the transformation temperature.

To evaluate the applicability of the expression for the class of materials of interest here, we explore the proportionality constant n for elements that undergo BCC and HCP transformations: Ti, Zr and Hf. We note that the transformation temperature is governed by the energy difference at zero temperature and the entropic stabilization of the austenite phase, associated with the difference in vibrational frequencies between the phases [100]. Thus, the proportionality constant in Eq. 3.1 can be expected to depend of the stiffness of the material. Based on the experimental transformation temperature (1155K for Ti, 1136 K for Zr and 2000K for Hf) [101] and zero-temperature energy difference between the BCC and HCP phases (114 meV/atom for Ti, 84 meV/atom from Zr and 181 K for Hf) [102], the

value of n is found to be 0.87, 1.17 and 0.95 for Ti, Zr and Hf, respectively. These values are, as expected, of the order of unity and, interestingly, they are linearly correlated with bulk moduli (113, 94, and 108 GPa for Ti, Zr and Hf, respectively) [102] as argued above. Figure 3.1 shows the calculated proportionality constant as a function of bulk modulus for system undergoing BCC to HCP phase transformation (Ti, Hf and Zr). We found following linear correlation between bulk modulus (B_0) and proportionality constant (n):

$$n = -0.0154 B_0(GPa) + 2.6088 \tag{3.2}$$

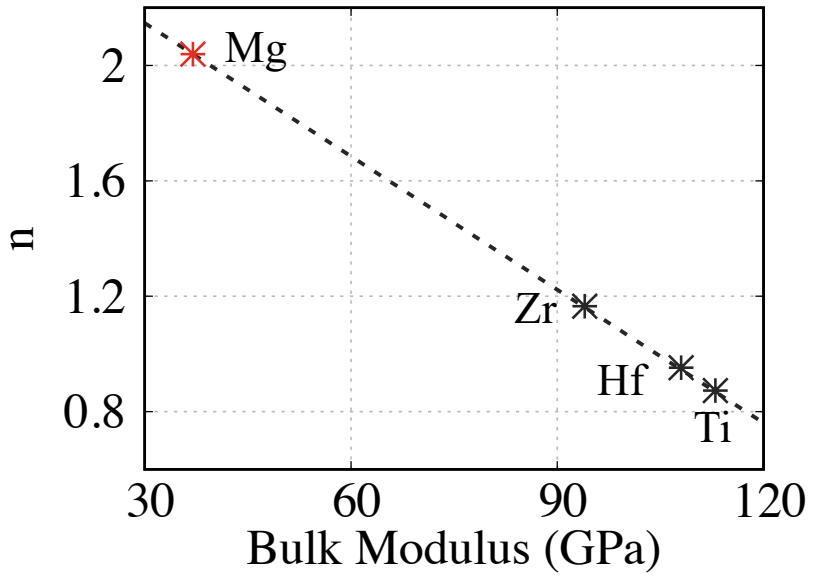

Figure 3.1. Calculated proportionality constant as a function of bulk moduli for Ti, Hf and Zr. Proportionality constant for Mg is predicted based on linear correlation obtained from Ti, Hf and Zr

Based on this linear correlation and bulk modulus (37 GPa) [102], we predict n to be 2.04 for Mg. Using this value and the zero temperature energy difference (39 meV/atom) [102], the transformation temperature for pure Mg is predicted to be 920 K. This high value is consistent with the lack of a BCC phase transformation in experiments up to melting at 923 K.

In the case of our Mg-Sc alloy, we find a proportionality constant n=1.422 using the experimental transformation temperature reported by Ogawa et al. [18] and our energy differences. This value is consistent with the BCC to HCP transformations mentioned above. We stress that Eq. 3.1 is an empirical expression and significant uncertainties are involved, however, it serves our purpose of estimating the change in transformation temperature cause by strain fields.

3.3 Transformation between austenite and martensite phase

3.3.1 structure and energetics of austenite and martensite phases

The high-temperature austenite phase has a BCC structure and we used a tetragonal supercell in our calculation as described in section 3.2.1, see Figure 3.2(a). We obtained the equilibrium structure by minimizing the energy with respect to atomic positions and cell volume. Cell shape (ratios between cell lengths and angles) is held fixed in order to retain cubic symmetry. This is justified since the atomic disorder in the relatively small cell used breaks the cubic symmetry. Ogawa et al. [18] observed that the Mg-Sc binary alloy undergoes a transformation from BCC austenite to orthorhombic martensite with the following lattice correspondence.

$$[100]_A \rightarrow [100]_M, [0\bar{1}1]_A \rightarrow [010]_M, [011]_A \rightarrow [001]_M \tag{3.3}$$

They observed that austenite undergoes 8.8% compression along $[100]_A$ and 9.3% and 2.9% tension along $[0\bar{1}1]_A$ and $[011]_A$, respectively. In addition to the change in shape atomic shuffling on closed-packed 110_A planes completes the transformation. Thus, each of the three $(110)_A$ planes can result in two different martensite variants, resulting in a total of six possible martensite variants for a single austenite. In a bulk disordered structure, these variants should have identical energies and lattice parameters. However, SQS and pseudo randomization cannot generate true random structures in a relatively small supercell which would lead to different formation energy and lattice parameters for these different variants. In order to obtain most stable martensite variant in our calculations, we calculate the energetics of two variants of martensite associated with our tetragonal cell, by interchanging the lattice

parameters along $[011]_A$ and $[0\bar{1}1]_A$ in the description above and followed by full relaxation of structures as discussed in next paragraph.

In order to obtain relaxed martensite structures, we start from the three austenite models, SQS-1, SQS-2, and Random, and deform them to match the experimental martensite lattice parameters. As mentioned above, each austenite results in two martensite variants. Starting from these structures, we performed a full relaxation via energy minimization with respect to atomic positions, cell shape and cell volume. Importantly, the angles remain very close to 90° (less than 0.3° deviation) in relaxed structure which is an artifact of chemical disorder in a relatively small supercell. We fixed the angle to be 90° in the relaxed structure and further preformed relaxation with respect to atomic positions and cell volume and we found the difference in zero-temperature energy to be insignificant (less than 1 meV/atom) as a result of this. We observe that the martensitic transformation is similar in terms of the change in lattice parameter for the three independent austenite structures (SQS-1, SQS-2 and Random) and the resulting six martensite structures, which are all orthorhombic. As will be presented below, these structures are in good agreement with experiments, and the predicted energy difference between the austenite and martensite phases are consistent with the low transformation temperature observed experimentally. Before discussing such results, we address the variability in atomic structures we observe.

Interestingly, both variants originating from SQS-1 exhibit stacking faults while those coming from SQS-2 and Random exhibit ideal ABABAB stacking. For SQS-1, one variant, denoted M1-DS (martensite 1-disordered stacking), exhibits ABACAB stacking along the z direction, and the second one, denoted M2-DS, exhibits ABCBAB stacking along the y direction. For SQS-2 and Random, both variants, denoted M1-OS (martensite 1-ordered stacking), and M2-OS (martensite 2-ordered stacking), respectively, exhibit ABABAB stacking along the z direction and y direction. Snapshots of relaxed structures of austenite and martensites for SQS-1 are shown in Figure 3.2. As is common practice in closed packed systems, we use A, B and C nomenclature to specify the three possible atomic arrangement of each layers normal to <110>. We would like to highlight that the martensite structure is orthorhombic and these layers do not have the six-fold symmetry of the closed packed planes

in HCP or FCC. The relationship between local atomic structures and the energetics of the stacking faults will be discussed in section 3.3.2.

Lattice parameters and energetics of austenite and martensite structures for SQS-1, SQS-2 and Random are reported in Table 3.2. Our lattice parameters are within 3% of experimental lattice parameters which is typical in DFT calculations. We note that transformations leading to ordered or disordered stacking sequences involve nearly identical changes in cell parameters, the only difference being the atomic shuffling on 110_A planes. The energy difference between austenite and the most stable martensite structure for each structure ranges from 10 to 12 meV; as will be discussed in detail in section 3.4.1 these energy differences are consistent with the experimental transformation temperature of 173 K. We note that the dependence of energy difference between phases on the detailed atomic structure is relatively weak; the two SQS and the random structure show a difference of about 20%. This is consistent with previous studies. For example, Jong et al. [103] calculated the energies of planar defects (twin boundaries and stacking faults) for various SQS and random atomic arrangements in Ti-Al systems and they found a variability of 10%.

As mentioned above, the austenite structures have been constrained to remain cubic. We also performed a full relaxation on the SQS-1 austenite structure via energy minimization with respect to atomic positions, cell shape, and cell volume. Unconstrained relaxation of austenite results in another variant of martensite which is 0.3 meV/atom higher in energy compared to M1-DS. The martensite variant obtained from unconstrained relaxation is structurally consistent with our M1-DS and experimental martensite.

In order to further validate our predicted structures, we now compare XRD patterns with experimental results. Since the experimental samples exhibit a coexistence of austenite and martensite, we combined the predicted XRD patterns for the austenite structures with all of the martensites (with equal weights). Figure 3.3 compares the experimental patterns [18] with our results for SQS-1, both ordered and disordered structures. XRD patterns associated with other martensite structures are shown in Figure A.1. The predicted XRD patterns are in good agreement with the experimental XRD pattern at -190 °C reported by Ref. [18]. Interestingly, we observe that staking faults results in the splitting of $(020)_M$ and $(110)_M$ peaks. The predicted peaks are slightly shifted with respect to experiments

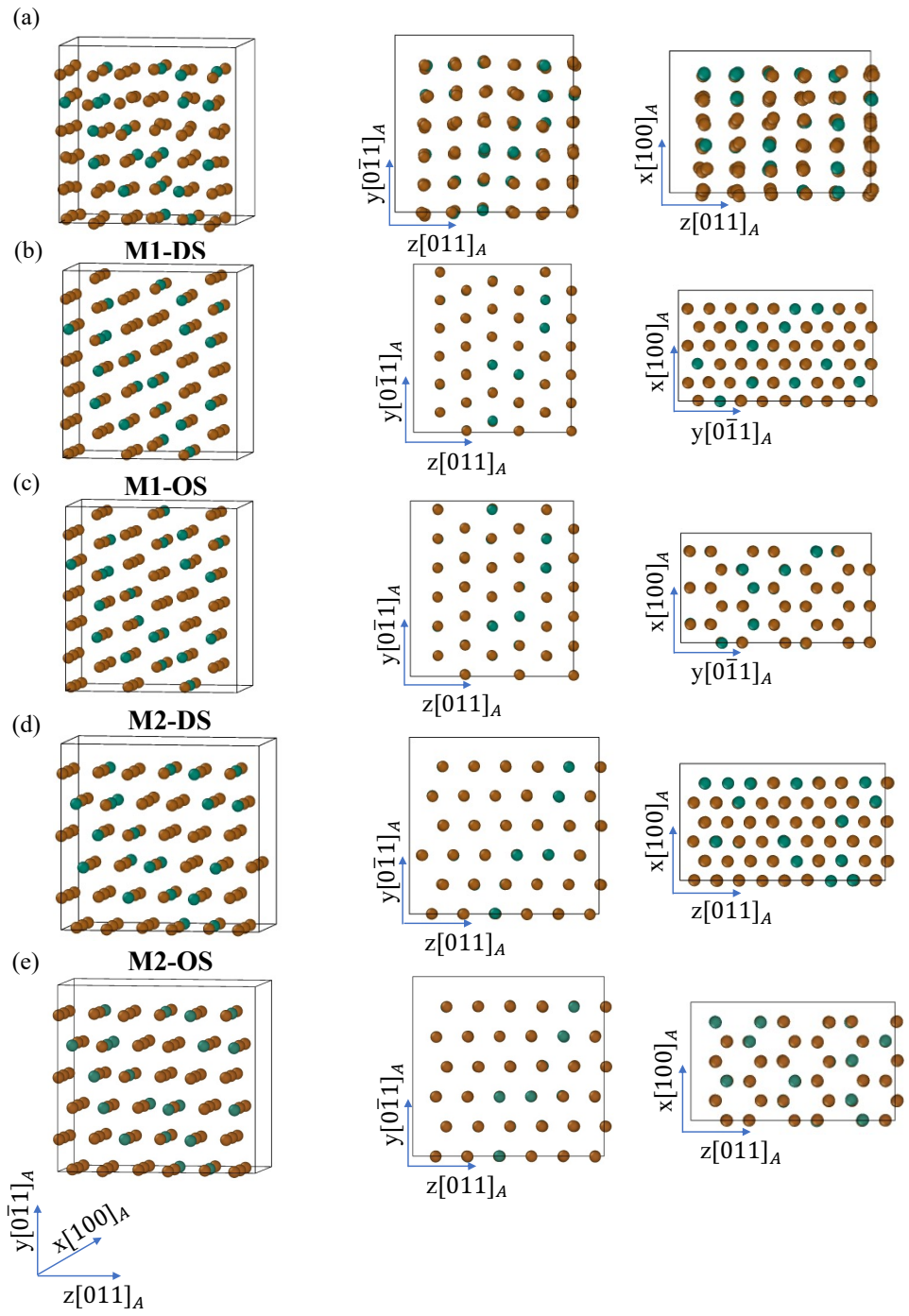

Figure 3.2. Snapshots of relaxed structures of (a) A, (b) M1-DS, (c) M1-OS, (d) M2-DS, and (e) M2-OS for Mg-Sc supercell (3x3x3 unit cells) with 87 atoms of Mg and 21 atoms of Sc (SQS-1). Brown and green colors are used for Mg and Sc atoms, respectively.

Table 3.2. Lattice parameters (Å) of all phases (Austenite (A), Martensite1-disordered stacking (M1-DS), Martensite1-ordered stacking (M1-OS), Martensite2-disordered stacking (M2-DS), Martensite2-ordered stacking (M2-OS)) and relative energy differences (meV/atom) of all martensite phases with respect to austenite

Phases			**a(Å)**	**b(Å)**	**c(Å)**	$\mathbf{E_A - E_M}$ **(meV/atom)**
Austenite	SQS-1	A	3.586	5.072	5.072	_
	SQS-2	A	3.586	5.071	5.071	_
	Random	A	3.585	5.07	5.07	_
	_	Exp.[18]	3.602	5.094	5.094	_
Martensite	SQS-1	M1-DS	3.182	5.564	5.217	10.5
		M1-OS	3.184	5.586	5.2	8.1
		M2-DS	3.189	5.207	5.569	6.5
		M2-OS	3.194	5.203	5.567	6.1
	SQS-2	M1-OS	3.191	5.578	5.2	10.1
		M2-OS	3.207	5.2	5.553	9.9
	Random	M1-OS	3.202	5.563	5.186	12
		M2-OS	3.201	5.216	5.532	7.7
	_	Exp.[18]	3.285	5.544	5.223	_

due to the expected discrepancy in lattice parameters. In order to quantify these shifts, we calculated interplanar distances and corresponding 2θ angles based on our DFT lattice parameters and those obtained experimentally [18] lattice parameters, see Table 3.3. The discrepancy in lattice parameters explain the shifts in the XRD patterns.

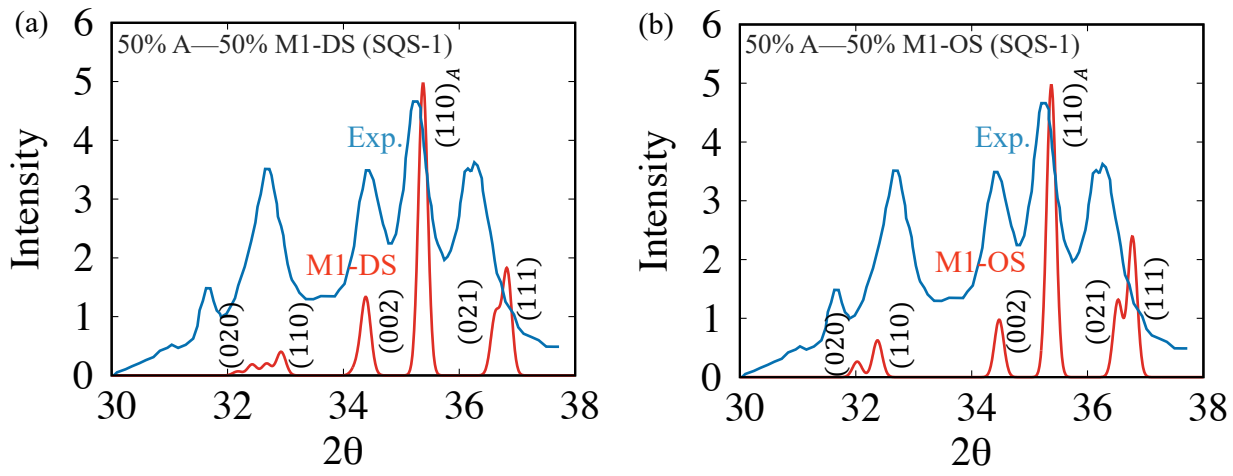

Figure 3.3. XRD pattern for system with 50% A and (a) 50% M1-DS phases and (b) 50% M1-OS phases for SQS-1, where gaussian distribution with standard deviation of 0.08 is used for peak broadening. Blue curve shows XRD pattern from experiments [18] at -190 °C

3.3.2 Thermodynamics of stacking faults in the martensite structure

Our predicted martensite structures are consistent with the ground state HCP structure obtained by Natarajan et al. [81] at 0K. However, martensites obtained by relaxing the austenite structures exhibit disordered stacking for two (SQS-1) out of the six martensites generated. This finding poses the question of whether such disordered stacking sequences represent the ground state or are metastable states trapped during relaxation. In order to address this, we studied the energetics of the M1-DS and M2-DS structures but with no stacking faults (denoted as M1-OS and M2-OS) by shuffling planes to obtain ordered stacking, see Figure 3.2. The cohesive energies of the M1-OS and M2-OS structures in SQS-1 are 8.1 meV/atom and 6.1 meV/atom, respectively. Both values are higher than those corresponding to M1-DS (10.5 meV/atom) and M2-DS (6.5 meV/atom). Thus, for

Table 3.3. Calculated interplanar spacing and 2θ based on experimental and DFT (M1(SQS-1)) lattice parameters

	$\mathbf{d_{hkl,exp.}(\text{Å})}$	$\mathbf{d_{hkl,M1-DS}(\text{Å})}$	$\mathbf{d_{hkl,M1-OS}(\text{Å})}$	$\mathbf{2\theta_{hkl,exp.}}$	$\mathbf{2\theta_{hkl,M1-DS}}$	$\mathbf{2\theta_{hkl,M1-OS}}$
$(020)_{M1}$	2.772	2.782	2.793	32.3°	32.2°	32.0°
$(110)_{M1}$	2.826	2.762	2.766	31.7°	32.4°	32.4°
$(002)_{M1}$	2.612	2.609	2.600	34.3°	34.4°	34.5°
$(021)_{M1}$	2.449	2.455	2.461	36.7°	36.6°	36.5°
$(111)_{M1}$	2.486	2.441	2.442	36.1°	36.8°	36.8°
$(110)_{A}$	2.547	2.536	2.536	35.2°	35.4°	35.4°

this specific atomic structure the stacking fault is energetically favorable. We note that the energy difference between disordered and ordered stacking is relatively small (2.4 meV/atom for M1 and 0.4 meV/atom for M2).

Having established this, we seek to develop physical insight behind the preferred stacking of these structures. More precisely, we seek models capable of correlating the energy of stacking fault formation with the atomic configuration. In order to generate data for this purpose, we systematically created the stacking faults by shuffling every plane of all six martensite structures and followed by full relaxation of these structures. Stacking fault energies (γ) are calculated using following equation:

$$\gamma = \frac{E_{DS} - E_{OS}}{A_{OS}} \tag{3.4}$$

Where E_{DS} and E_{OS} denote the zero-temperature energy of martensite with disordered stacking and ordered stacking, respectively. A_{OS} is the cross-sectional area of martensite exhibiting ordered stacking. A negative stacking fault energy indicates stability of the disordered stacking structure over the ordered stacking structure.

One could hypothesize that the stacking sequence is governed by the ability of layers to pack tightly and, interestingly, we found that the stacking fault energies of martensites with various disordered stacking sequences correlate with equilibrium volume. Figure 3.4 shows the stacking fault energy of the various stacking sequences of all six martensites as a function of equilibrium unit-cell volume. The Figure reveals the general correlation between the equilibrium volume and energy for all of them. This correlation implies that the preferred stacking of each structure is governed by short range interactions driven by the closeness of atomic packing which depends on the equilibrium volume. Of course, the actual energy depends on individual atomic interactions and the volume is a surrogate; this explains the scattering in Figure 3.4.

The model based on atomic volumes provides interesting insight but it has an important drawback: it requires atomistic calculation on the structures involved. We would like to understand stacking fault energies based on the local chemical environments and, thus, we developed a second model. In the martensite, each atom has 12 first nearest neighbors (6 in-

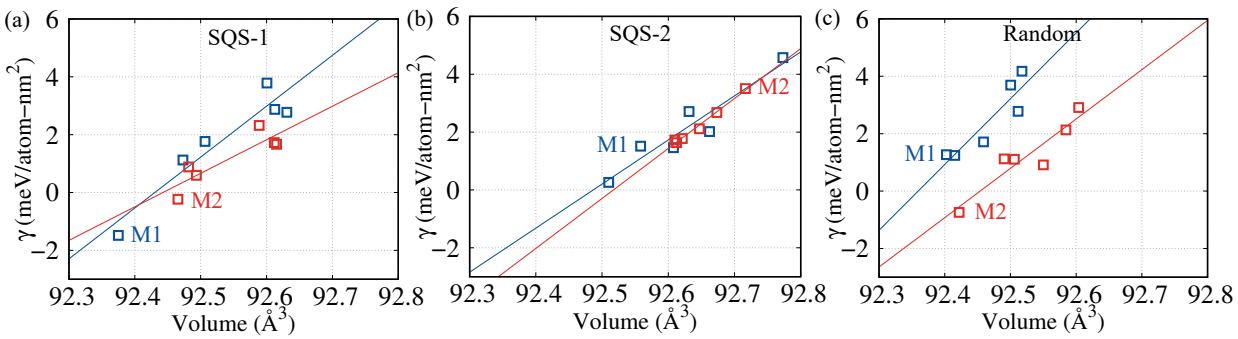

Figure 3.4. Stacking fault energy of martensite with various stacking sequences as a function of their equilibrium unit-cell volume for (a) SQS-1, (b) SQS-2 and (c) Random. Blue and red colors are used for M1 and M2, respectively. Blue and red straight lines show general linear correlation between stacking fault energy and the equilibrium unit-cell volume for M1 and M2, respectively.

plane and 6 out of plane) and the formation of a stacking fault affects only the 6 out-of-plane nearest neighbors of the layers across the fault. The local environment of each atom can be expressed in terms of these six out-of-plane nearest neighbors as the number of Mg and Sc atoms: $Mg_{\mathrm{i}}Sc_{6-\mathrm{i}}$ where i is an integer in a range 0 to 6. We hypothesized that the local energy is a linear function of these descriptors of the local environment. Thus, we express the stacking fault energy γ as the difference in the populations of various environments between the ordered and disordered structures:

$$\begin{aligned}\gamma_{model} = \gamma_{penalty} &+ \sum_{\mathrm{i}=0}^{6}(a_{Mg_{\mathrm{i}}Sc_{6-\mathrm{i}}-DS,Mg} - a_{Mg_{\mathrm{i}}Sc_{6-\mathrm{i}}-OS,Mg})\gamma_{Mg_{\mathrm{i}}Sc_{6-\mathrm{i}},Mg} \\ &+ \sum_{\mathrm{i}=0}^{6}(a_{Mg_{\mathrm{i}}Sc_{6-\mathrm{i}}-DS,Sc} - a_{Mg_{\mathrm{i}}Sc_{6-\mathrm{i}}-OS,Sc})\gamma_{Mg_{\mathrm{i}}Sc_{6-\mathrm{i}},Sc}\end{aligned} \tag{3.5}$$

Where $a_{Mg_{\mathrm{i}}Sc_{6-\mathrm{i}}-DS,Mg}$, $a_{Mg_{\mathrm{i}}Sc_{6-\mathrm{i}}-DS,Mg}$, $a_{Mg_{\mathrm{i}}Sc_{6-\mathrm{i}}-OS,Mg}$, and $a_{Mg_{\mathrm{i}}Sc_{6-\mathrm{i}}-OS,Mg}$, denote the number of Mg and Sc atoms with each possible local environment ($Mg_{\mathrm{i}}Sc_{6-\mathrm{i}}$) environment in M-DS and M-OS, respectively. $\gamma_{penalty}$, $\gamma_{Mg_{\mathrm{i}}Sc_{6-\mathrm{i}},Mg}$ and $\gamma_{Mg_{\mathrm{i}}Sc_{6-\mathrm{i}},Sc}$ are adjustable parameters obtained by linear regression and reported in Table 3.4. Figure 3.5 shows the correlation between the actual and predicted values and the scattering can be attributed to our underlying assumption. In spite of the underlying assumptions, our simple model captures the overall trends across all structures and indicates that the short-range interactions govern stacking fault energies. Such model could be useful in continuum or analytical models of the thermo-mechanical properties of these alloys.

3.3.3 Austenite-martensite transformation path

For formation of specific martensite structures from the austenite depends not only of the thermodynamics of the various variants and stacking sequences but also on the energy barriers associated with the transformation. Thus, we studied the transformation path in SQS-1 between the austenite phase and M1-DS as well as M1-OS to calculate transformation barrier. We chose the M1 variant over M2 due to its lower energy. In order to study transformation pathway, we linearly interpolated the lattice parameters between the phases

Table 3.4. $\gamma_{Mg_iSc_{6-i},Mg}$, $\gamma_{Mg_iSc_{6-i},Sc}$ and $\gamma_{penalty}$ obtained from linear regression of γ_{actual} and $\gamma_{predicted}$. We did not find any atom to have local environment Mg_1Sc_5 and Sc_6 in our structures.

		i = 0	**i = 1**	**i = 2**	**i = 3**	**i = 4**	**i = 5**	**i = 6**
$\gamma_{\mathbf{Mg_iSc_{6-i},Mg}}$ $(\mathbf{meV - atom/nm^2})$	—	-0.15	-0.35	-0.68	-0.05	1.23	—	—
$\gamma_{\mathbf{Mg_iSc_{6-i},Sc}}$ $(\mathbf{meV - atom/nm^2})$	—	-0.45	-1.06	-1.73	-0.14	3.37	—	—
$\gamma_{\mathbf{penalty}}$ $(\mathbf{meV - atom/nm^2})$	1.85	—	—	—	—	—	—	—

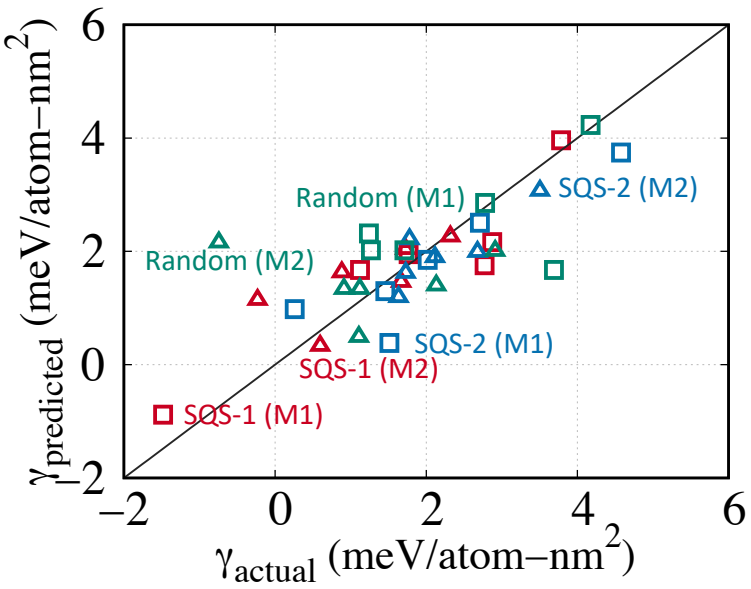

Figure 3.5. Linear correlation between γ_{actual} and $\gamma_{predicted}$. Square and triangle shapes are used for M1 and M2, respectively.

and relaxed the structures with respect to atomic coordinates. The degree of transformation is described by the order parameter λ, which determines the lattice parameter as following:

$$a_\lambda = (1-\lambda)a_A + \lambda a_{M1-DS,M1-OS} \tag{3.6}$$

$$b_\lambda = (1-\lambda)b_A + \lambda b_{M1-DS,M1-OS} \tag{3.7}$$

$$c_\lambda = (1-\lambda)c_A + \lambda c_{M1-DS,M1-OS} \tag{3.8}$$

Figures 3.6(a) and (b) show the transformation pathway between A and M1-DS, A and M1-OS. The transformation barrier between A and M1-DS is 0.8 meV/atom, compared to 1.7 meV/atom for A to M1-OS transformation. Thus, M1-DS is not only the lowest energy structure but also has a lower transformation barrier which suggest that A will prefer to transform to M1-DS phase.

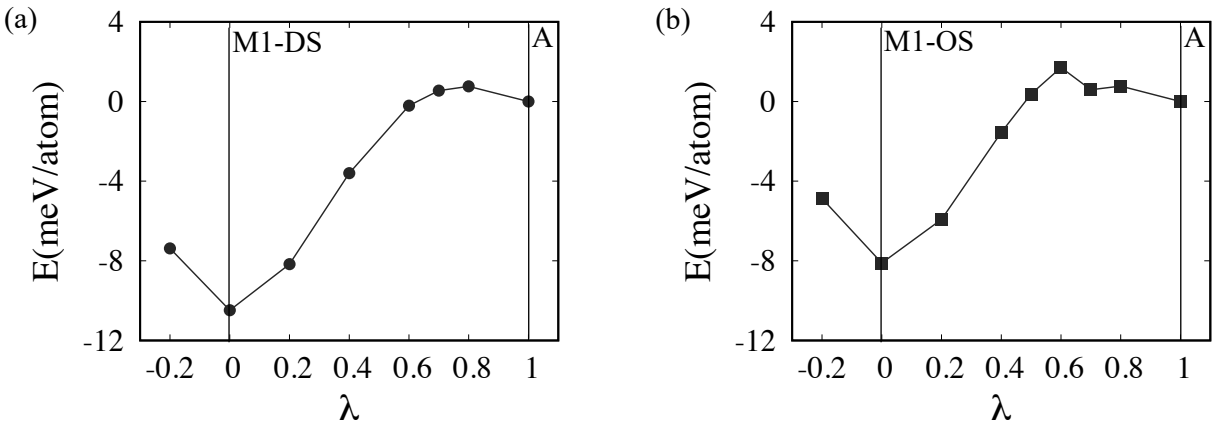

Figure 3.6. Energy of relaxed structure on linear path from martensite to austenite lattice parameters for (a) M1-DS, and (b) M1-OS of SQS-1

To assess the validity of these calculations, we also characterized the minimum energy path between phases using generalized solid-state nudged elastic band(G-SSNEB) [104] which involves both atomic and unit cell degree of freedom. The G-SSNEB approach determines the minimum energy pathway between initial and final states by simultaneously relaxing atomic and cell degrees of freedom. We used four images between our initial (A) and final (M1-DS) states, and the initial path is created based on linear interpolation of cell vectors and atomic coordinates. We used force convergence criterion of 10^{-3} eV/Å to determine minimum energy pathway. Figure A.2 compares the G-SSNEB transformation pathway with one computed on a linear path for A to M1-DS. Given the simplicity of the transformation, these two results are indistinguishable.

Our phase transformation calculations exhibit a range of behaviors, from barrierless transformations observed from the unconstraint relaxations of the austenite cells to a relatively small barrier of 0.8 meV/atom between A and M1-DS. This is consistent with prior work on martensitic materials, for example, Chakraborty et al. [105] observed a barrier of 7 meV/atom for $Ti_Ta_{0.33}$ using G-SSNEB and Kibey et al. [106] observed a barrier of 6.5 meV/atom for NiTi.

3.4 Interfacial strain to stabilize the martensite phase

With the objective of increasing the martensitic transformation temperature, we explore the effect of epitaxial strain on the relative energy between the two phases (section 3.4.1 and section 3.4.2). We chose the martensite variant with lowest energy (variant 1) of SQS-1 for further calculations. The reason for choosing SQS-1 is the lower energy of its austenite and martensite by 1.4 meV/atom and 1.8 meV/atoms, respectively, compared to SQS-2.

3.4.1 Bi-axial strain on closed packed plane

It has been shown that the substrate can play an important role in altering the relative energetics of different phases in a thin film by via interfacial strain [82], [83]. For example, Choi et al. [82] have shown that the $GdScO_3$ and $DyScO_3$ substrates increase the rela-

tive stability of ferroelectric tetragonal phase in $BaTiO_3$ and improves the transformation temperature to 400 ºC and 540 ºC, respectively, compared to 130 ºC in bulk.

In order to effectively mimic the effect of substrate on martensitic stability, we force the lattice parameter on the closest pack $(011)_A$ (xy) plane of both austenite and martensite phases while relaxing the third lattice parameter along $[011]_A$ (z) to a stress below 0.1 GPa. We selected the $(011)_A$ plane for biaxial strain because it is a lowest energy surface in both austenite and martensite (closest pack plane). In-plane lattice parameters range from the martensite to austenite lattice parameters as a function of λ as shown as shown in Eq. 3.6 and Eq. 3.7.

For each set of lattice parameters, starting with both martensite atomic positions and austenite atomic positions, we relaxed the structures with respect to atomic positions. While relaxing the structures, starting with austenite atomic positions, we observed a transformation to the martensite structure for bi-axial strains corresponding to λ of 0.6 or less. In order to prevent this transformation and calculate the energy of the austenite (unstable at 0 K), we performed a constrained relaxation for structures starting with austenite atomic positions. This was accomplished by the following steps: i) cell lattice parameter is relaxed in the z direction while relaxing the ions along x, ii) ions are further relaxed in x and y directions, iii) ions are relaxed in x and z directions, and iv) ions are relaxed in x, y and z directions sequentially. Specific steps for unconstrained relaxation are chosen based on the structural analysis of austenite and martensite structures. We observed that the transformation from A to M1 results in shuffling of atoms along z direction, and minor relaxation is observed along x and y. Similarly, transformation from A to M2 results in shuffling along y and minor relaxation along x and z. Our objective is to calculate the energy of unstable austenite with maximum degrees of freedom relaxed for a fixed in-plane lattice parameter retaining austenite symmetry. In the first step, we relax the out-of-plane lattice parameter while relaxing atoms only along the x direction as we know that the atoms relaxation in x will not break austenite symmetry, however relaxation along y or z will transform the structure to M1 and M2, respectively. As we are straining the system on a linear path from A to M1, relaxation of atoms along z transform the structure in M1 much faster compared to relaxation of atoms along y (transformation to M2). Based on this observation, we first allow atoms to relax

along x and y until the structure starts to transform in M2 in our second step, and then allow them to relax along x and z in third step. Finally, we allow atoms to relax along all x, y and z until it starts to transforms to either M1 or M2.

At each value of λ the most relaxed structure before the transformation starts is taken. Figure 3.7 shows the effect of strain on relative energies of austenite and martensite phases. It can be observed that the applied strain increases the energy of both austenite and martensite phases which is expected.

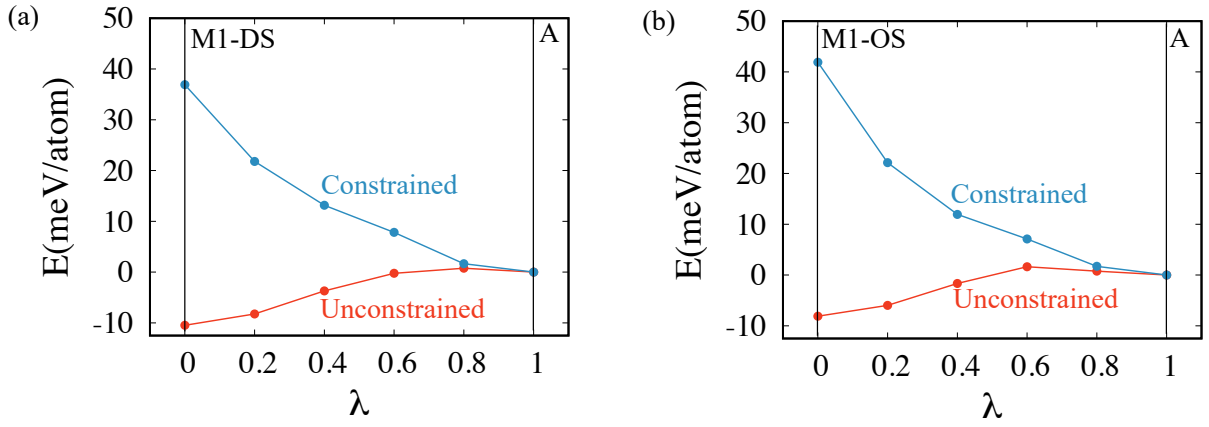

Figure 3.7. Effect of biaxial strain in $(011)_A$ plane on energy of austenite (constrained relaxation) and martensite (unconstrained relaxation) for SQS-1; (a) M1-DS, (b) M1-OS, where strains are applied on linear path between austenite and martensite in-plain lattice parameters. All structures are relaxed in out of plane direction

Figure 3.8 shows the effect of in-plain strain on the relative stability of M1-DS and M1-OS over the austenite phase and the estimated transformation temperatures from Eq. 3.1. We found that the zero-temperature energy differences between A and M2-DS (M2-OS) for 0, 0.2 and 0.4 values of λ are increased to 47.4 (50), 30.1 (28) and 16.9 (13.5) meV/atom, respectively, compared to 10.5 (8.1) meV/atom in bulk. We can estimate the corresponding increase in transformation temperature, as discussed in section 3.2.2, to be 782 K (825 K), 496 K (463 K) and 278 K (223 K), respectively, from 173 K (133 K) in bulk. These results indicate that an appropriate amount of strain ($\lambda \pm 0.4$) can increase the transformation temperature close to room temperature.

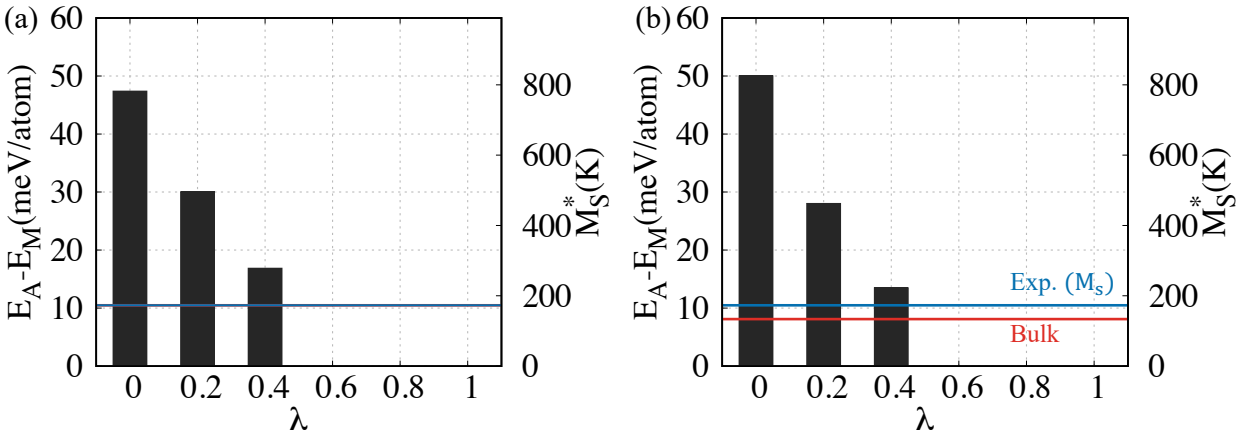

Figure 3.8. Effect of biaxial strain on $(011)_A$ plane on (a) M1-DS, (b) M1-OS stability and estimated transformation temperatures (M_s^*), where strains are applied on linear path between austenite and martensite in-plain lattice parameters. All structures are relaxed in out of plane direction.

We note that the strain required to increase the transformation temperature to near room temperature is quite high. Such strains could be achieved through coherent interfaces with an appropriate substrate or matrix material as long as the dimensions of the MgSc phase remains below the critical length for plastic relaxation. In elastic materials, the critical thickness of thin films can be calculated by comparing elastic energy stored as a result of misfit strain to the energy required to form a dislocation [107] but martensitic materials exhibit much higher coherency limits. For example, Buschbeck et al. [108] have shown coherent martensitic $Fe_{70}Pd_{30}$ films 50 nm in thickness over a family of substrates that span the entire Bain path of the transformation, with strains of over 8%.

3.4.2 Mg-Sc/Mg nanolaminates

Ogawa et al. [109] studied the precipitation kinetics of Mg-rich HCP phase in BCC matrix of Mg-Sc alloy, however, they did not report the effect of precipitation on martensitic transformation. Bulk Mg does not show phase transformation from HCP to BCC while heating due to relatively large zero-temperature energy difference between BCC and HCP phases and low melting temperature. With the purpose of stabilizing the martensite phase by utilizing the high stability of HCP Mg, we created nanolaminates with pure Mg and the Mg-Sc (19.44 at.% Sc) alloy along closest pack plane $(011)_A$, see Figure 3.9. Similar to bi-axial strain, we selected $(011)_A$ plane due to its low surface energy.

We studied the energetics of nanolaminates (also called superlattices) by varying the fraction of pure Mg (2,4 and 6 layers) while Mg-Sc (19.44 at.% Sc) have 6 layers along the $[011]_A$ directions. Similar to bulk Mg-Sc (19.44% Sc) , we obtained the equilibrium structure and energy of austenite by minimizing the energy with respect to atomic positions and cell volume. Cell shape is held fixed in order to retain cubic symmetry. In the case of the martensite structures, full relaxation via energy minimization with respect to atomic positions, cell shape and cell volume is performed. Austenite and martensite energy difference is defined as following:

$$\Delta E = E_A - E_M = \frac{E_{Total,A} - E_{Total,M}}{N_{Total}} \tag{3.9}$$

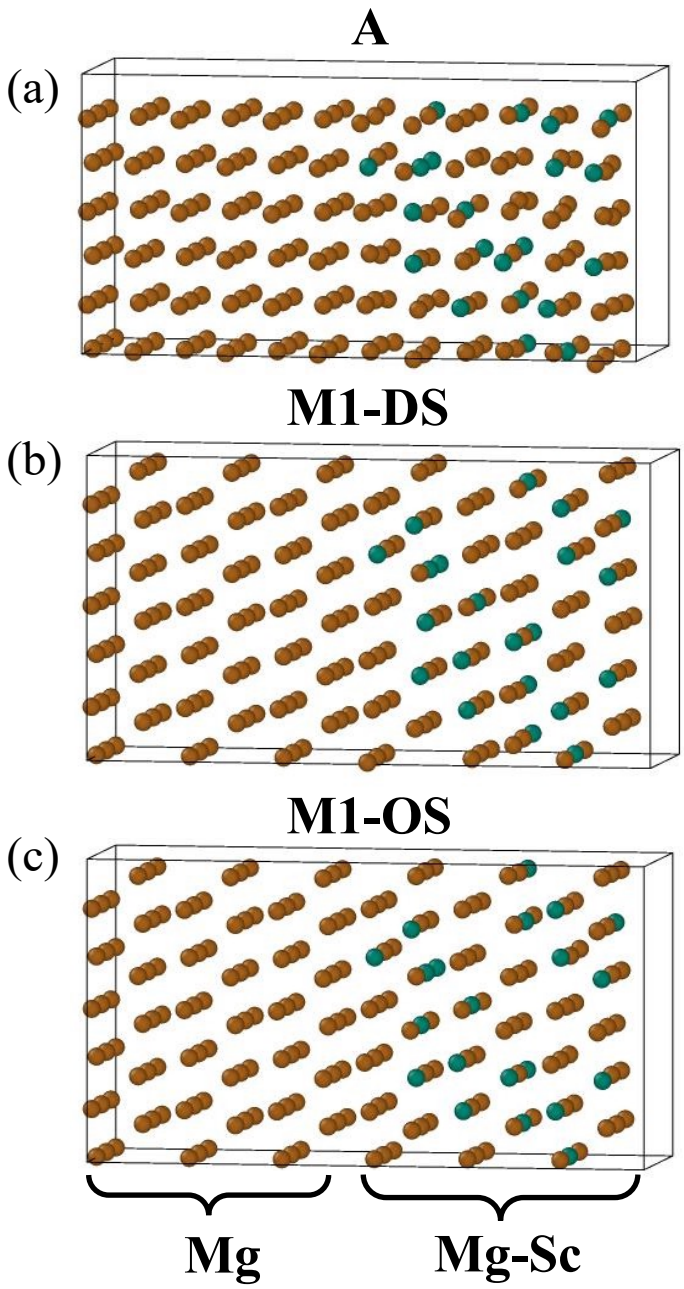

Figure 3.9. Snapshots of relaxed structures of nanolaminates containing 50% pure Mg and 50% of (a) A, (b) M1-DS, (c) M1-OS. Brown and green colors are used for Mg and Sc atoms, respectively.

Figure 3.10 compares the relative stability of M1-DS and M1-OS over A and the predicted transformation temperature for nanolaminates containing pure Mg and Mg-Sc (19.44 at.% Sc) alloy as a function of relative fraction of pure Mg. Transformation temperatures for nanolaminates are predicted using Eq. 3.1 with proportionality constant n=1.422 (described in section 3.2.2). We find that the martensite stability increases with increasing fraction of pure Mg in laminates which is expected. For 2, 4 and 6 layers of pure Mg in Mg-Sc/Mg, zero-temperature energy differences between A and M1-DS (M1-OS) increase to 12.9 (12.1), 16.8 (15.39) and 18.1 (16.9), respectively, and the transformation temperature can be estimated to increase to 212 K (200 K), 277 K (254 K) and 299 K (278 K). We believe that this increase in transformation temperature is not specific to pure Mg, and it can also be obtained by nanolaminates or by precipitates of other martensite stabilizing phases. We believe that the precipitates will affect the martensitic transformation which is also shown earlier both computationally [60] and experimentally [55], [56].

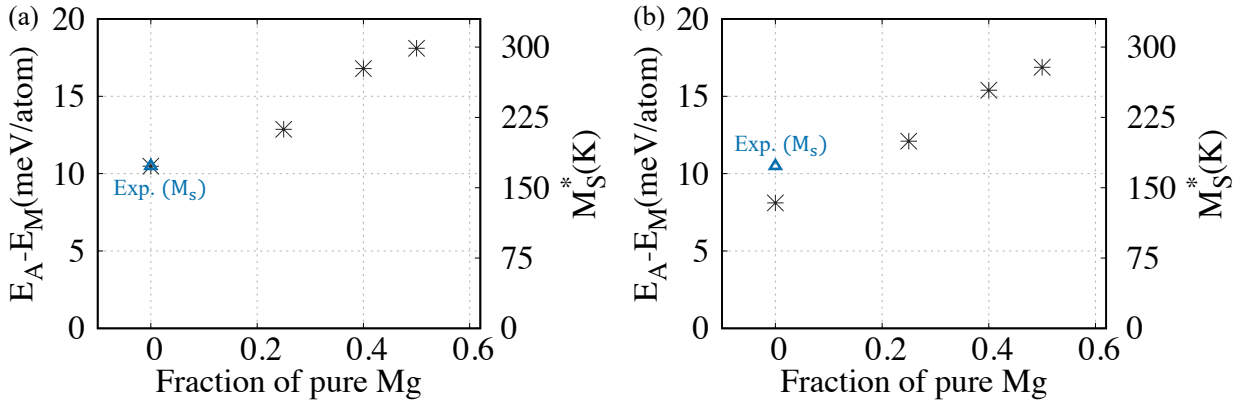

Figure 3.10. Effect of pure Mg fraction in nanolaminates on (a) M1-DS, (b) M1-OS stability and transformation temperatures (M_s^*), where laminates are created normal to $(011)_A$ plane

3.5 Conclusions

We characterized the martensitic transformation between high-temperature BCC austenite and low-temperature orthorhombic martensite using DFT in a Mg-Sc based lightweight

shape memory alloy. Our predicted lattice parameters, x-ray diffraction pattern and zero-temperature energy difference are consistent with experiments.

We studied the effect of bi-axial strain on the energetics and transformation temperature and we found that the zero-temperature energy difference between austenite and martensite can be increased to 16.9 meV/atom by applying 6.8% compressive strain along [100] and 5.8% tensile strain along $[0\bar{1}1]$ which can be expected to result in an increase in transformation temperature to 278 K compared to 173 K in bulk. Simulations of nanolaminates between pure Mg and Mg-Sc binary alloy revealed that the Mg acts as a martensite stabilizer and increases the zero-temperature energy difference to 18.1 meV/atom for 50 at.% Mg. Such an energy difference can be expected to increase the transformation temperature to room temperature. Thus, our simulations showed that epitaxial bi-axial strain which can be obtained using substrates or by a suitable second phase has the potential to increase the operation temperature in lightweight Mg-Sc alloys to room temperature.

4. MARTENSITIC TRANSFORMATION IN SUPERLATTICES OF TWO NON-TRANSFORMING METALS

This chapter was adapted from Shivam Tripathi, Michael S. Titus, and Alejandro Strachan. "Martensitic transformation in superlattices of two non-transforming metals." Journal of Applied Physics 130.16 (2021): 165105. [110].

A number of studies have shown that the coherent integration of a second non-transforming phase in martensitic materials results in unprecedented thermo-mechanical properties. In this chapter, we demonstrate the possibility of martensitic transformation by epitaxially combining two non-transforming materials, Mg (hexagonal closed packed (HCP)) and MgLi (body centered cubic (BCC)). Density functional theory calculations predict that MgLi/Mg superlattices undergo a transformation crystallographically equivalent to MgSc alloys and can be expected to result in finite temperature shape memory behavior. We predict the zero-temperature energy of the martensite phase to be 9.3 meV/atom lower than austenite for a 50-50 at.% MgLi/Mg nanolaminate, which is expected to result in a martensitic transformation temperature of approximately 150 K. This energy difference can be tuned between 4.9 meV/atom and 18.1 meV/atom by varying the fraction of pure Mg phase in the superlattice, potentially enabling the transformation from cryogenic to room and higher temperatures. While Li diffusion might limit the applications of the systems proposed, this work opens the door to a new approach to create martensitic materials.

4.1 Introduction

Mg is among the most attractive elements for various applications in automobile [111], aerospace [112], sport [113], robotic [114], and medicine [115] industries due to its low density (1.74 g/cm3). However, the lack of room temperature ductility due to the HCP structure limits its application. To address this challenge, many efforts have been focused on stabilizing the BCC structure in Mg using alloying elements [18], [46], [116], [117] and epitaxial stresses [118], [119]. The addition of Li as an alloying element changes its crystal structure from HCP to BCC, which results in improved ductility owing to the larger number of slip systems available in BCC structures [117]. Furthermore, Mg-Li alloys also have a lower

density than pure Mg. These interesting characteristics make Mg-Li based alloys promising candidates for next-generation automotive and aerospace components [120]. In addition to alloying, superlattices have been utilized to stabilize the BCC phase in HCP-based materials [118], [119], [121]. For example, the superlattices of 5nm/5nm Mg/Nb [118], [119] and 1.55 nm/1.55 nm Zr/Nb [121] are found to be stable as BCC structures. In this study, we create various superlattices of MgLi/Mg, the ultra-lightweight composites, by varying their relative fractions with the objective of not only stabilizing the BCC phase in Mg but also induce reversible martensitic transformation in these composite systems.

Martensitic transformations are solid to solid, diffusionless transformations from a high-temperature phase called austenite to a martensitic phase. Such transformations can provide strengthening [122] and underlie both pseudo-elasticity and shape memory behavior in SMAs [1]. These unique thermo-mechanical properties make these alloys desirable for a wide range of applications. Only a fraction of the known metallic alloys exhibits martensitic transformations, and a relatively small subset exhibits shape memory. Thus, significant effort has been devoted to optimizing the properties of the few known classes of shape memory materials [1], [2], [40], [41], [123]. One powerful avenue to tune the properties of shape memory materials is the introduction of engineered second phases; these are known to strongly affect the martensitic transformation and, hence, thermo-mechanical properties [55], [56], [59]–[62], [80]. For example, Wang et al. [55] has shown experimentally the tunability of Young's modulus over a wide temperature range in Ti-Nb based shape memory alloys due to elastically confined martensitic transformation as a result of nanoscale concentration modulation. Ultra-low functional fatigue has been observed experimentally in a Ni-Ti-Cu based shape memory alloy due to the presence of coherent Ti2Cu precipitates [56]. In addition to these experimental studies, Guda et al. [59] and Reeve et al.[60] have shown the tunability of hysteresis and transformation temperature as a result of a coherent second phase in nanolaminates and other nanostructure configurations, respectively, using molecular dynamics simulations. Ultra-low stiffness (2 GPa) has also been computationally demonstrated in a composite system of $Ni_{50}Al_{50}$ and $Ni_{63}Al_{37}$ [62]. Moreover, Desai et al. [61] has mapped the effect of the lattice mismatch and the stiffness of the second phase on the hysteresis and transformation temperatures using molecular dynamic simulations. This

body of work shows how the coherent second phases change the double-well free energy landscape underlying martensitic transformation. In this chapter, we extend this concept and demonstrate that martensitic transformations can be induced via the coherent integration of two non-transforming materials.

Mg-Sc alloys are an important class of lightweight SMAs, unfortunately, their low transformation temperature, 173 K, limits their applicability. As discussed in chapter 3, we used electronic structure calculation to study the possibility of using a second phase (pure Mg) to tune the transformation temperature to room temperature [80]. Motivated by the fact that the addition of Mg increases the transformation temperature in MgSc, this paper explores the novel approach of inducing a martensitic transformation in disordered BCC MgLi, a non-martensitic alloy, via the addition of HCP Mg. In addition, Sc is relatively scarce and very costly, this makes Mg/MgLi attractive over MgSc alloys. Our theoretical calculations show that MgLi/Mg superlattices exhibit a martensitic transformation between BCC austenite to orthorhombic martensite. This is crystallographically similar to the transformation observed in Mg-Sc alloys that results in finite temperature shape memory behavior. We note that the MgLi/Mg superlattices studied here might be unstable at room and higher temperatures due to the mass interdiffusion of Li atoms. However, the stability of Mg/Nb superlattices [119] provides hope, and we believe that further experimental investigation of diffusion in MgLi/Mg superlattices is required to make a definite claim about their stability. Nonetheless, we believe that the first demonstration of martensitic transformation by combining two non-transforming phases will open a wide material space for the discovery and design of next-generation SMAs.

4.2 Simulation and analysis details

4.2.1 Atomistic models

To build coherent MgLi/Mg nanolaminates, we start with relaxed structures of MgLi, and Mg oriented so that the interface is between the (011)MgLi and (0001)Mg surfaces. MgLi is a chemically disordered BCC alloy where each atomic site is equivalent and randomly occupied by either Mg or Li. The models for stoichiometric MgLi are based on a tetragonal

supercell of BCC structure with cell vectors oriented as: a=[100] (x), b=[011] (y), and c=[0$\bar{1}$1] (z) and the simulation cell is generated by replicating the unit cell three times along each direction. To obtain a chemically disordered structure for the binary stoichiometric MgLi, we assign atoms using SQS [90]–[92] based on an algorithm developed by van de Walle et al. [91], implemented in ATAT [92] package. The SQS approach matches the pair, triplet, and quadruplet correlation functions with those of the true random structure. Pure Mg is based on orthorhombic supercell of the HCP structure with cell vectors oriented along a=[1$\bar{2}$10] (x), b=[0001] (y), and c=[10$\bar{1}$0] (z). The simulation cell for pure Mg is replicated three times in x and z directions, and we generated various supercells by varying replication along y from 2 times (4 layers along y) to 9 times (18 layers along y). The structures of stoichiometric MgLi and pure Mg phases are shown in Figure A.3. The MgLi structure is relaxed with respect to atomic positions and cell volume; the cell shape (ratio between lattice parameters and angles) was held fixed to retain the symmetry. This is justified since the atomic disorder in the relatively small cell used breaks the cubic symmetry. Mg structures are fully relaxed via energy minimization with respect to atomic positions, cell shape, and cell volume.

We created superlattices (coherent nanolaminates) with the stoichiometric MgLi and pure Mg phases along closest pack planes $(011)_{MgLi}$ and $(0001)_{Mg}$, see Figure 4.1. We selected $(011)_{MgLi}$ plane in the MgLi phase and $(0001)_{Mg}$ plane in pure Mg, similar to MgSc/Mg system [80] due to their low surface energy and low epitaxial strains. We studied the energetics of the superlattices by varying the mole fraction of pure Mg (4, 6, 8, 10, 12, 14, and 18 layers) while maintaining 6 layers along the $[011]_A$ direction of the stoichiometric MgLi. To obtain the austenite structure in MgLi/Mg superlattices, we started with the relaxed cubic lattice parameters of MgLi in our initial structure and first performed a relaxation with respect to atomic positions and cell volume; the cell shape (ratio between lattice parameters and angles) was held fixed to retain the symmetry. We also performed a full relaxation on these austenite structures via energy minimization with respect to atomic positions, cell shape, and cell volume. We found austenite structure to be stable with respect to relaxation in cell shape only for 60-40 Mg-Li/Mg and transformation to one of the variants of martensite is observed for other structures. Martensite structures in these superlattices are obtained by

starting with initial lattice parameters of pure Mg and perform full relaxation via energy minimization with respect to atomic positions, cell shape, and cell volume. Importantly, the angles in relaxed structures of our martensite remain very close to 90° (less than 0.2° deviation), which is an artifact of chemical disorder in a relatively small supercell. We also calculated the energetics of another variant of martensite associated with our tetragonal cell by interchanging the lattice parameters along $[011]_A$ and $[0\bar{1}1]_A$ in the description above and followed by full relaxation of structures. Figure 4.1 shows the relaxed structures of austenite and two variants of martensite in 60-40 MgLi/Mg nanolaminates.

We also studied the transformation pathway from austenite to martensite to further confirm the transformation behavior corresponding to shape memory alloys. To do so, we linearly interpolated the lattice parameter between the phases followed by structure relaxation with respect to atomic coordinates. The order parameter λ describes the degree of transformation, and the lattice parameters are determined as follows:

$$a_\lambda = (1-\lambda)a_A + \lambda a_{M1,M2} \tag{4.1}$$

$$b_\lambda = (1-\lambda)b_A + \lambda b_{M1,M2} \tag{4.2}$$

$$c_\lambda = (1-\lambda)c_A + \lambda c_{M1,M2} \tag{4.3}$$

Generalized solid-state nudged elastic band (G-SSNEB) [104] calculations are also performed to determine the minimum energy pathway between the phases. The G-SSNEB approach does so by simultaneously relaxing atomic and cell degrees of freedom. We created the initial path by linearly interpolating the cell vectors and atomic coordinates. We used four images between our initial and final states.

4.2.2 DFT simulation details

We used the VASP [84]–[87] to perform the DFT calculations within the generalized gradient approximation of PBE [75]. PAW pseudopotentials [88], [89] parameterized for PBE

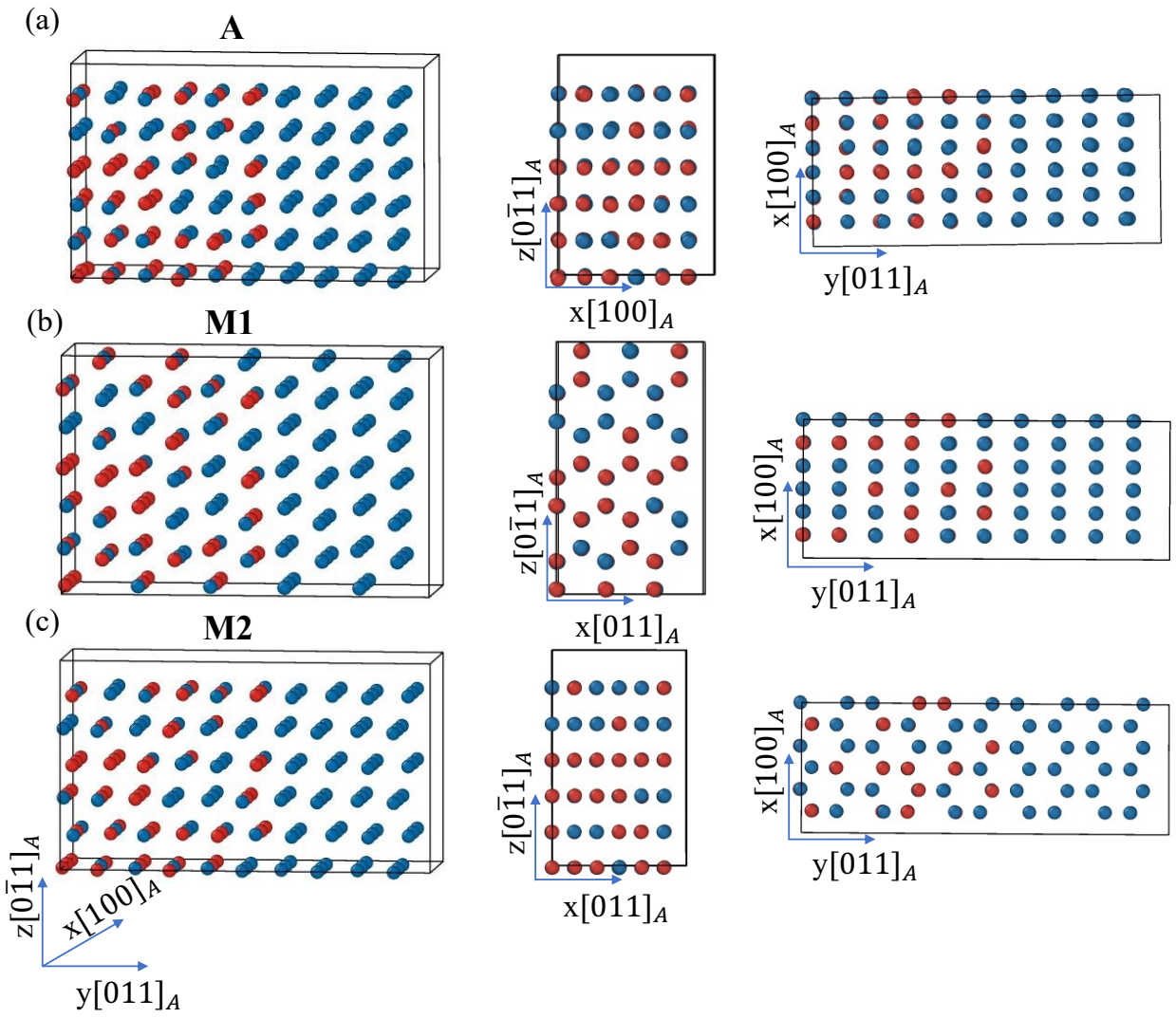

Figure 4.1. Snapshots of the relaxed structure of (a) A, (b) M1, and (c) M2 for nanolaminate containing 60% stoichiometric MgLi phase and 40% pure Mg phase. Red and blue colors are used for Li and Mg atoms, respectively.

with one valence electron for Li and two valence electrons for Mg were used. We used a 450 eV energy cut-off and Gaussian smearing for integrals in the first Brillouin zone with a smearing of σ=0.05 eV. We used gamma-centered 7x5x5 k-mesh for sampling the reciprocal space for stoichiometric BCC MgLi and HCP Mg Phase. Gamma-centered 7x3x5 and 7x1x5 k-mesh were used for 6MgLi/4-12Mg and 6MgLi/14-18Mg superlattices, respectively. We used 10^{-4} eV energy difference as the convergence criterion for electronic relaxation. Atomic positions were relaxed until the force on every atom was less than 0.01 eV/Å. All our calculations were non spin-polarized.

4.2.3 Estimating transformation temperature

The martensitic transformation temperature can be calculated by computing the free energy of the austenite and the martensite phases via first principles simulations. However, our goal is to demonstrate a martensitic transformation in a superlattice of two non-transforming materials, and the simple estimate of the transformation temperature will suffice. Thus, to estimate the martensitic transformation temperature from the calculated zero temperature energy difference between the phases, we use the empirical relation proposed and discussed in Refs. [95]–[97], [124], [125]:

$$M_S^* = n\frac{E_A - E_M}{k_B} \tag{4.4}$$

The details of the applicability and the range of proportionality constant for various systems are discussed in Ref. [80]. As will be described below, the crystallographic characteristics of the martensitic transformation in Mg/Mg-Li superlattices are identical to the Mg-Sc system. This indicates that a value n=1.42 found in Ref. [80] would be appropriate. To estimate uncertainties in our estimates, we note that the bulk modulus (BM) of 60/40 MgLi/Mg (29 GPa) is lower than the BM of Mg-Sc (44 GPa) in the martensitic phase and Ref. [80] documented a dependence of n on stiffness in metals undergoing BCC to HCP transformations. Assuming a similar dependence, n could be as large as 1.65 for Mg/MgLi. We will use these two values to estimate a range of transformation temperatures for the superlattices studied. We note that Zarkevich et al. [124] suggest a value n=1 to be widely

applicable for various first-order transformations. However, the current authors found a significant deviation in n from unity for BCC to HCP transformation in Zr, Mg, and MgSc in Ref. [80].

4.3 Transformation between austenite and martensite phase

4.3.1 Structure and energetics of austenite and martensite phases

The relaxation of the stoichiometric MgLi structure with respect to atomic positions and cell volume, maintaining cell shape fixed as discussed in section 4.2.1, results in the BCC phase to be stable with the relaxed parameter of 3.467 Å. We also performed unconstrained relaxation of these structures, which results in angles deviating slightly from 90° (less than 0.4°), which is an artifact of the chemical disorder in the relatively small supercell. We used the relaxed cubic and orthorhombic supercells of MgLi and Mg to generate MgLi/Mg superlattices, see section 4.2.1. Superlattices with 40 at.% of pure Mg phase results in relatively minor changes in lattice parameters as the Mg phase deforms and adopts the BCC structure. Quite interestingly, as we had hypothesized, for a fraction of the pure Mg phase of 50% and over, unconstrained relaxation starting in the austenite phase results in a martensitic transformation. We found the martensite phase in the MgLi/Mg superlattices to be orthorhombic (similar to Mg-Sc alloys) with the following lattice correspondence between austenite and martensite:

$$[100]_A \rightarrow [100]_M, [0\bar{1}1]_A \rightarrow [010]_M, [011]_A \rightarrow [001]_M \tag{4.5}$$

During transformation, austenite undergoes 9.8% compression along $[100]_A$ and 2.2% and 9.9% tension along $[011]_A$ and $[01\bar{1}]_A$, respectively, for 60-40 MgLi/Mg. In addition to the change in shape, atomic shuffling on closed-packed 110_A planes completes the transformation. Thus, six different variants of martensite are possible for each austenite owing to six $(110)_A$ planes in cubic structures. In a bulk disordered structure, these variants should have identical energies and lattice parameters. However, SQS cannot generate true random structures in relatively small supercells, which leads to different formation energy and lattice parameters for these different variants. To obtain the most stable martensite variant

in our calculations, we calculated the energetics of two variants of martensite associated with our tetragonal cell by interchanging the lattice parameters along $[011]_A$ and $[0\bar{1}1]_A$ in the description above, and followed by full relaxation as discussed in section 4.2.1. The relaxed lattice parameters and the energetics of various phases in these superlattices are reported in Table 4.1. Figure 4.2 compares the relative stability of both martensites (M1 and M2) over austenite for the composition range where our calculations predict a solid-to-solid transformation to exist. To calculate the energy of the austenite, we performed a constrained relaxation (as described in section 4.2.1). Figure 4.2 also shows the estimated transformation temperature for various superlattices, obtained from Eq. 4.4, see section 4.2.3. The energy difference between austenite and martensite ranges from 4.9 meV/atom to 18.1 meV/atom, and the estimated transformation temperature ranges from 94 K (81 K) to 347 K (299 K) corresponding to n=1.65 (1.42) for a fraction of the pure Mg phase between 40% to 75%. We note that for MgSc alloys with a Ms temperature of 173 K the energy difference is 10.5 meV/atom (horizontal line in Fig. 4.2).

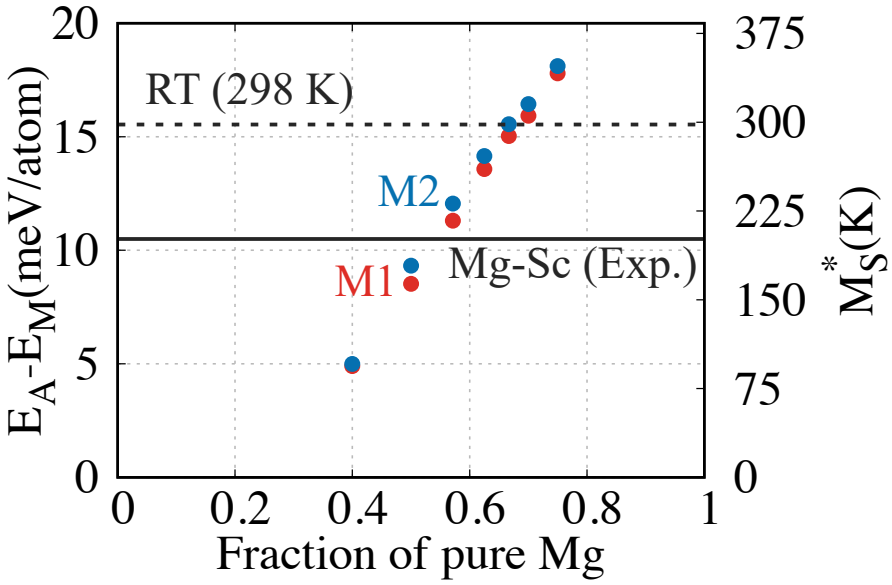

Figure 4.2. Effect of pure Mg phase fraction in Mg/MgLi nanolaminates on martensite stability and estimated transformation temperature (M_s^*) with n=1.65. The solid and the dashed horizontal lines represent M_S for Mg-Sc and room temperature (RT), respectively.

Table 4.1. Lattice parameters (Å) of all phases (Austenite (A), Martensite1 (M1), Martensite2 (M2)) and relative energy differences (meV/atom) of all martensite phases with respect to corresponding austenite for various MgLi/Mg superlattices

Mg fraction in MgLi/Mg		**a(Å)**	**b(Å)**	**c(Å)**	$\mathbf{E_A - E_M}$ **(meV/atom)**
0.4	A	3.512	4.967	4.967	_
	M1	3.167	5.076	5.460	4.90
	M2	3.167	5.423	5.103	4.99
0.5	A	3.524	4.983	4.983	_
	M1	3.171	5.101	5.467	8.52
	M2	3.168	5.443	5.120	9.33
0.571	A	3.524	4.983	4.983	_
	M1	3.175	5.117	5.473	11.30
	M2	3.177	5.445	5.130	12.06
0.625	A	3.538	5.003	5.003	_
	M1	3.179	5.123	5.479	13.58
	M2	3.193	5.439	5.132	14.15
0.667	A	3.542	5.009	5.009	_
	M1	3.181	5.125	5.490	15.03
	M2	3.190	5.451	5.139	15.56
0.7	A	3.546	5.015	5.015	_
	M1	3.184	5.125	5.497	15.93
	M2	3.191	5.459	5.143	16.44
0.75	A	3.550	5.021	5.021	_
	M1	3.186	5.136	5.499	17.79
	M2	3.190	5.479	5.149	18.11

To further confirm that the martensitic transformation in Mg/MgLi is crystallographically similar to MgSc alloys, Figure 4.3 compares the simulated XRD pattern of 60-40 MgLi/Mg with the experimental XRD pattern reported by Ogawa et al. [18] for the Mg-Sc system. We combined the XRD pattern of the austenite and the martensite phases of 60-40 MgLi/Mg superlattice with equal weights since both phases coexist in the experimental system. Our XRD pattern is consistent with the martensitic transformation observed in Mg-Sc from BCC austenite to orthorhombic martensite resulting in finite temperature shape memory behavior. Our predicted structures result in all the peaks associated with the austenite and martensite phases reported in experiments for Mg-Sc [18]. As expected, the peak positions are shifted compared to Mg-Sc due to the difference in lattice parameters. We calculated the interplanar distance and corresponding 2θ angles for all the peaks based on our DFT lattice parameters of M1 and M2 of 60-40 MgLi/Mg and the experimentally obtained lattice parameters (martensite orientation corresponds to our M2) for Mg-Sc [18] to quantify the shift in the peak positions, see Table 4.2. The difference in the lattice parameters explains the shift in the peak positions.

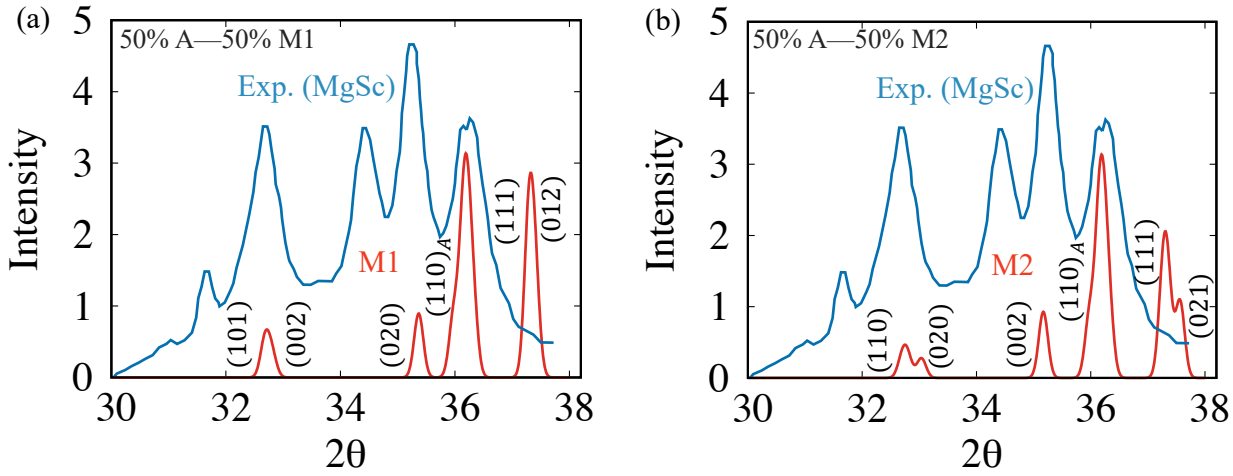

Figure 4.3. XRD pattern for system with 50-50 austenite (A) and (a) martensite variant 1 (M1) phases; and (b) martensite variant 2 (M2) phases for nanolaminate containing 60% stoichiometric MgLi phase and 40% pure Mg, where Gaussian distribution with a standard deviation of 0.08 is used for peak broadening. The blue curve shows the XRD pattern of Mg-Sc from experiments [18] at -190 °C, where martensite and austenite coexist.

Table 4.2. Calculated interplanar spacing and 2θ based on experimental (Mg-Sc) and DFT (60/40 MgLi/Mg) lattice parameters

	$\mathbf{d_{hkl,exp.}(\text{Å})}$	$\mathbf{d_{hkl,M1}(\text{Å})}$	$\mathbf{d_{hkl,M2}(\text{Å})}$	$\mathbf{2\theta_{hkl,exp.}}$	$\mathbf{2\theta_{hkl,M1}}$	$\mathbf{2\theta_{hkl,M2}}$
$(101)_{M1}, (110)_{M2,exp.}$	2.826	2.740	2.735	31.7°	32.7°	32.7°
$(002)_{M1}, (020)_{M2,exp.}$	2.772	2.730	2.711	32.3°	32.8°	33.0°
$(020)_{M1}, (002)_{M2,exp.}$	2.612	2.538	2.552	34.3°	35.4°	35.2°
$(111)_{M1}, (111)_{M2,exp.}$	2.486	2.411	2.410	36.1°	37.3°	37.3°
$(012)_{M1}, (121)_{M2,exp.}$	2.449	2.404	2.394	36.7°	37.4°	37.6°
$(110)_{A,exp.}$	2.547	2.483	2.483	35.2°	36.2°	36.2°

4.3.2 Austenite-martensitic transformation Path

While the energetics of the phases at zero-temperature provide information about thermodynamic stability, the calculation of energy barriers is required in order to get a complete understanding of the phase transformation. To study the austenite-martensite transformation pathway, we linearly interpolated the lattice parameters between the austenite and martensite phases, see Eqs. 4.1-4.3, and relaxed the structures with respect to atomic coordinates. To assess the validity of these calculations, we also characterized the minimum energy path between phases using G-SSNEB, which involves both atomic and unit cell degrees of freedom as described in section 4.2.1. We created the initial path by linearly interpolating the cell vectors and atomic coordinates. We used four images between our initial (A) and final states (M1 & M2). Force convergence criterion of 10^{-3} eV/Å is used during G-SSNEB calculation. Transformation pathways between A and M1 obtained via linear interpolation and G-SSNEB are close, which was also observed in our previous work on the MgSc system [80]. However, maximum force on atoms during G-SSNEB calculation between A and M2 does not converge to the convergence criterion of 10^{-3} eV/Å even for more than 1000 ionic steps. Figure A.4 shows the transformation pathway between A and M2 for the convergence criterion of $5X10^{-3}$ eV/Å. One possible explanation for not reaching the convergence criterion might be the presence of a wavy interface between MgLi/Mg for M2 structures, unlike flat interface with closed packed planes in M1, see Figure 4.1. Here, we will use the transformation pathway obtained by linear interpolation between A and M2 for a comparative study. Figure 4.4 shows the transformation pathway from A to M1 (Linear & G-SSNEB) and A to M2 (Linear) for 60-40 MgLi/Mg nanolaminate. We found no barrier for transformation between A and M1 and a small barrier between A and M2 (0.6 meV/atom) for 60-40 MgLi/Mg nanolaminate. M2 is thermodynamically more stable by 0.09 meV/atom compared to M1, see Table 4.1, however, the transformation to M1 is expected to be kinetically preferred over M2 due to no energy barrier between the phases. The observation of no barrier for M1 and a small barrier for M2 is consistent with our prior study on Mg-Sc [80] and other shape memory alloys in the literature [105], [106], [126]. For example, Salloom et al. [127] found no transformation barrier for TiNb12.5, TiNb16.6, and TiNb25 using G-SSNEB; Chakraborty

et al. [105] observed a barrier of 7 meV/atom for TiTa0.33 using G-SSNEB and Kibey et al. [106] observed a barrier of 6.5 meV/atom for NiTi using linear interpolation.

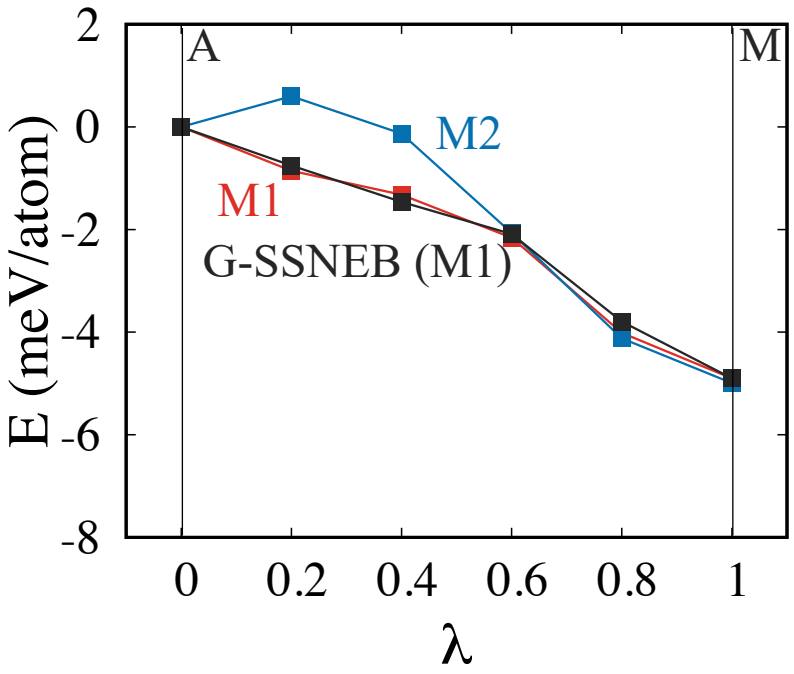

Figure 4.4. Transformation pathway from A to M1 (Linear & G-SSNEB) and A to M2 (Linear) for nanolaminate containing 60% stoichiometric MgLi phase and 40% pure Mg phase.

4.4 Discussion and conclusion

We demonstrate the possibility of martensitic transformations in superlattices between two non-transforming materials, pure Mg and stoichiometric MgLi. The predicted transformation for the superlattices is crystallographically equivalent to that observed in MgSc alloys which are known to exhibit finite temperature shape memory behavior. Our DFT simulations predict the martensite phase to be 9.3 meV/atom lower in energy than austenite for a 50-50 at.% MgLi/Mg nanolaminate. This energy difference can be tuned from 4.9 meV/atom to 18.1 meV/atom by varying the fraction of pure Mg between 40% and 75%. These results represent a novel and rather general avenue to create and engineer martensitic transformations starting from materials that do not exhibit it.

We now discuss the possibility of the experimental realization of the coherent superlattices proposed here. Hou et al. [126] have shown the stabilization of BCC phase in Ta/Ti superlattices up to a critical individual layer thickness (h) of 7.5 nm. As expected for thickness above the critical value, for h > 7.5 nm the BCC structure destabilizes and the superlattice is composed of BCC Ta/BCC Ti/HCP Ti/BCC Ti/BCC Ta. A similar observation is also made for Nb/Mg superlattices for a critical thickness of 5 nm [118]. The critical thickness h for a particular system depends on the misfit strain and mechanical properties of the two phases. The lower misfit strain is expected to result in higher critical thickness. The misfit strain at the HCP/BCC nanolaminates is defined as:

$$\epsilon_{misfit} = \sqrt{(\frac{(a_{[1\bar{2}10],HCP} - a_{[100],BCC})}{0.5 * (a_{[1\bar{2}10],HCP} + a_{[100],BCC})})^2 + (\frac{(a_{[10\bar{1}0],HCP} - a_{[0\bar{1}0],BCC})}{0.5 * (a_{[10\bar{1}0],HCP} + a_{[0\bar{1}0],BCC})})^2} \tag{4.6}$$

The misfit strain of our MgLi/Mg laminates is 0.146, which is 0.2% and 13.9% lower than Ta/Ti and Nb/Mg, respectively. Therefore, the critical h of an individual layer before the coherency loss is expected to be at least 5 nm for MgLi/Mg nanolaminates. In this study, our largest nanolaminate is 1.5nm/4.7nm MgLi/Mg, hence, it is expected to be well within the coherency limit. To confirm this, we created a BCC MgLi (6 layers)/BCC Mg (4 layers)/HCP Mg (6 layers)/BCC Mg (4 layers) nanolaminate, see Figure A.5, and the initial lattice parameters are calculated by the weighted sum of the lattice parameters of BCC 60-40 MgLi/Mg and HCP pure Mg. We fully relaxed the structure via energy minimization with respect to atomic positions, cell shape, and cell volume. The relaxed structure is single phase martensite. We also performed the relaxation with respect to atomic positions after enforcing the cubic symmetry at the interfacial plane (xz) in the initial structure, and the relaxation resulted in the single-phase BCC nanolaminate. In conclusion, we do not observe the stabilization of the BCC MgLi/BCC Mg/HCP Mg/BCC Mg/BCC MgLi type structures for the small superlattice periods studied.

We note that the specific superlattices studied here, while attractive from a light-weighting perspective, are not without limitations. Li diffusivity in Mg is relatively high, and the superlattices will likely be unstable with respect to interdiffusion at room and higher

temperatures. Shi et al. [128] have found the diffusion coefficient of Li to be between $2.46x10^{-8}$ cm^2/s to $9.89x10^{-8}$ cm^2/s for BCC Mg-Li alloys with Li composition varying from 60% to 90%. Based on the value for Mg-60Li (at.%), we calculate a time ($t = \lambda^2/D$) of 0.004 s for an interdiffusion distance of 100 nm. This is a worst-case scenario as the Li diffusion in HCP Mg would be significantly lower. We expect that the proposed superlattices to be stable at low temperatures. Other metal combinations result in stable superlattices, e.g. Mg/Nb [119], and we believe our approach can be applied to stable structures.

We note that our general observations are not limited to the MgLi/Mg system and the exploration of additional materials combinations that could result in martensitic transformations should be pursued further, both theoretically and experimentally. The fundamental idea is to coherently integrate a BCC and an HCP material with lattice misfit such that the nanolaminate results in a double-well free energy landscape. The BCC material breaks the 6-fold HCP symmetry which enables shape memory effect. BCC/HCP superlattices would likely involve interfaces at $(011)_{BCC}$ $(0001)_{HCP}$ planes with directions $[100]_{BCC}$ $[1\bar{2}10]_{HCP}$ and $[0\bar{1}1]_{BCC}$ $[10\bar{1}0]_{HCP}$ at the interface. To favor the transformation, the BCC material should cause tension in the HCP material along $[1\bar{2}10]$ and compress along $[10\bar{1}0]$. This restricts the lattice parameter difference between possible materials. Table 4.3 shows possible BCC/HCP materials pairs that could result in martensitic transformation.

Table 4.3. Misfit strains along $[100]_{BCC}\|[1\bar{2}10]_{HCP}$ and $[0\bar{1}1]_{BCC}\|[10\bar{1}0]_{HCP}$ directions at $(011)_{BCC}\|(0001)_{HCP}$ interface for various pairs of BCC/HCP materials

	$\epsilon_{misfit,[100]_{BCC}\|[1\bar{2}10]_{HCP}}(\%)$	$\epsilon_{misfit,[0\bar{1}1]_{BCC}\|[10\bar{1}0]_{HCP}}(\%)$
MgSc/Mg	11.3	-9.0
MgLi/Mg	7.9	-12.3
Nb/Mg	3.6	-16.6
Ta/Mg	3.7	-16.6
MgSc/Zr	10.2	-10.1
MgLi/Zr	6.8	-13.5
Nb/Zr	2.5	-17.7
Ta/Zr	2.5	-17.7
MgSc/Ti	20.0	-0.2
MgLi/Ti	16.7	-3.6
Nb/Ti	12.4	-7.9
Ta/Ti	12.4	-7.8
Mo/Ti	7.7	-12.6
V/Ti	2.0	-18.2
Cr/Co	13.9	-6.4
V/Co	17.9	-2.3

5. UNCOVERING THE ROLE OF NANOSCALE PRECIPITATES ON MARTENSITIC TRANSFORMATION AND SUPERELASTICITY

This chapter was adapted from Shivam Tripathi, Karthik Guda Vishnu, Michael S. Titus and A. Strachan, "Uncovering the role of nanoscale precipitates on martensitic transformation and superelasticity" Acta Materialia (under review). [129].

We characterize the role of coherent nanoscale B2 $Ni_{50}Al_{50}$ precipitates on the temperature and stress induced martensitic phase transformation in nanocrystalline $Ni_{63}Al_{37}$ shape memory alloys using multi-million-atoms MD simulations. We studied two types of precipitates: one with single crystal precipitates (SXP) and a second where grain boundaries cut through precipitates (PXP). Simulations reveal that the presence of B2 precipitates stabilizes the cyclic flag-shaped stress-strain response, characteristic of superelasticity, and reduces remnant strain. In contrast, single-phase nanocrystalline $Ni_{63}Al_{37}$ exhibits degradation of the reverse transformation during cyclic loading and, eventually, incomplete reversible transformation within a few cycles. This is consistent with previous experimental findings of ultra-low fatigue in Ni-Ti-Cu alloys with Ti_2Cu precipitates. The simulations reveal that the presence of precipitates significantly improves the reversibility of the transformation by acting as elastic zones that partially shield the martensitic transformation and drive the reverse transformation. A detailed analysis of the MD trajectories reveals that the martensitic transformation of the matrix induces ultra-large elastic deformation in some of the B2 precipitates (approximately 12%) to the point of resulting in a martensite-like atomic structure.

5.1 Introduction

SMAs owe their ability to recover their original shape after large deformations upon heating and superelastic behavior to an underlying solid-state, diffusion-less phase transformation from austenite to martensite and back [1]. These martensitic transformations enable solid-state actuation [15], mechanical damping [130], and, recently, emerging solid-state refrigeration technologies [131], making SMAs attractive for aerospace [132], medical

[4], automobile [111], construction [5], and micro-electro-mechanical systems (MEMS) [7] applications. Tuning of the underlying martensitic transformation undergirds the design of next-generation SMAs for specific applications. While the search for new shape memory alloy compositions remains important [40], [41], [133], two-phase shape memory alloys incorporating a non-transforming coherent second phase have shown great promise.

The incorporation of coherent second phases has been shown both experimentally [55], [56], [58] and computationally [59]–[62], [80] to significantly alter the characteristics of martensitic transformations and therefore, the thermo-mechanical response of these composite systems. For example, Ni-Ti-Cu- based SMAs have been experimentally shown to exhibit ultra-low fatigue up to millions of cycles in the presence of coherent Ti_2Cu precipitates [56]. Tunable Young's modulus has been experimentally observed over a wide temperature range in Ti-Nb-based gum metals resulting from elastically confined martensitic transformation due to nanoscale concentration modulation [55]. Strength and functional fatigue are shown to improve significantly in the crystalline-amorphous nanocomposites of nano-crystalline NiTi due to suppression of transformation-induced dislocations in the crystalline region and shear bands in the amorphous region via mutual strengthening of the two phases in nanolaminates [58]. Molecular dynamics studies by Guda Vishnu et al. [59] and Desai et al. [61] have shown that the transformation temperatures and hysteresis can be tuned significantly by the presence of coherent second phases in nanolaminates. Moreover, an ultra-low modulus (as low as 2GPa) was observed in the composite system of $Ni_{63}Al_{37}$ and $Ni_{50}Al_{50}$ [62].

While most of the experimental studies have focused on polycrystalline samples, atomistic studies have, to date, only characterized the role of the average grain size in polycrystalline materials [134], [135]. An atomic-level understanding of the role of precipitates and how their interaction with grain boundaries influences the characteristics of martensitic transformation is still lacking. For example, ultra-low functional fatigue has been observed in Ni-Ti-Cu-based SMAs due to the presence of coherent Ti_2Cu precipitates [56], however, the underlying atomistic mechanisms governing the transformation characteristics remain unknown. Several open science questions persist, which include: do precipitates undergo any structural transition driven by the matrix? what atomic-level processes are responsi-

ble for remnant strain? and how does the presence of precipitates influence the martensite growth and reverse transformation? To address these questions is the purpose of this study.

Large-scale MD simulations of stress- and temperature-induced martensitic transformation in nanocrystalline $Ni_{63}Al_{37}$ SMAs with nanoscale $Ni_{50}Al_{50}$ provide a picture of these processes with atomic resolution. The simulations show that the ultra-fine grain single-phase $Ni_{63}Al_{37}$ alloy exhibits a significant degradation of the reverse transformation during cyclic loading and, eventually, incomplete reversible transformation within a few cycles. The incorporation of coherent B2 precipitates stabilizes the stress-strain response and can be utilized to design fatigue-resistant ultra-fine grain shape memory alloys for next-generation applications.

5.2 Simulation details

5.2.1 Interatomic potential model

We used an EAM interatomic potential developed by Farkas et al. [136] to describe atomic interactions in Ni-Al alloys. The potential was parametrized for the B2 phase of NiAl and Ni_5Al_3. Material properties like elastic constants were matched with more than 90% accuracy, and lattice parameters and cohesive energies were matched with 99% accuracy for the B2 phase. This potential captures the martensitic transformation from B2 austenite to monoclinic martensite for compositions between 61-66 at.% Ni, and it has been used in prior studies to investigate the martensitic transformation in NiAl based shape memory alloys [59], [60], [62], [134], [137]. However, the martensite structure predicted by this potential differs from the experimentally observed M14 structure, see Ref. [137] for detailed comparisons between structures. Thus, our simulations should be taken to correspond to model shape memory alloy only approximately equivalent to NiAl. All molecular dynamics simulations were performed using large-scale atomic/molecular massively parallel simulator (LAMMPS) [138] in this study.

5.2.2 Nanocrystalline samples with precipitates

We started by creating a polycrystal of stoichiometric NiAl with random grain orientations and 30 nm average grain size using the Atomsk package [139]. Atomsk package uses Voronoi tessellation [140] to construct a polycrystal that divides the space into n cells for user-specified n points (seeds) with the property that any point in a particular cell is closest to its corresponding seed among all seeds. Simulation cell size and the total number of grains were input parameters to the code, which then generated random seeds to create a polycrystal with random grain orientations. Input parameters were chosen such that the average grain size is around 30 nm. Our simulation cell has 54 million atoms and 34 grains. Grain orientations and sizes of all grains are reported in Table A.1.

Both the single- and multi-phase samples were first constructed with a uniform $Ni_{63}Al_{37}$ composition by replacing 26% of Al atoms, chosen randomly, to Ni in stoichiometric NiAl. We decided to study spherical precipitates, 8 nm diameter, and with a volume fraction of 0.12, similar to the experiments on Ni-Ti-Cu systems [56], showing ultra-low functional fatigue. The PXP was generated by randomly selecting random places, non-overlapping spherical regions of 8 nm diameter in a 800 K-relaxed $Ni_{63}Al_{37}$ structure and switching the Ni atoms in the Al sub-lattice back to Al, turning the $Ni_{63}Al_{37}$ alloy back to stoichiometric NiAl. SXP was generated starting from the PXP sample via the following steps: i) each precipitate that cut through one or more grain boundaries is removed; ii) in its place, single crystal configuration from within the grain containing the most atoms in the removed precipitate is placed followed by excess Ni atoms replaced by Al as in the PXP case. We note the possibility of point defects and anti-phase boundaries (APB) at the interfaces of these replaced single crystal precipitates and the matrix.

All nanocrystalline structures were relaxed using Nosé-Hoover isothermal, isobaric (NPT) ensemble at 800 K temperature and 1 atm pressure until the change in average energy is less than 0.002 meV/atom-ps. Structures at 600 K were generated by quenching the 800 K structures at 5 K/ps followed by the relaxation at 1 atm pressure with the same convergence criterion. Coupling constants for temperature and pressure were 0.1 ps and 1 ps, respectively, throughout the study. Figure 5.1 shows 2D snapshots of relaxed structures of

$Ni_{63}Al_{37}$, PXP, and SXP at 600 K. Atoms are color-coded according to polyhedral template matching (PTM) analysis [141] which is implemented in LAMMPS [138] to identify different phases. PTM classifies structures according to the topology of the local environment and identifies each atom as BCC (identified as austenite in this study), HCP (martensite), FCC (stacking fault), and unidentified (grain boundaries). OVITO [142] is used for visualization. Blue and light blue colors represent atoms with BCC ordering (austenite) for matrix and precipitates, respectively. Green and light green colors represent atoms with HCP (martensite) and FCC (stacking Faults) ordering, respectively. Black color is used for atoms with no ordering (grain boundary).

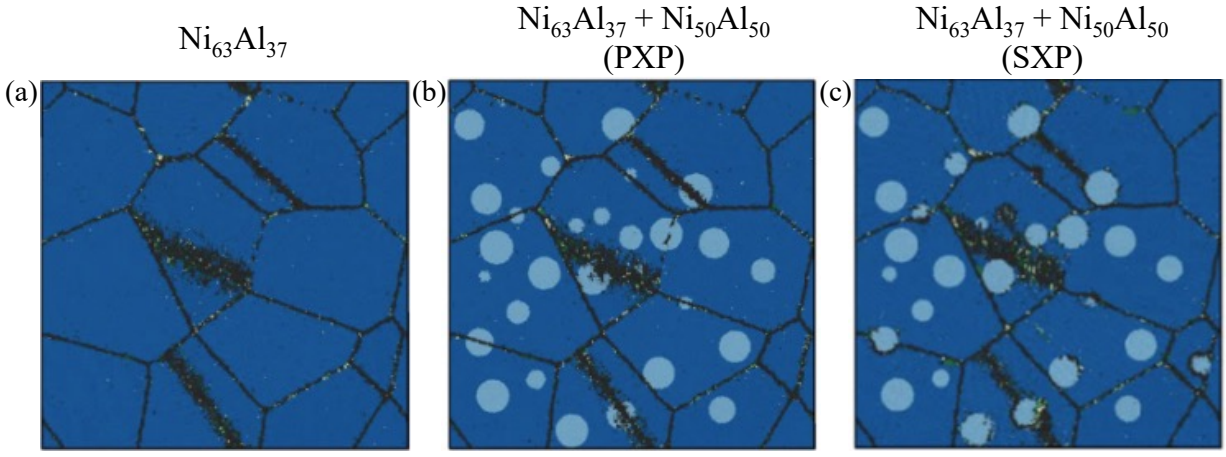

Figure 5.1. Snapshots of the 2D section of relaxed structures corresponding to (a) $Ni_{63}Al_{37}$, (b) $Ni_{63}Al_{37}$ + $Ni_{50}Al_{50}$ (PXP), and (c) $Ni_{63}Al_{37}$ + $Ni_{50}Al_{50}$ (SXP) at 600 K. Blue and light blue colors represent atoms with BCC ordering (austenite) for matrix and precipitates, respectively. Green and light green colors represent atoms with HCP (martensite) and FCC (stacking Faults) ordering, respectively. Black color is used for atoms with no ordering (grain boundary).

5.2.3 Stress and temperature-induced phase transformation

5.2.4 Stress-strain response during cyclic loading

The stress-induced martensitic transformation was characterized by elongating the simulation cell along the tensile axis (chosen to the z cartesian direction) up to 4% strain

with a strain rate of 5x10^7 s^{-1}. The lateral dimensions and angles in the simulation cell were evolved to maintain a stress of 1 atm using a Nose´-Hoover barostat, and the temperature was controlled using a Nosé-Hoover thermostat. The subsequent unloading and equilibration simulations were performed under stress-controlled conditions to unload the stress to 1 atm over 800 ps followed by relaxation for additional 1000 ps. These unloaded and relaxed structures were used for subsequent cycles of loading. To characterize the role of the stress-strain history on the martensitic transformation, we performed five cycles of loading-unloading-relaxation, totaling 13 ns of simulation time for each sample.

To characterize irreversible processes responsible for plastic slip, we examined the evolution of the relative displacement of every pair of first and second nearest neighboring atoms at the beginning of each loading cycle, using a cutoff of 3.5 Å. In these systems, the peaks corresponding to the first and second nearest neighbors in the radial distribution function (g(r)) overlap, therefore, the cutoff was chosen corresponding to the first minima in g(r) that includes the first and second nearest neighbors. Details of the method can be found in Ref. [143]. To study the temperature-induced martensitic transformation, the relaxed structures at 600 K and 1 atm were cooled down to 1 K at a rate of -0.5 K/ps using an isothermal-isobaric ensemble. Cell parameters, including angles, were allowed to vary independently to maintain a stress of 1 atm. The low-temperature structures were heated above the austenite finish temperature at a heating rate of 0.5 K/ps. We studied the temperature-induced martensitic transformation on the initial structures and the relaxed structures after completion of the fourth loading-unloading-relaxation cycle for all three systems.

5.3 Stress induced transformation

In all simulations, we observe significant evolution in the stress-strain and martensitic fraction behavior as a function of strain from cycle 1 to cycle 2, as shown in Figure 5.2 for various loading/unloading cycles at 600 K. We attribute this to incomplete relaxation of the initial structures due to the timescales achievable with MD and additional relaxation occurring during loading, especially at grain boundaries. Therefore, all subsequent analysis focuses on cycles 2 to 5.

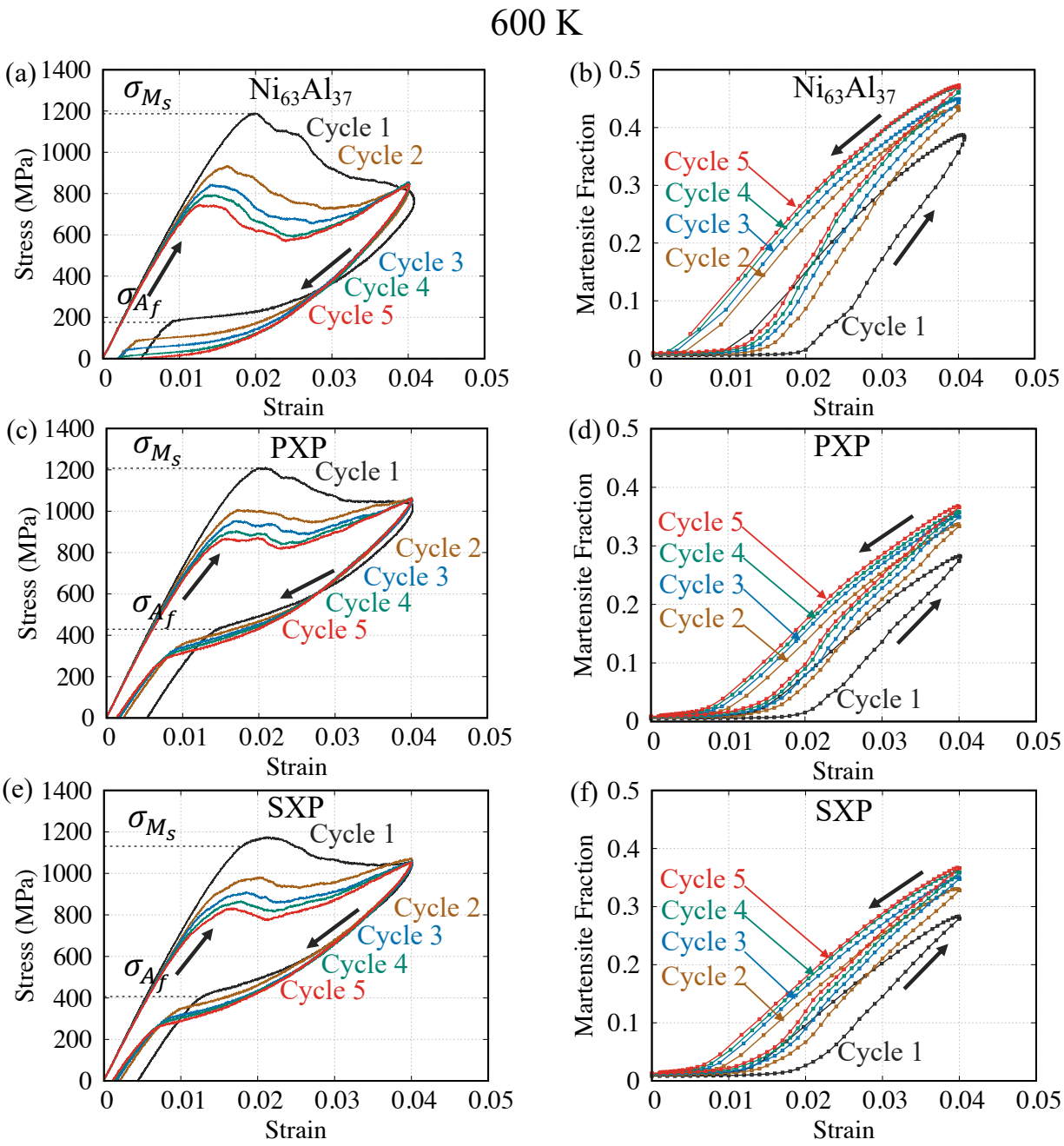

Figure 5.2. Stress (a, c, e) and martensite fraction (b, d, f) as a function of strain for various loading/unloading cycles of $Ni_{63}Al_{37}$ (a, b), PXP (c, d), and SXP (e, f) at 600 K. Direction of arrows represent loading (upward) and unloading (downward) directions.

We observe significant degradation in the stress-strain response of single-phase $Ni_{63}Al_{37}$, and this is consistent with experimental observations on fine-grain (110 nm) NiTi SMA [58]. The presence of precipitates results in significant stabilization of the stress-strain response upon cyclic loading compared to a system with no precipitates. This is consistent with experimental results on Ni-Ti-Cu shape memory alloys showing ultra-low functional fatigue [56] with the incorporation of Ti_2Cu nano-precipitates.

In all samples, we observe a reduction in both the σ_{M_s} (forward transformation) and σ_{A_f} (reverse transformation) during cyclic loading, indicating the relative stabilization of martensite with loading history. However, the relative change in σ_{A_f} is significantly larger in single-phase $Ni_{63}Al_{37}$; this eventually leads to incomplete reversible transformation for the fifth loading/unloading cycle. Contrarily, the presence of precipitates stabilizes the stress-strain response, especially during the reverse transformation, and a minimal change in σ_{A_f} is observed between cycle 2 and cycle 5 for the PXP and SXP samples. The extent of martensitic transformation during loading increases with increasing cycles, see Fig. 5.2(b, d, f). This phenomenon is commonly observed in experimental studies and is known as pre-training. By design, both types of precipitates stabilize the austenite phase, and their presence reduces the extent of martensitic transformation relative to single-phase $Ni_{63}Al_{37}$. Importantly, the presence of precipitates significantly increases the austenite finish stress, improving the reversibility of the pseudo-elastic deformation. The effect of precipitates on the σ_{M_s} is less dramatic. The atomistic mechanisms behind these trends will be discussed in section 5.3.1.

At 800 K, the increase in temperature reduces the extent of martensitic transformation and superelasticity due to the increased austenite stability, as shown in Figure 5.3 by the stress and the martensitic fraction as a function of strain for various cycles at 800 K. Like at 600 K, the extent of martensitic transformation during loading also increases with increasing loading/unloading cycles, and the presence of precipitates stabilizes the austenite phase and reduces the extent of martensitic transformation. However, at 800 K, the effect of temperature on austenite stabilization dominates, and the effect of precipitates on the reversibility of the pseudo-elastic deformation is minimal. We will focus on the results at 600 K in the remainder of the paper.

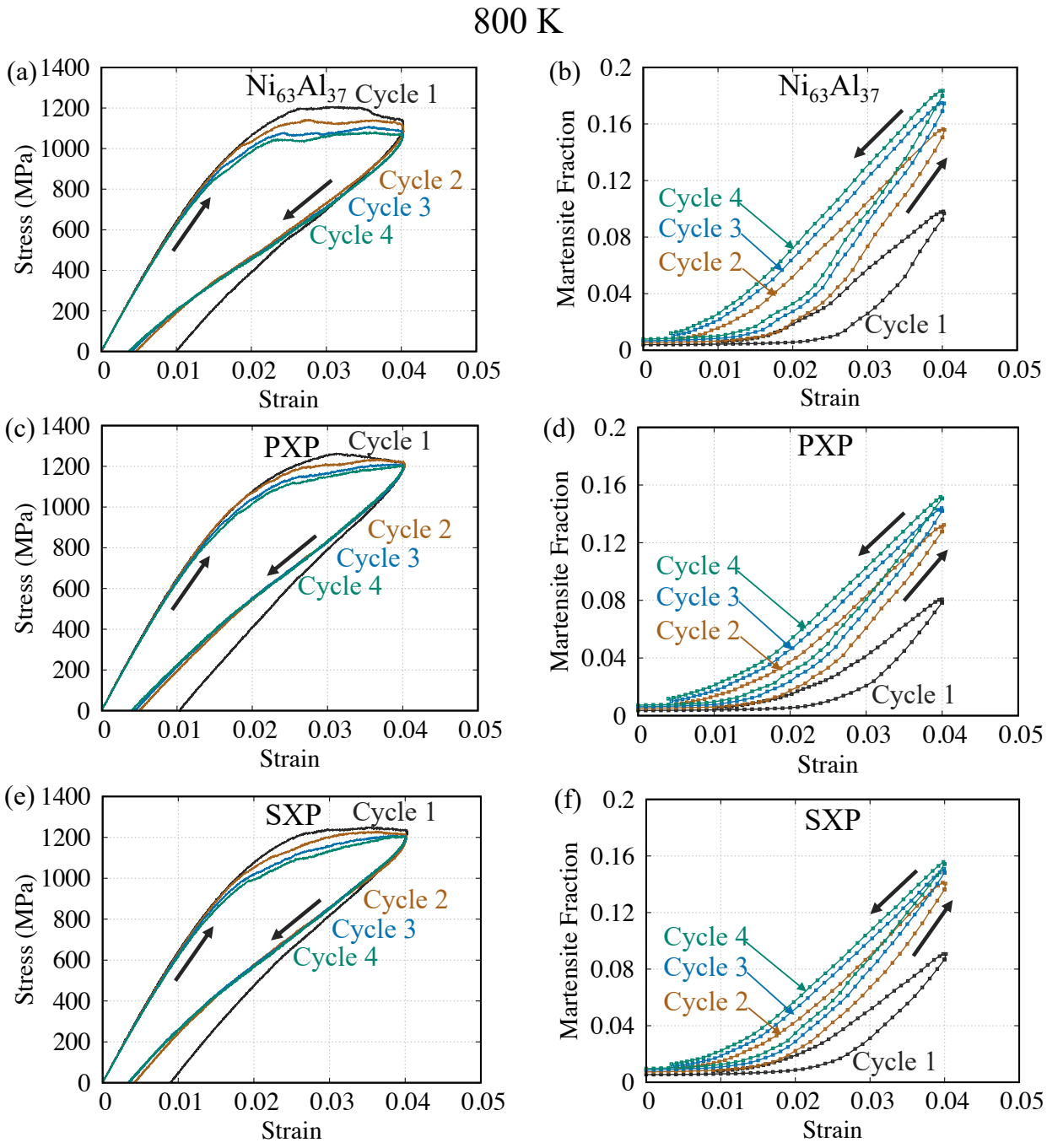

Figure 5.3. Stress (a, c, e) and martensite fraction (b, d, f) as a function of strain for various loading/unloading cycles of $Ni_{63}Al_{37}$ (a, b), PXP (c, d), and SXP (e, f) at 800 K. Direction of arrows represent loading (upward) and unloading (downward) directions.

Figure 5.4 compares the stress and martensite fraction as a function of strain between the three samples for the fifth loading/unloading cycle at 600 K. The presence of precipitates significantly reduces the rate of martensite propagation during loading but has a minor effect on the initiation of the transformation. Importantly, precipitates have a pronounced effect on the reverse transformation. The stress-strain response for PXP and SXP are rather similar.

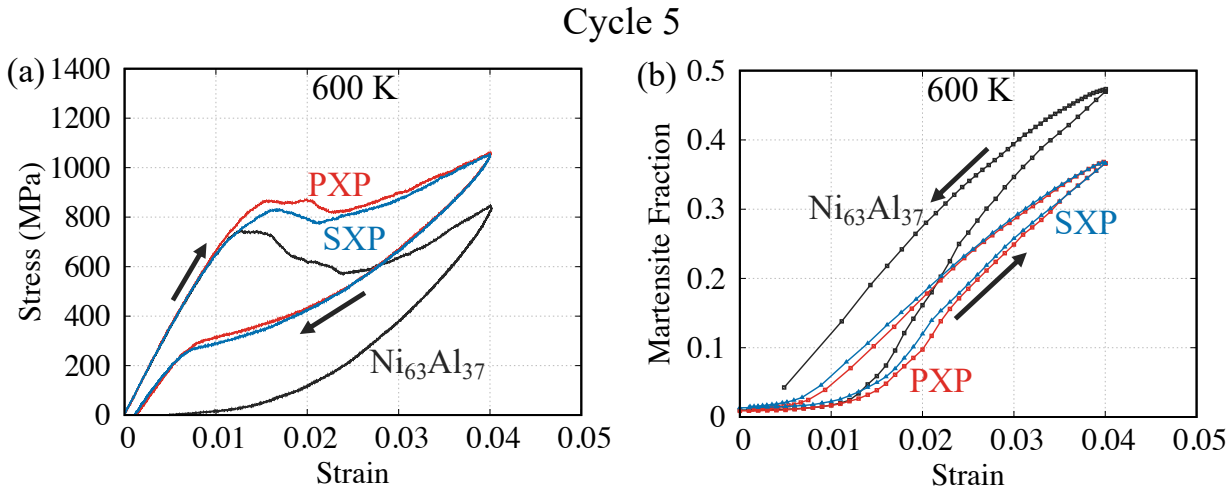

Figure 5.4. (a) Stress and (b) martensite fraction as a function of strain during the fourth cycle of uniaxial deformation to 4% strain for various samples followed by unloading to 1 atm stress at 600 K. Direction of arrows represent loading (upward) and unloading (downward) directions.

Experimental studies [56], [144] have shown that the presence of coherent precipitates in SMAs can reduce mechanical hysteresis. To confirm this behavior and understand the effect of cyclic loading on mechanical hysteresis for all three systems, we compare the area encircled by the cyclic stress-strain curves for various cycles, see Figure 5.5. As expected, both types of precipitates reduce the hysteresis. In addition, we observe a reduction in hysteresis with increasing cycles and a decrease in the relative change between cycles with increasing cycle number.

The presence of remnant strain is indicative of irreversible processes and can be observed in stress-strain response during cyclic loading for all the systems, see Fig. 5.2 (a, c, e). There are two possible origins for this irreversibility: i) remnant martensite that does not transform back to austenite, and ii) irreversible processes at the atomic scale via dislocation

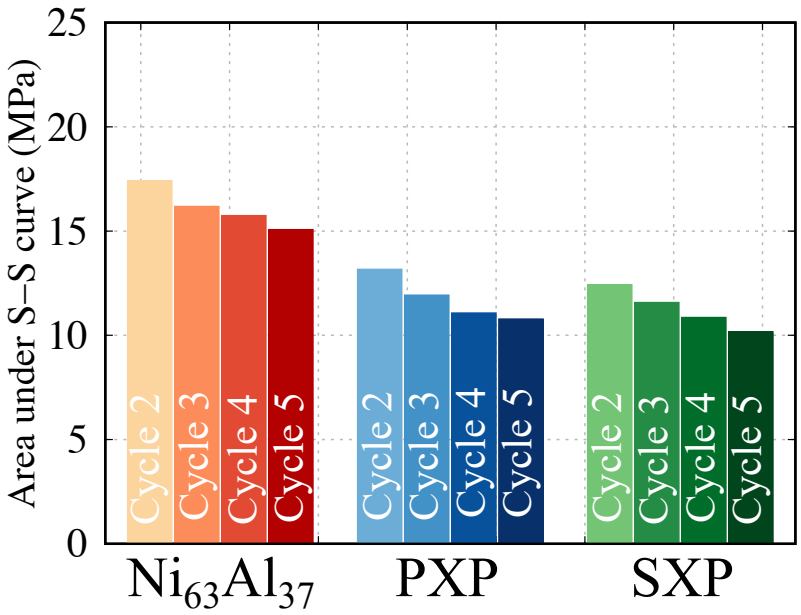

Figure 5.5. Area under stress-strain (S-S) curves of $Ni_{63}Al_{37}$, PXP, and SXP for various loading/unloading cycles (Cycle-2 to Cycle-5) at 600 K

slip and/or grain boundary sliding. To quantify the second possibility, we examined the evolution of the relative displacement of every pair of first and second nearest neighboring atoms as discussed in section 5.2.2. Figure 5.6 shows the histogram of the distances after a single loading-unloading cycle for various cycle numbers at 600 K. The pairs undergoing displacements of more than 1.6 Å (first minima of the number of pairs vs distance) are considered as irreversible plastic events [143]. We find that the total number of irreversible events decreases with increasing cycles. To quantitatively compare the relative impact of irreversible processes for various systems during cyclic loading, we define the total displacement in irreversible atomic events (D_{IAE}) as the sum of distances for all the pairs which undergo irreversible processes. We note that this is a scalar quantity that does not provide information about the total plastic slip on individual systems.

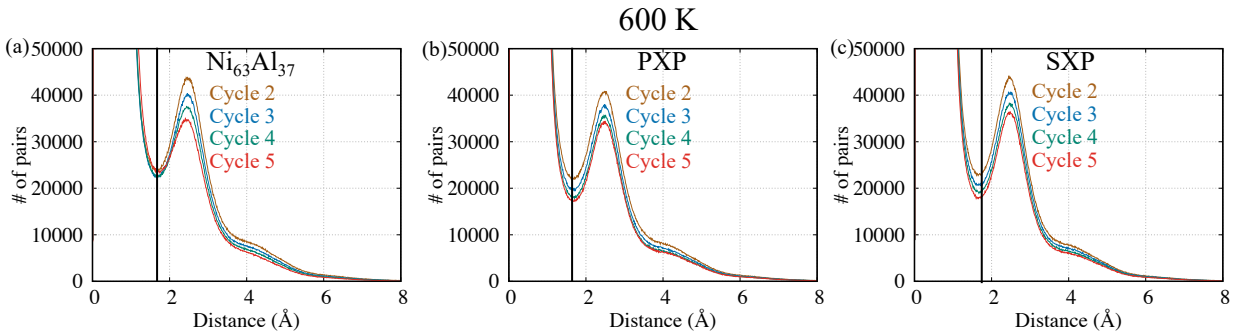

Figure 5.6. Histogram of the distances in structures after loading-unloading cycle for various cycles of (a) $Ni_{63}Al_{37}$, (b) PXP, and (c) SXP at 600 K

To understand the mechanisms that dominate the remnant strain, Figure 5.7 compares remnant strain, remnant martensite, and D_{IAE} during cyclic loading for all three systems. Interestingly, the remnant strain increases with increasing cycles for systems with no precipitates, but it decreases for PXP and SXP, see Figure 5.7 (a). The increase of remnant strain in the system without precipitates is dominated by the degradation of the reverse martensitic transformation since the D_{IAE} decreases with cycle number. Quite interestingly, the presence of precipitates stabilizes the reverse transformation, and the remnant martensitic fraction is relatively constant with cyclic loading.

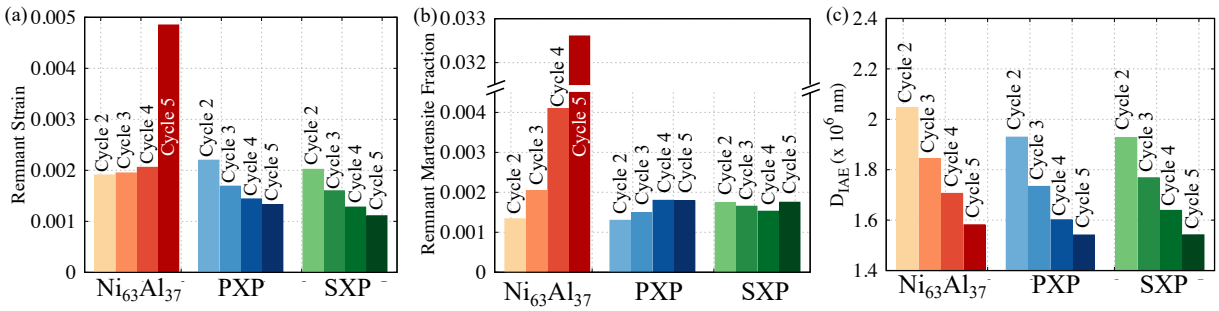

Figure 5.7. (a) Remnant strain along loading direction, (b) remnant martensite fraction, and (c) D_{IAE} during cyclic loading of $Ni_{63}Al_{37}$, PXP, and SXP at 600 K. Reference structures is taken as the structures at the beginning of corresponding loading cycle.

The irreversible atomic processes in Fig. 5.6 can be further subdivided into dislocation glide and grain boundary sliding. Figure 5.8 highlights (in red) the atoms involved in irreversible processes during cycle 4 for the three systems at 600 K. The snapshots reveal that most irreversible events occur at grain boundaries, these grain boundary processes account for approximately 95% of all pairwise irreversible events and dominate the irreversible processes during cyclic loading. Interestingly, in the SXP, we also observe the presence of atoms involved in irreversible deformation at the incoherent interfaces between precipitates and the differently oriented matrix grain, see Figure 5.8 (c). The presence of precipitates suppresses atomic-scale irreversible events (number of pairs of atoms undergoing irreversible atomic processes) for both PXP and SXP compared to a single-phase system, see Figure A.6. However, the increase in the grain boundary area in the SXP case results in an increase in the pairs of atoms undergoing irreversible events compared to PXP.

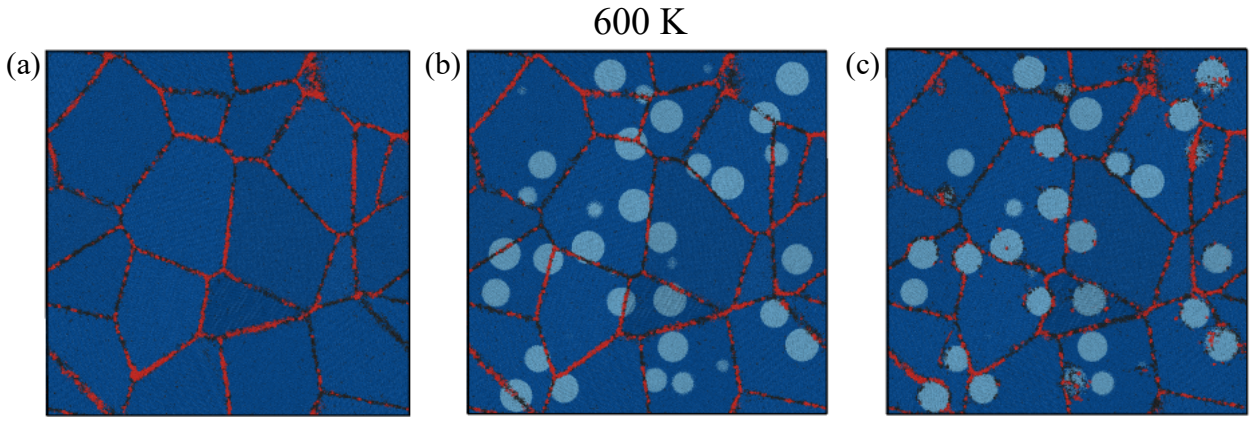

Figure 5.8. Snapshots of (a) $Ni_{63}Al_{37}$, (b) PXP, and (c, f) SXP showing atoms involved in irreversible atomic processes during Cycle-4 at 600 K. Red color is used for atoms involved in irreversible events. For remaining atoms, black color represent atoms with no local ordering (grain boundary); blue and light blue are used for the rest of the atoms in the matrix and precipitate, respectively.

5.3.1 Atomistic mechanisms underlying martensitic transformation

To understand the effect of precipitates on stress-strain stabilization, we now focus on the atomic-level processes underlying the nucleation and propagation of the martensitic and

reverse transformations. More specifically, we seek to address the following questions: What are the atomic processes responsible for the increase in transformation reversibility under the presence of precipitates? Why do precipitates have a smaller effect on σ_{M_s} than on σ_{A_f}?

Martensite start and nucleation of the martensitic transformation

To understand the relatively minor effect of the presence of precipitates on σ_{M_s}, we focus on the nucleation of the martensite phase. Figure 5.9 shows the process of martensite nucleation in a representative grain for all three systems at 600 K. We show snapshots at various times during cycle 4. Blue and light blue colors represent atoms with BCC ordering (austenite) for the matrix and precipitate, respectively. Green and light green colors represent atoms with HCP (martensite) and FCC (stacking faults) ordering in the matrix, respectively. Red and light red colors represent atoms with HCP (martensite) and FCC (stacking Faults) ordering in precipitates, respectively. Black is used for atoms with no crystalline ordering (grain boundary). We observe similar behavior in other grains. The snapshot at t=0 shows the remnant martensite and stacking faults from prior loading/unloading cycles, predominantly located near grain boundaries.

Martensite nucleation starts at t=240 ps for the selected grain, and we observe that the martensite phase nucleates at the grain boundaries for single-phase $Ni_{63}Al_{37}$ and PXP while for SXP grain boundaries and incoherent interfaces between the precipitates and differently orientated grains act as nucleation sites. We note that only a fraction of grain boundaries (those in contact with the matrix phase) will act as martensite nucleation sites for the systems with precipitates. We computed the effective grain boundary area for nucleation as the fraction of grain boundaries in the matrix phase, including the incoherent interfaces between precipitates and the matrix for SXP. The presence of precipitates, both in PXP and SXP, affects the effective grain boundary area for nucleation, however, due to the small number of precipitates lying on grain boundary, the change is relatively minor compared to single-phase $Ni_{63}Al_{37}$: an 11% reduction for PXP and 2% increment for SXP. This is consistent with the relatively minor effect of precipitates in σ_{M_s} and the observation in Fig. of earlier nucleation in the SXP system than in PXP.

To capture the influence of precipitates on martensite growth, Figure 5.9 also shows snapshots at various times (t=280 ps, 320 ps, 360 ps, 400 ps, 600 ps, and 800 ps) during loading following nucleation. As mentioned above, the austenite-stabilizing effect of precipitates reduces the rate of martensitic propagation during forward transformation and enhances the rate of reverse transformation. σ_{A_f} does not depend on the martensite nucleation site density and is only affected by the rate of reverse transformation or the austenite stabilizing behavior of precipitates. Therefore, we observe a significant change in σ_{A_f} due to the presence of precipitates in both PXP and SXP unlike σ_{M_s}. We discuss the partial structural transition in B2 precipitates driven by the martensitic propagation in the matrix and the influence of the precipitates on martensitic transformation in their surrounding matrix in next subsection.

Effect of precipitates on martensite propagation

Figure 5.10 shows snapshots of the structures before loading, after loading, and after unloading during cycle 4 at 600 K, and the color scheme is used that of Figure 5.9. The snapshots clearly reveal the shielding effect of the precipitates on the martensitic transformation, see center panels in Figure 5.10 (b, e, and h). The shielding effect was also observed around Ti_2Cu precipitate in Ni-Ti-Cu SMAs, where both austenite and martensite phases were found in the matrix near the precipitate/matrix interface compared to only martensitic phase in the matrix far from the interface [56]. However, quite surprisingly, regions within certain precipitates (composed on non-martensitic NiAl) are identified as martensitic. Thus, the transformation of the matrix induces ultra-high strains (approximately 12% deviatoric strain is needed to be identified as martensite) on some NiAl precipitates. This value of deviatoric strain was determined by deforming a 2,000 atom single-crystal supercell of B2 NiAl towards the martensite until 95% of the atoms are identified as martensitic by the PTM [141] analysis. A similar process was observed in coherent nanolaminates and core-shell nanowires [60].

To further characterize and quantify the shielding effect and the ultra-high deformation of precipitates, we quantify the martensite fraction identified in three regions: precipitates,

bulk matrix, and the matrix surrounding the precipitates (denoted as near-precipitate matrix (NPM)) within a cutoff of 5.58 Å. The cutoff is chosen to match the force cutoff in the Ni-Al EAM force field [136] used in this study. Figure 5.11 shows the martensitic fraction as a function of strain for precipitates, NPM, and matrix for various cycles of loading/unloading of PXP and SXP at 600 K. The curves for the matrix and NPM show the expected hysteresis, with NPM exhibiting a 30% reduction in transformation relative to the matrix. Quite interestingly, even when the precipitates are severely deformed into the martensitic phase, they experience negligible hysteresis. That is, the highly but elastically deformed precipitates spring back into their unstrained austenite phase and help drive the reverse transformation of the system. We note that Chluba et al. [56] did not find any structural transition in the Ti_2Cu precipitate during cyclic deformation of Ni-Ti-Cu SMAs experimentally, however, they only show analysis for a single precipitate. We also observe that approximately 30% precipitates undergo negligible structural transition, the histogram of identified martensitic fraction in precipitates for SXP during the fourth cycle is shown in Figure A.7. We did not find any correlation between the fraction of martensitic precipitates and various characteristic properties of the crystals they belong to like crystal orientation, stress invariants, potential energy, and the fraction of atoms with no ordering (grain boundary) for the precipitates.

5.4 Temperature induced transformation

Section 5.3 showed that both kinds of precipitates stabilize the austenite phase during stress-induced transformation. Here, we characterize the effect of precipitates on the temperature-induced transformation and the influence of prior mechanical loading history for all three systems. Figure 5.12(a) shows martensite fraction as a function of temperature during cooling and heating for $Ni_{63}Al_{37}$, PXP, and SXP using the relaxed structure at 600 K before Cycle-1 as initial conditions. We find a thermal hysteresis of approximately 300 K in single-phase $Ni_{63}Al_{37}$; this is significantly higher than experimentally reported values for various SMAs. For example, the values of thermal hysteresis are 15 K for $Ni_{64}Al_{36}$ and $Ni_{49.8}Ti_{50.2}$ [19], [20], 50 K for $Ti_{74}Nb_{26}$ and $Mg_{80.8}Sc_{19.2}$ [18], [21], 21 K for $Ni_{58}Al_{26}Fe_{16}$ [22], and 150 K for $Fe_{43.5}Mn_{34}Al_{15}Ni_{7.5}$ [23]. However, our value is consistent with a pre-

vious MD study of nano-crystalline $Ni_{63}Al_{37}$ SMA [134]. The larger hysteresis in MD can be attributed to a significantly higher heating/cooling rate (0.5 K/ps), which is expected to suppress the M_s and increase the A_f temperatures. Our goal is to characterize the effect of precipitates and mechanical history on transformation characteristics rather than predicting the absolute values.

As expected, precipitates stabilize the austenite phase, and the extent of martensitic transformation during cooling is significantly lower than the single-phase system. SXP is found to have a slightly higher Ms than single-phase $Ni_{63}Al_{37}$, which is unexpected since the precipitates are austenite stabilizing and expected to reduce both M_s and A_f . We attribute this increment to relatively more nucleation sites arising from the presence of only partially relaxed incoherent interfaces between precipitates and differently oriented grain. As expected, the presence of precipitates in PXP and SXP significantly reduces the A_f.

To understand the effect of loading history on temperature-induced martensitic transformation, we performed the same cooling-heating cycles on relaxed structures at 600 K after mechanical cycle-4. The martensite fraction as a function of temperature is shown in Figure 5.12 (b). The prior loading history results in the stabilization of the martensite phase, increasing the M_s and A_f. Moreover, the effect of incoherent interfaces between precipitates and differently-oriented grains diminishes because the initial structure has undergone various relaxation cycles during prior cyclic loading. Therefore, both PXP and SXP have reduced M_s and A_f temperatures compared to single-phase $Ni_{63}Al_{37}$. Like the case of the stress-induced martensitic transformation, the effect is less dramatic for Ms. Compared to single-phase Ni63Al37, the presence of precipitates reduces the thermal hysteresis by 42% (37%) and 50% (50%) for relaxed structures at 600 K after Cycle-4 (before Cycle-1) for PXP and SXP, respectively. Figure 5.13 shows the snapshots of structures at various temperatures (600 K, M_s, 1 K, and A_f) during cooling (600 K and M_s) and heating (1 K and A_f) for the initial structure relaxed at 600 K after Cycle-4 of cyclic loading. At 600K (Figure 5.13 (a, e, i)), all the structures are predominantly austenite with some remnant martensite at grain boundaries and at the interface of precipitates and differently oriented grains (latter only for SXP). Like the stress-induced transformation, martensite preferentially nucleates at grain boundaries in the temperature-induced transformation, see Figure 5.13 (b, f, j), and

the precipitates shield the martensite propagation in their surrounding matrix while they undergo a partial structural transition (Figure 5.13 (c, g, k)). During heating, all the systems revert back to the austenite phase above A_f temperature.

5.5 Conclusions

We characterized the role of nanoscale precipitates on martensitic transformation and super-elasticity in nano-crystalline samples for the first time with atomic resolution using molecular dynamics. In particular, we studied the effect of nanoscale spherical $Ni_{50}Al_{50}$ precipitates on stress- and temperature-induced martensitic phase transformation in nanocrystalline $Ni_{63}Al_{37}$ shape memory alloys using multi-million-atoms molecular dynamics simulations. The presence of B2 precipitates results in a stable stress-strain response, while single-phase nanocrystals exhibit degradation of the reverse transformation during cyclic loading. Simulations revealed that the precipitates shield the martensitic transformation in the matrix and partially deform to an unstable martensite-like structure in an elastic manner. Both kinds of precipitates, one where the grain boundaries cut through precipitates (PXP) and a second case where precipitates are single crystals (SXP), are austenite stabilizing, and their presence reduces the extent of martensite transformation. Martensite nucleates at the grain boundaries, and the grain boundary area influences the stress and temperature associated with the start of martensitic transformation. While the remnant martensite fraction originating from poor reversibility determines the remnant strain for single-phase nanocrystalline $Ni_{63}Al_{37}$, irreversible plastic slip (grain boundary sliding) dominates for systems with nanoscale precipitates. In conclusion, our results provide detailed insight into the experimentally into the origins of experimentally reported characteristics of phase transformation in the presence of precipitates.

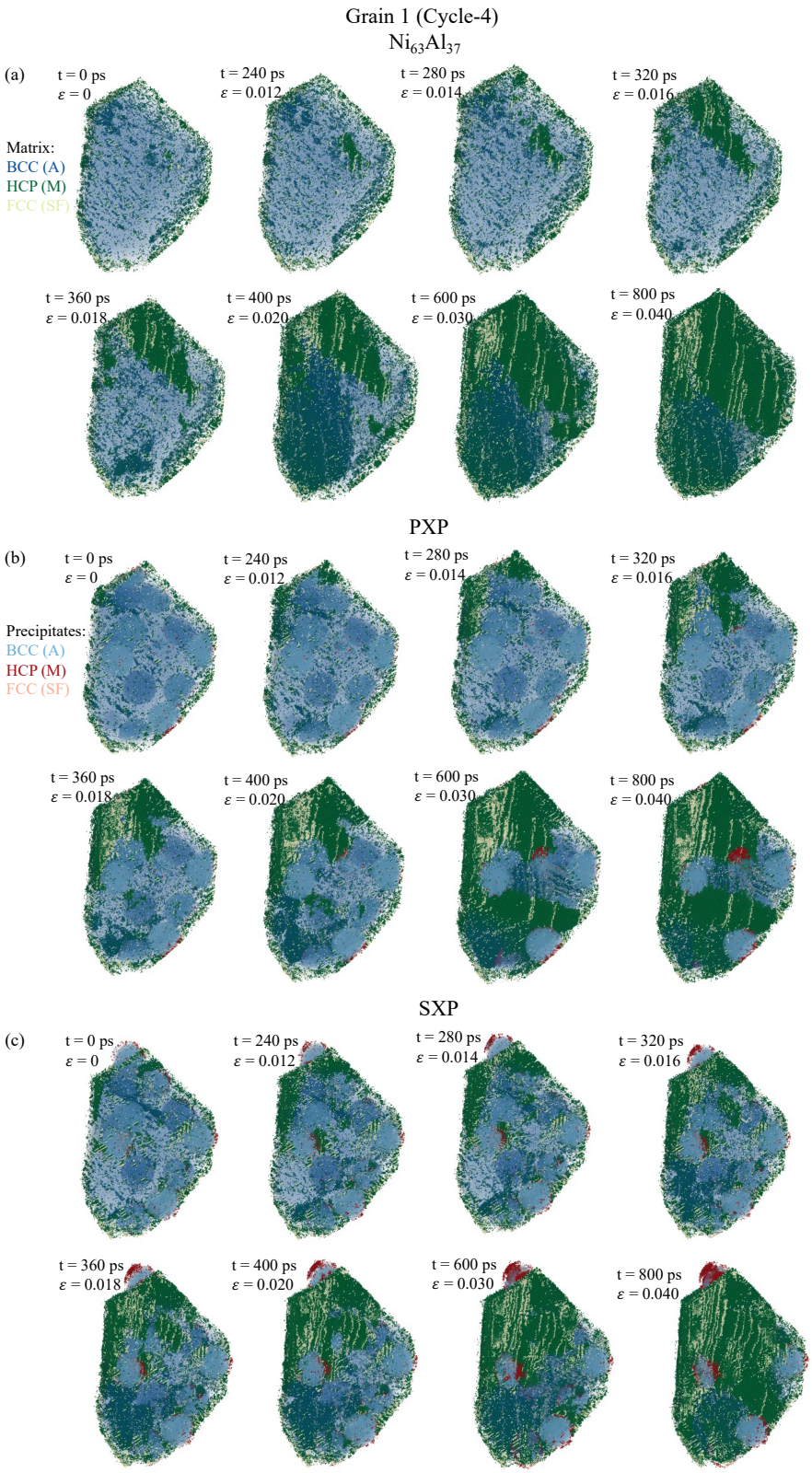

Figure 5.9. Snapshots of grain-1 at various times during the fourth loading cycle of (a) $Ni_{63}Al_{37}$, (b) PXP, and (c) SXP at 600 K.

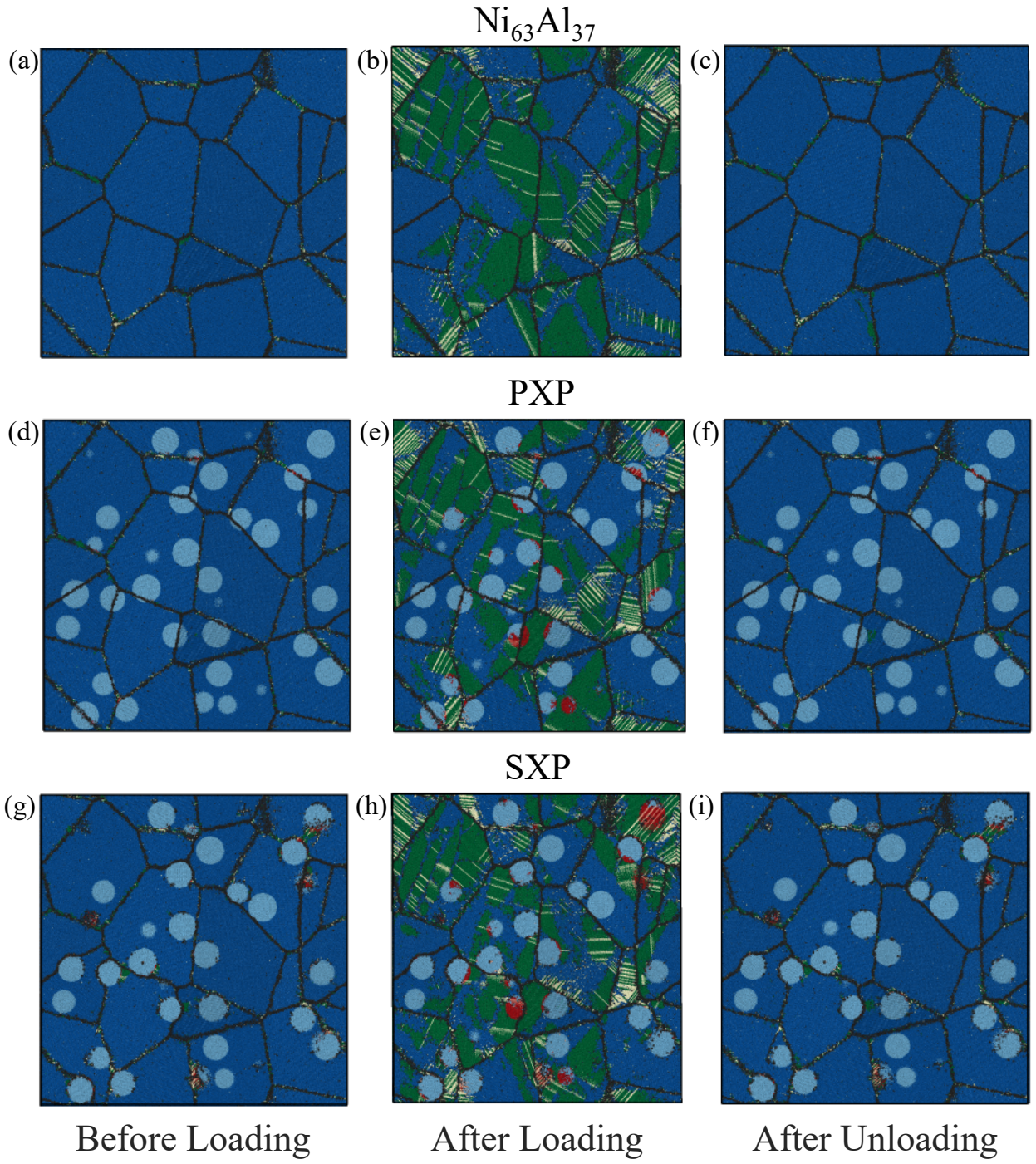

Figure 5.10. Snapshots of the structures at (a, d, g) before loading, (b, e, h) after loading, and (c, f, i) after unloading during cycle 4 for (a, b, c) $Ni_{63}Al_{37}$, (d, e, f) PPT-PX, and (g, h, i) PPT-SX at 600 K.

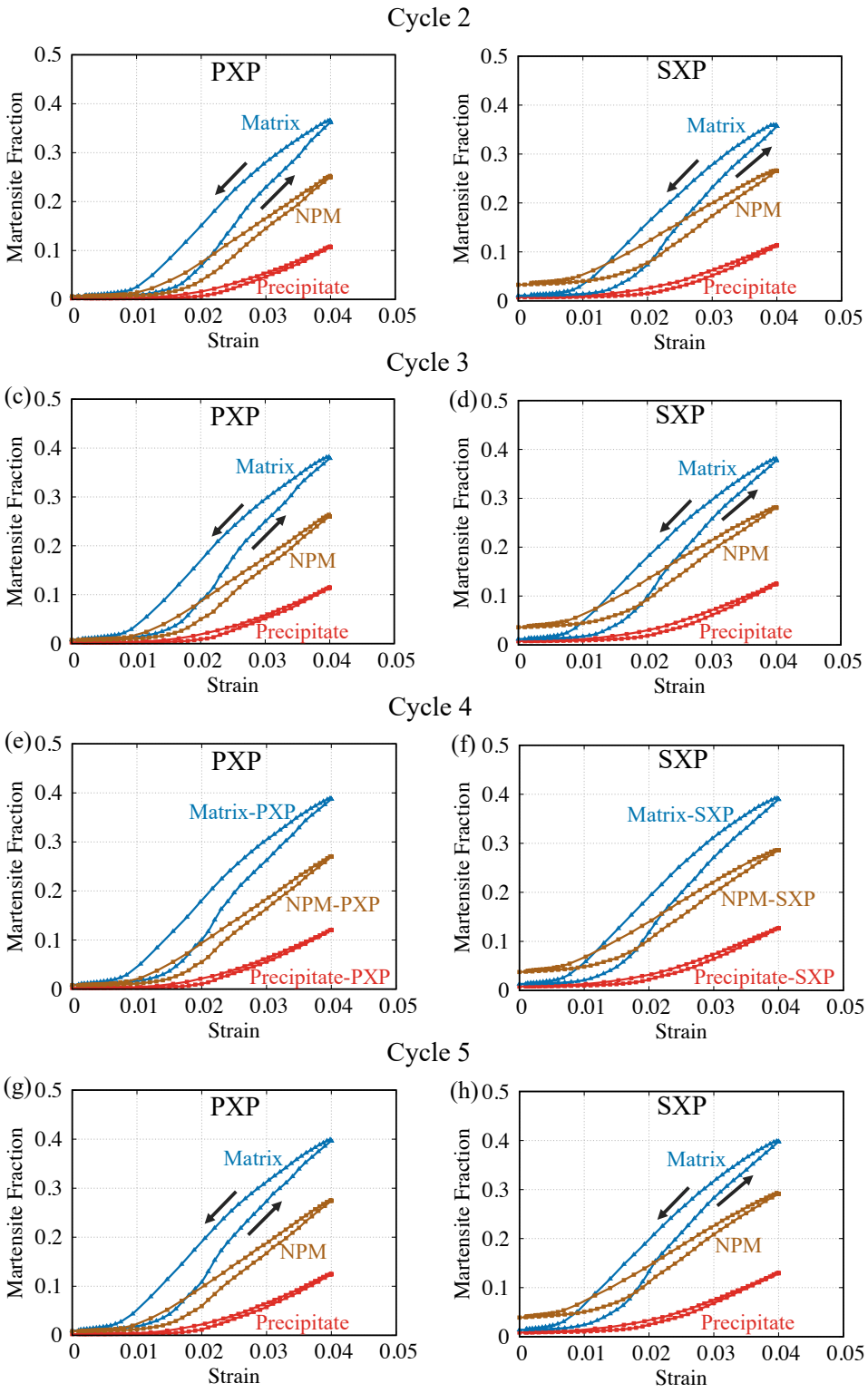

Figure 5.11. Martensite fraction as a function of strain in precipitates, matrix in vicinity of precipitates (NPM) and matrix during during loading/unloading cycles for PXP (a, c, e, g), and SXP (b, d, f, h) at 600 K.

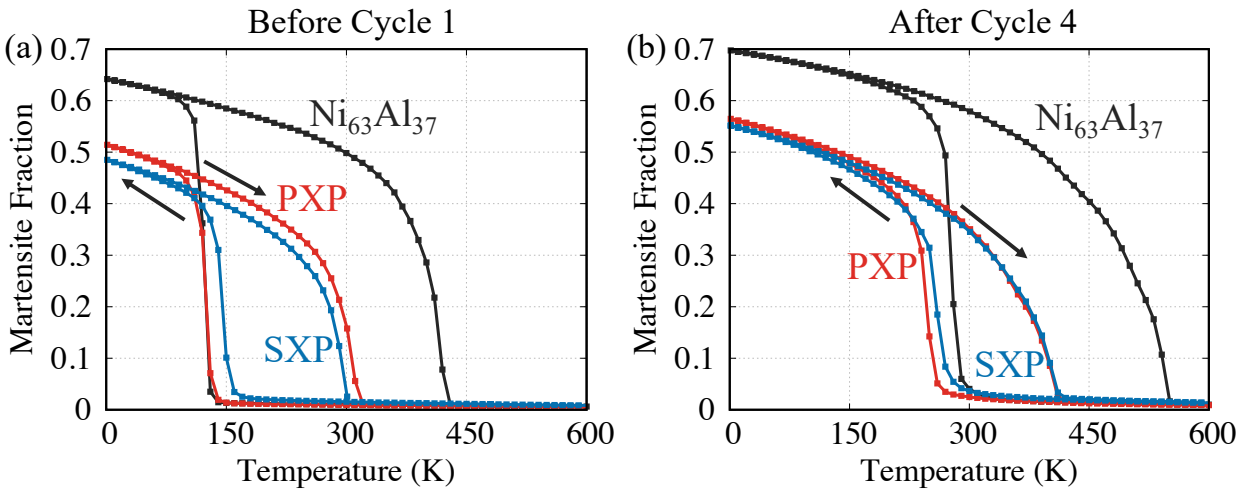

Figure 5.12. Martensite fraction as a function of temperature for heating-cooling cycles of $Ni_{63}Al_{37}$, PXP, and SXP for relaxed structure (a) before Cycle-1 and (b) after Cycle-4 during cyclic loading. The direction of arrows represents cooling (upward) and heating (downward) directions.

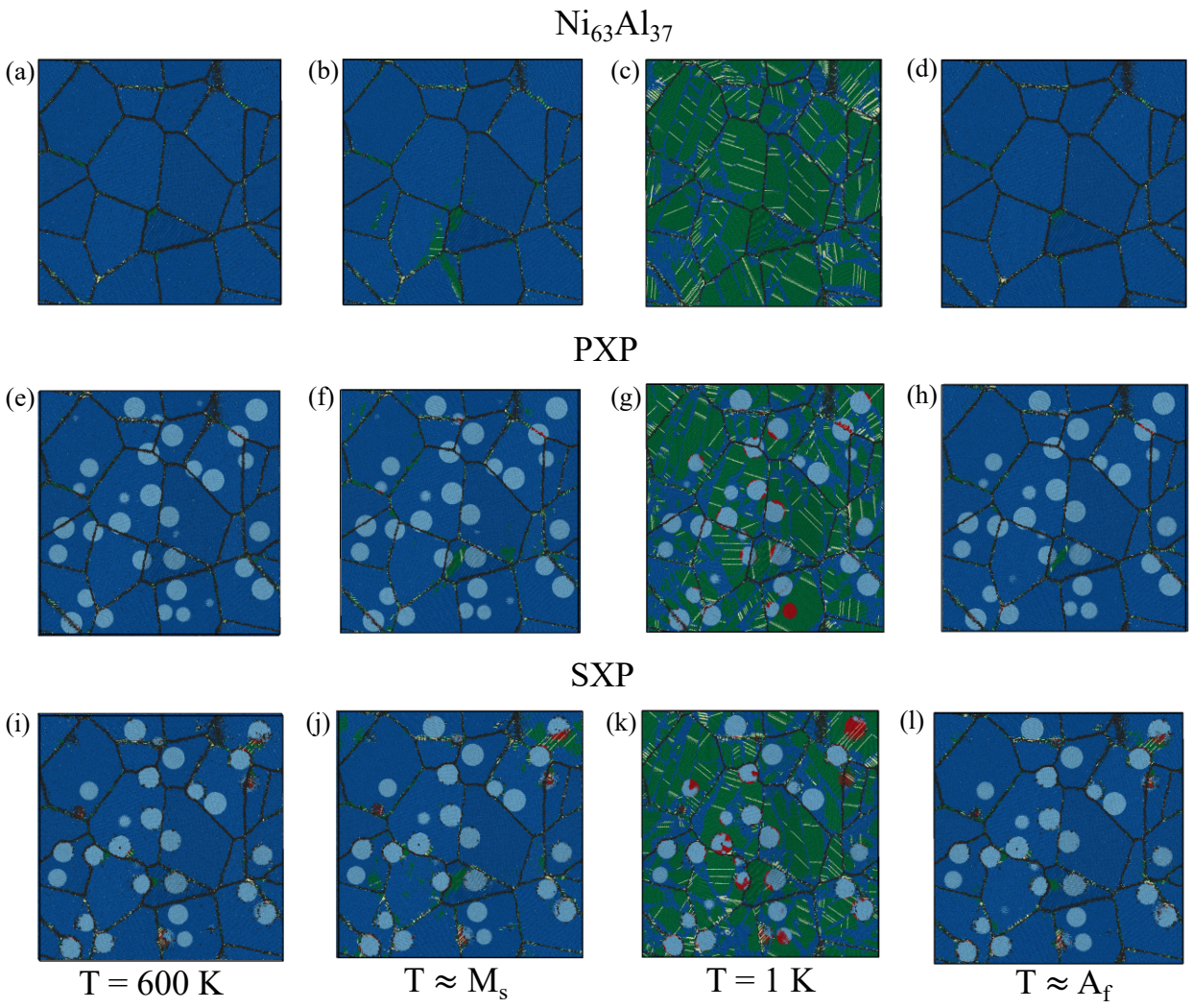

Figure 5.13. Snapshots of $Ni_{63}Al_{37}$ (a-d), PXP (e-h), and SXP (i-l) during cooling at 600 K (initial) (a, e, i), Ms (b, f, j), 1 K (c, g, k) and during heating at Af (d, h, l) for initial structure relaxed at 600 K after Cycle-4 of cyclic loading.

6. AUTOMATED APPROACH TO DISCOVER COHERENT PRECIPITATES IN MULTI-COMPONENT SHAPE MEMORY ALLOYS

This chapter was adapted from Shivam Tripathi, Lok C. Fan, Michael S. Titus, and Alejandro Strachan. "Automated approach to discover coherent precipitates in multi-component shape memory alloys." Computational Materials Science 197 (2021): 110651. Copyright 2021 Elsevier [145].

Coherent precipitates have a strong effect on martensitic transformations and can be used to tune properties and improve performance. However, only a small number of the possible martensitic matrix/precipitate combinations has been explored. Therefore, we developed an automated approach to discover possible coherent precipitates in a given base alloy of interest as well as the composition and processing conditions required to achieve the desired nanostructure. The software, denoted CohPhaseFind, couples high-throughput equilibrium thermodynamic calculations to identify coexisting phases with strain-based lattice matching based on ab initio simulations to assess coherency and orientation relationships. We demonstrate CohPhaseFind to discover possible coherent precipitates in Ni-Ti, Ni-Ti-X (X=Al, Cu and Hf) and Ni-Ti-Hf-Al alloys. We identify previously reported precipitates and new ones that merit exploration.

6.1 Introduction

Coherent precipitates result in extraordinary changes in the mechanical properties of metals and have been harnessed in a range of applications, from the Al alloys used by the Wright brothers [146]–[149] during the early days of aviation to today's gas turbine engines made of Ni-based superalloys [150]. Precipitation strengthening was first reported in Al alloys in 1901 [151], [152] and has since been utilized for various alloy systems [153]. Al-Cu-Mg based alloys strengthened by various coherent precipitates are among the first and the most widely studied systems owing to their use in automotive [154] and aerospace [155]. There has also been significant efforts in Ni-based super alloys [156]; $\gamma' - Ni_3Al$ precipitates

coherently dispersed in the γ matrix lead to superior mechanical properties [156], [157] in these alloys.

Coherent precipitates can also have a strong effect on materials that undergo martensitic transformations that underlie important phenomena including shape memory and superelasticity. Martensitic transformations are diffusion-less, solid-to-solid, transformations from a high-temperature and high-symmetry austenitic phase to a low-temperature and lower-symmetry martensitic phase. A subset of martensitic materials called SMAs exhibit quite remarkable properties. In their martensitic phase, they can recover their original shape upon heating after plastic deformation; in their austenite phase, they exhibit large, recoverable strains [1]. These thermo-mechanical properties make them useful in a wide range of applications.

Coherent precipitates in SMAs provide a relatively novel avenue to tune SMA properties and design alloys with unprecedented properties that remains to be fully explored and exploited. For example, Chluba et al. [56] showed experimentally that the presence of coherent Ti_2Cu precipitates in a NiTi austenitic matrix resulted in ultralow fatigue in a Ni-Ti-Cu based alloy. Elastically confined martensitic transformation was observed in Ti-Nb alloys as a result of nanoscale concentration modulation, which in turn resulted in superelasticity with a tunable Young's modulus over a wide temperature range [55]. In addition to experiments, various computational studies have shown that the presence of coherent second phases leads to unprecedent thermomechanical response in materials undergoing martensitic transformation [59], [61], [62], [80]. Guda Vishnu et al. [59] observed a significant reduction in the transformation hysteresis for superlattice or nanolaminate configurations of $Ni_{50}Al_{50}$ and $Ni_{63}Al_{37}$. Reeve et al. [62] also found that ultra-low stiffness (as low as 2GPa) can be achieved in a composite of $Ni_{50}Al_{50}$ and $Ni_{63}Al_{37}$ organized in core/shell nanowires and nanolaminates configurations.

Despite this enormous potential of coherent second phases for achieving novel properties in fully-dense materials, only few coherent second phases have been explored in shape memory alloys, and a systematic automated approach to design alloys exhibiting a coherent second phase that exists in equilibrium with the austenitic or martensitic phase of SMAs is lacking. There have been prior studies utilizing high-throughput thermodynamics and ab

initio calculations to discover alloys with novel properties [158]–[161]. For example, Senkov et al. [159] used high-throughput thermodynamics calculations to discover possible equiatomic multi-component alloys for high temperature structural applications. Hautier et al. [160] used high-throughput density functional theory calculations in combination with machine learning to discover new ternary oxides. MPInterface package developed by Mathew et al. [161] automates the high-throughput computational screening and generate interfacial structures for atomistic study. McClure et al. [162] combined ab initio and experimental data with transfer learning techniques to explore protective oxides for high-temperature applications. This paper introduces an automated approach, CohPhaseFind, to identify a set of coherent phases which are in equilibrium with matrix by coupling the high-throughput equilibrium thermodynamic calculations (section 6.2.1) with the strain-based lattice matching between the austenite matrix and coherent second phases (section 6.2.2). Section 6.3 exemplifies CohPhaseFind by exploring coherent second phases in NiTi-based shape memory alloys. We find the already-explored Ni_3Ti precipitate in the Ni-Ti system, Ti_2Cu precipitate in the Ni-Ti-Cu system, Ni_2TiAl precipitate in the Ni-Ti-Al system and $Ni_2Ti(Hf, Al)$ precipitate in the Ni-Ti-Hf-Al system. Additionally, we also discover coherent Ti (BCC and HCP) precipitates in NiTi; Ni_3Ti precipitate in Ni-Ti-Al; Ti (BCC and HCP), Cu, Ni_3Ti, Cu_3Ti_2, and Cu_4Ti to be coherent with NiTi matrix in Ni-Ti-Cu system. We stress that CohPhaseFind is generally applicable and can be used to discover coherent second phases in any multi-component alloy system.

6.2 Identifying possible coherent precipitates for martensitic matrices

The overall workflow consists of three main steps, see Figure 6.1. Step 1: For the base martensitic alloy of interest and possible alloying elements, CohPhaseFind performs phase equilibrium calculations over a broad temperature and composition ranges. Step 2 identifies composition and temperature ranges corresponding to two-phase regions where the matrix is predicted to coexist with the potential second phase. Finally, in Step 3, after identifying all possible two-phase alloys, CohPhaseFind down selects possible coherent precipitates from

a lattice matching procedure building on crystal structure information obtained from the Materials Project (MP) [102].

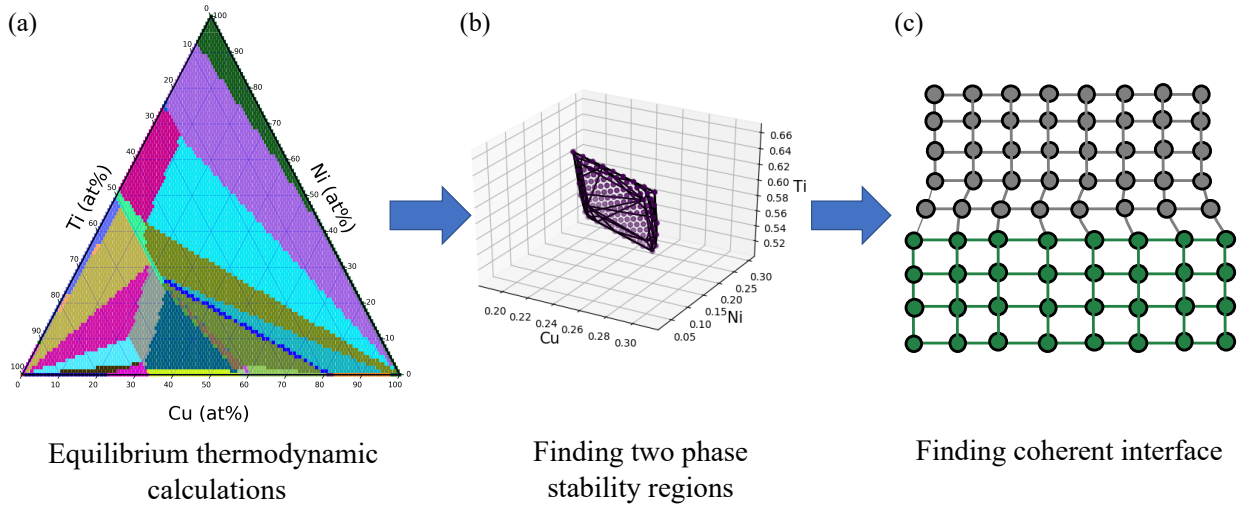

Figure 6.1. CohPhaseFind's automated workflow to identify the pairs of coherent equilibrium phases (a) Ni-Ti-Cu phase diagram at 973 K, (b) BCC_B2 and H_L21 phase stability region and (c) schematic of coherent interface between two phases

6.2.1 Thermodynamic calculations

We seek to find regions in the phase and temperature space of multi-component systems where the desired austenite matrix is in thermodynamic equilibrium with a coherent second phase. In order to obtain phase equilibria in multi-component system, we perform high-throughput single point equilibrium thermodynamic calculations using Thermo-Calc [163] via the TC-python framework by looping over various compositions and temperatures. Thermo-Calc determines phase equilibria by calculating and minimizing free energies of various phases at the given temperature and composition in a specified alloy system [164]. To explore composition and temperature space, we use a regular grid over the desired composition and temperature spaces of adjustable resolution. Calculations can be performed in parallel in order to reduce time to solution. We do this by slicing the composition and temperature space and assigning each region to different threads/cores. The slices are equally sized, and

the number of slices depends on the threads/cores available. Computed results are stored in JSON dictionaries.

As a verification test, we compared the ternary phases diagram of Ni-Ti-Al obtained from our package with one obtained directly from the Thermo-Calc GUI, see Figure 6.2. We used Thermo-Calc database TCNI8 (Ni based superalloys database) [165] for thermodynamic calculations. Our results indicate a larger number of distinct phase equilibria regions because some phase designations are arbitrarily defined and changed between two independent single-point equilibrium calculations (e.g. H_L21 split into H_L21#1 and H_L21#2). Keeping that aside, both phase diagrams are in good agreement with each other.

6.2.2 Screening for coherent phases

After identifying all two-phase regions, we need to select second phases likely to form coherent precipitates. We consider a criterion based on strain energy to assess the potential coherency between the base austenite and possible second phases. This requires crystal structure information. Unfortunately, this information is not available in the TC databases used for the thermodynamic calculations. However, the MP repository [102] has extensive crystal structure data from ab initio calculations, and CohPhaseFind uses this information to evaluate lattice strain energy via the MP API [102].

Matching the phase designation in Thermo-Calc with MP entries is not trivial, and Figure 6.3 shows the decision tree to find the lattice parameters of the stoichiometric phases from MP database.

Equilibrium phases obtained by Thermo-Calc possess crystallographic information in Strukturbericht notation. In order to match the crystallographic information of these phases with MP database, we convert Strukturbericht notation into space group number using aflowlib crystal database [166]. The second challenge is that the crystallographic information in MP is restricted to stoichiometric phases, while the equilibrium thermodynamic calculations often result in phases that deviate from the perfect stoichiometry used in MP for intermetallic compounds. Therefore, we map the resulting phases into stoichiometric ones based on sublattice information obtained from thermodynamic calculations performed

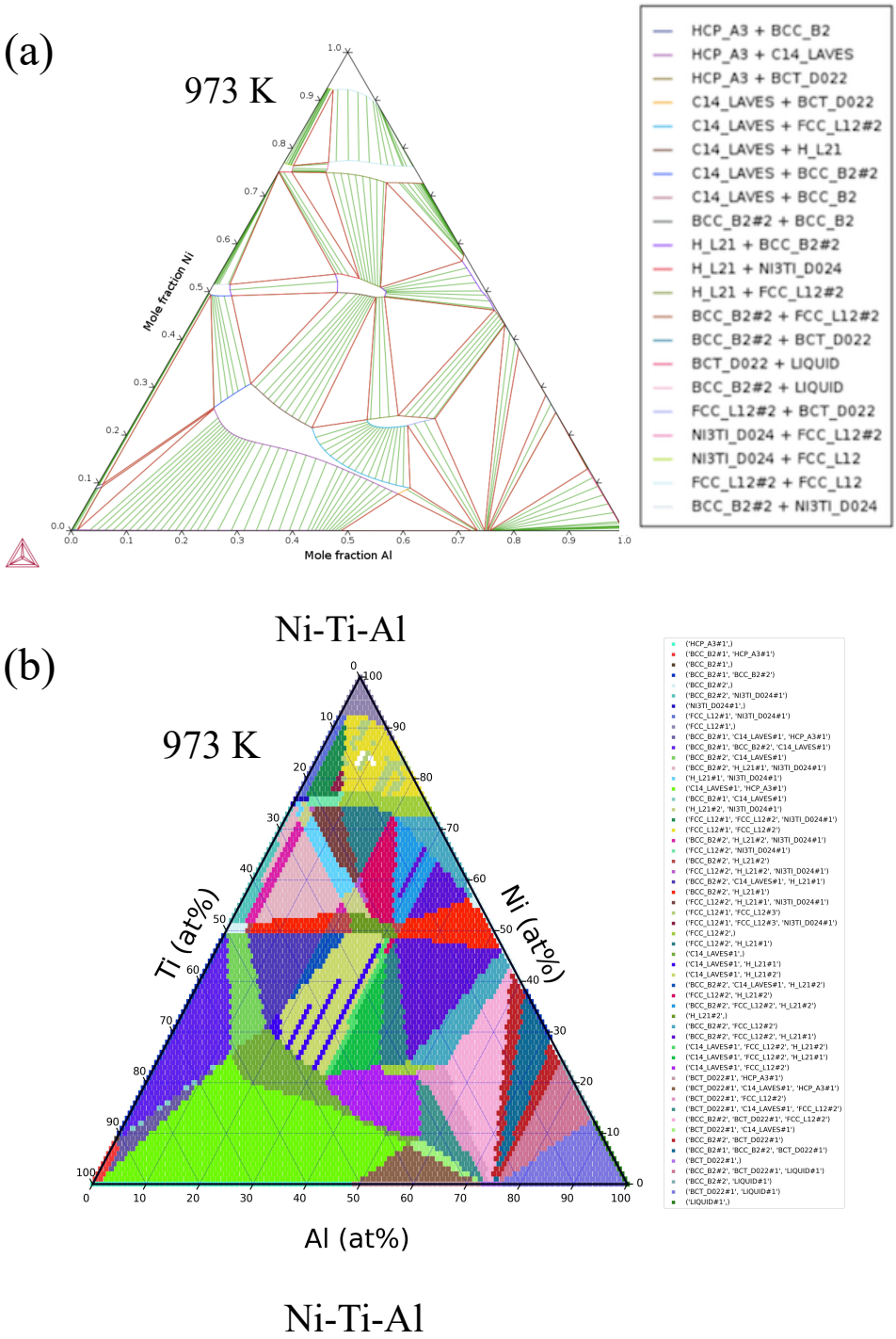

Figure 6.2. Phase diagrams of (a) Ni-Al-Ti (Thermo-Calc [163]) and (b) Ni-Al-Ti (CohPhaseFind) at 973 K

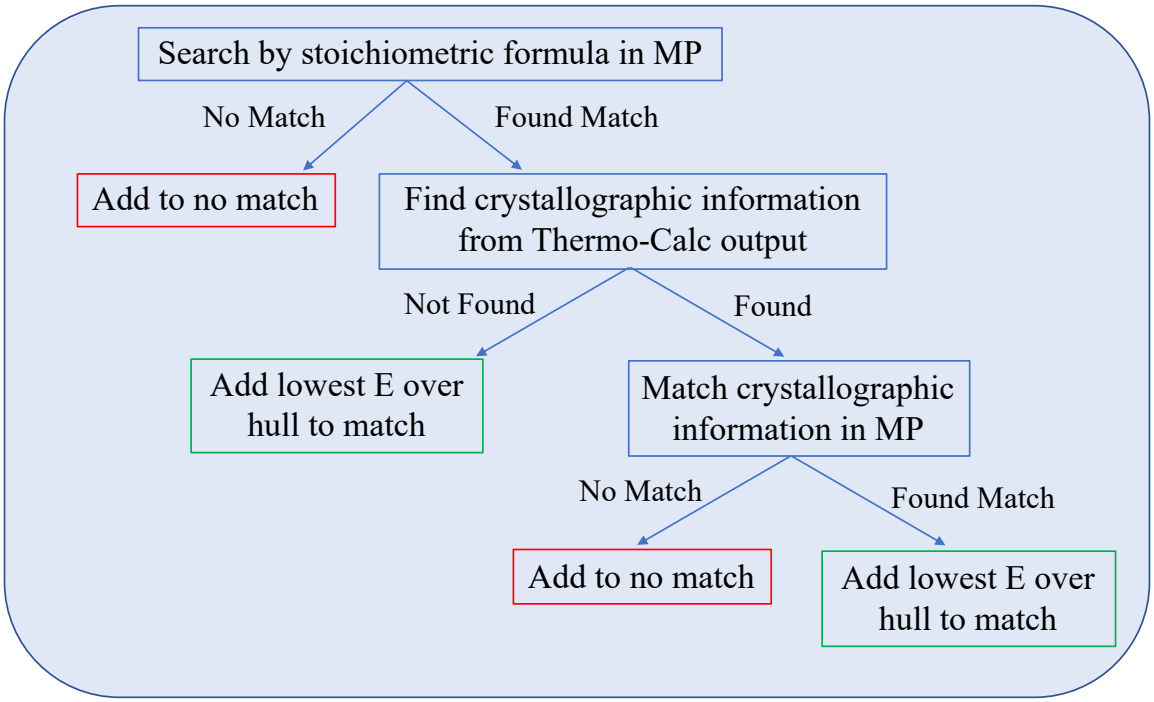

Figure 6.3. Decision tree to find the lattice parameter of stoichiometric composition from Materials Project [102]

via Thermo-Calc [163]. The nearest stoichiometric formulae for each phase is calculated as follows: i) we calculate the total number of moles of various elements within a phase using full alloy composition and phase fraction, ii) using these total number of moles of all the elements and sublattices composition, the relative fraction of each sublattice within a phase is calculated by solving simultaneous multi-variable linear equations, iii) these fractions are multiplied by the smallest common integer such that all of them become integer (n_{iXi}) to generate stoichiometric formula $(S^{iXi})_{n_{iXi}}$ (where i varies from 1 to N (total number of sublattices)) in terms of sublattices for all phases, and iv) we generate a set of elements-based stoichiometric formulae from each sublattice-based stoichiometric formula for each phase, by replacing sublattice S^i with elements which occupy more than 20% of sites of sublattice i.

The DFT-predicted lattice parameters of the closest compounds in MP are then used to calculate a strain-based criterion used for lattice matching using the substrate analyzer [167] package within the pymatgen framework to find the matching plane and in-plane matching superlattice vectors for a given pair of phases. Substrate analyzer matches a pair of crystal lattices in any given crystal direction by periodically reconstructing and rotating the interface to find a best match within the user specified matching criteria. This package also systematically searches for all possible crystal directions for matching within a specified criterion on Miller Indices. In our code, the maximum matching area and maximum allowed strain as a coherency criterion are adjustable. Based on this set of coherency criteria, a set of coherent coexisting pairs of equilibrium phases along with their matching plane can be obtained. Miller indices are allowed to vary between 0 to 3 for matching planes. We note that only lattice parameters are used here to find the coherent interfaces, and the significance of atomic packing is completely ignored in this analysis.

6.3 Example calculations: Coherent precipitates in NiTi SMAs

We now demonstrate CohPhaseFind to identify possible coherent precipitates in NiTi based SMAs, used commercially in a wide range of applications. Independent alloying additions of Al, Cu and Hf in Ni-Ti alloys have been shown to result in novel thermo-mechanical response [40], [51], [52], [54], [56], [168], [169]. Therefore, we look for possible coherent

second phases in binary Ni-Ti, ternary Ni-Ti-X (X=Al, Cu and Hf) and quaternary Ni-Ti-Hf-Al systems. We seek to identify second phases that have been experimentally observed as a validation along with possible additional, unexplored second phases. The TCNI8 [165] database in Thermo-Calc is used for equilibrium thermodynamic calculations for all the systems. The TCNI8 [165] database in our calculations does not have information about the experimentally observed Ti_2Ni phase which might alter the phase equilibria, therefore, the users are advised to look at the experimentally observed phase diagrams if available.

6.3.1 Ni-Ti system

Table 6.1 shows the input parameters used during equilibrium thermodynamic calculations and the screening of the coherent second phases for Ni-Ti system. The temperature and composition ranges are chosen such that the NiTi matrix is thermodynamically stable and plausible to undergo martensitic transformation.

Table 6.1. Input parameters for Ni-Ti system

Equilibrium Thermodynamic Calculations	
Temperature Range	773K-1473K
Temperature Step	50 K
Composition range for Ni and Ti (atomic fraction)	0-1
Composition Step (atomic fraction)	0.01
Screening Coherent Second Phases	
Matrix Phase	NiTi (B2)
Minimum fraction of matrix phase	0.5
Composition range of Ni in matrix (atomic fraction)	0.49-0.51
Composition range of Ti in matrix (atomic fraction)	0.49-0.51
Maximum allowed strain	5%
Maximum allowed matching area	100 $Å^2$

The set of second phases predicted to be coherent with NiTi (BCC_B2) are reported in Table 6.2. Table 6.2 contains the following information: i) stoichiometric formula and space group of the second phase, ii) matching planes between matrix and the second phase, iii) matching plane area and biaxial strain on the second phase, iv) alloying elements, mean composition and the temperature of alloy corresponding to the two-phase stability region. While biaxial matching of the second phase do suffice for epitaxy in nanolaminates, precipitates form multiple epitaxial interfaces in 3D. Therefore, we have multiple entries corresponding to same second phase with different matching planes, matching plane area and biaxial strain within a cutoff specified by the user. We believe that the matching interfaces in 3D will be a subset of these various matching planes reported in Table 6.2 for a specific second phase. We found Ti (both BCC and HCP) and Ni_3Ti to be coherent with NiTi. Ni_3Ti has been observed in experimental studies [170]. Unfortunately, our calculation misses the experimentally reported metastable Ni_4Ti_3 coherent second phase [170] since this phase is not available in our thermodynamic database.

Table 6.2. Predicted coherent second phases, denoted as SP in table, for NiTi (BCC_B2) matrix in Ni-Ti system. Composition and temperature represent mean value of those within the stability region of specific SP and matrix. * is used for coherent second phases which have been observed in prior experimental studies. ** is used for second phases which are predicted by Thermo-Calc and do not coexist with matrix in experimental NiTi phase diagram.

SP	**SP Space Group**	**Matrix Plane**	**SP Plane**	**Matching Area (Å^2)**	$(\epsilon_x^2 + \epsilon_y^2)$	**Composition (at. fraction) [Ni,Ti]**	**T (K)**
**Ti	P6_3 /mmc	(100)	(203)	71.68	$4.37\text{x}10^{-4}$	[0.38,0.62]	848
**Ti	P6_3 /mmc	(100)	(302)	44.80	$4.55\text{x}10^{-4}$	[0.38,0.62]	848
**Ti	P6_3 /mmc	(320)	(101)	32.3	$7.05\text{x}10^{-4}$	[0.38,0.62]	848
**Ti	P6_3 /mmc	(100)	(001)	44.80	$7.44\text{x}10^{-4}$	[0.38,0.62]	848
**Ti	P6_3 /mmc	(110)	(332)	76.02	$1.15\text{x}10^{-3}$	[0.38,0.62]	848
**Ti	P6_3 /mmc	(210)	(102)	20.03	$1.25\text{x}10^{-3}$	[0.38,0.62]	848
**Ti	P6_3 /mmc	(100)	(100)	26.88	$1.70\text{x}10^{-3}$	[0.38,0.62]	848
**Ti	P6_3 /mmc	(320)	(310)	96.91	$1.70\text{x}10^{-3}$	[0.38,0.62]	848
*Ni_3Ti	P6_3 /mmc	(332)	(100)	84.05	$1.02\text{x}10^{-3}$	[0.57,0.43]	823
*Ni_3Ti	P6_3 /mmc	(100)	(110)	71.68	$2.01\text{x}10^{-3}$	[0.57,0.43]	823
*Ti	$Im\bar{3}m$	(320)	(211)	96.91	$2.31\text{x}10^{-3}$	[0.40,0.60]	1023

6.3.2 Ni-Ti-X (X =Al, Cu and Hf) system

The input parameters used during equilibrium thermodynamic calculations and the screening of the coherent second phases for Ni-Ti-X (X = Al, Cu and Hf) are shown in Table 6.3. Al is found to substitute on both Ni and Ti sublattices while Cu and Hf is found to substitute on Ni and Ti sublattices, respectively, in the NiTi (BCC_B2) phase. The composition range for screening second phases was chosen such that the matrix is likely to undergo martensitic transformation.

Table 6.3. Input parameters for Ni-Ti -X (X = Al, Cu and Hf) system

Equilibrium Thermodynamic Calculations	
Temperature Range	773K-1473K
Temperature Step	50 K
Composition range for Ni, Ti and X (atomic fraction)	0-1
Composition Step (atomic fraction)	0.01
Screening Coherent Second Phases	
Matrix Phase	NiTi (BCC_B2)
Minimum fraction of matrix phase	0.5
Composition range of Ni in matrix (atomic fraction)	0.45-0.51 (Ni-Ti-Al)
	0.20-0.51 (Ni-Ti-Cu)
	0.49-0.51 (Ni-Ti-Hf)
Composition range of Ti in matrix (atomic fraction)	0.45-0.51 (Ni-Ti-Al)
	0.49-0.51 (Ni-Ti-Cu)
	0.20-0.51 (Ni-Ti-Hf)
Composition range of X in matrix (atomic fraction)	0.01-0.10 (Ni-Ti-Al)
	0.01-0.30 (Ni-Ti-Cu)
	0.01-0.30 (Ni-Ti-Hf)
Maximum allowed strain	5%
Maximum allowed matching area	100 $(Å)^2$

Tables 6.4, 6.5 and 6.6 show the set of second phases which are coherent with NiTi (B2) in Ni-Ti-Al, Ni-Ti-Cu and Ni-Ti-Hf system, respectively. We found Ni3Ti to be coherent with NiTi in Ni-Ti-Al and Ni-Ti-Cu system, this second phase has been experimentally reported for the binary Ni-Ti system. Experimentally characterized Ni_2TiAl and Ti_2Cu phases are also found for Ni-Ti-Al and Ni-Ti-Cu systems, respectively. Ni_2TiAl precipitates are shown to increase the strength of this alloy system [52], and Ti_2Cu precipitates are shown to reduce the functional fatigue in Ni-Ti-Cu [56]. Additionally, we also found Cu, Ti (BCC and HCP), Ti_2Cu, Ni_3Ti, Cu_3Ti_2 and Cu_4Ti to be coherent with the NiTi matrix in Ni-Ti-Cu. These precipitates have not been characterized so far and merit exploration. In Ni-Ti-Hf, we found Ti (BCC) to be coherent with NiTi matrix. We miss out on experimentally reported H phase due to the limitation imposed by database in our thermodynamic calculation as our database (TCNI8) does not have information on the H phase [165].

Table 6.4. Predicted coherent second phases, denoted as SP in table, for NiTi (BCC_B2) matrix in Ni-Ti-Al system. Composition and temperature represent mean value of those within the stability region of specific SP and matrix. * is used for coherent second phases which have been observed in prior experimental studies.

SP	**SP Space Group**	**Matrix Plane**	**SP Plane**	**Matching Area (Å^2)**	**$(\epsilon_x^2+\epsilon_y^2)$**	**Composition (at. fraction) [Al,Ni,Ti]**	**T (K)**
$^*Ni_2Ti-Al$	Fm$\bar{3}$m	(111)	(111)	62.07	5.52x10^{-4}	[0.08,0.50,0.42]	906
$^*Ni_2Ti-Al$	Fm$\bar{3}$m	(110)	(110)	50.68	5.52x10^{-4}	[0.08,0.50,0.42]	906
$^*Ni_2Ti-Al$	Fm$\bar{3}$m	(100)	(100)	35.83	5.52x10^{-4}	[0.08,0.50,0.42]	906
$^*Ni_3Ti$	P6_3/mmc	(332)	(100)	84.05	1.02x10^{-3}	[0.01,0.56,0.43]	823
$^*Ni_3Ti$	P6_3/mmc	(100)	(110)	71.68	2.01x10^{-3}	[0.01,0.56,0.43]	823

Table 6.5. Predicted coherent second phases, denoted as SP in table, for NiTi (BCC_B2) matrix in Ni-Ti-Cu system. Composition and temperature represent mean value of those within the stability region of specific SP and matrix. * is used for coherent second phases which have been observed in prior experimental studies.

SP	**SP Space Group**	**Matrix Plane**	**SP Plane**	**Matching Area (Å^2)**	**$(\epsilon_x^2 + \epsilon_y^2)$**	**Composition (at. fraction) [Cu,Ni,Ti]**	**T (K)**
Cu	Fm$\bar{3}$m	(110)	(110)	38.01	3.05x10^{-4}	[0.37,0.25, 0.38]	998
Cu	Fm$\bar{3}$m	(210)	(210)	60.10	3.05x10^{-4}	[0.37,0.25, 0.38]	998
Cu	Fm$\bar{3}$m	(110)	(221)	76.02	2.23x10^{-3}	[0.37,0.25, 0.38]	998
Ti	P6_3 /mmc	(100)	(203)	71.68	4.37x10^{-4}	[0.08,0.31, 0.61]	898
Ti	P6_3 /mmc	(100)	(302)	44.8	4.55x10^{-4}	[0.08,0.31, 0.61]	898
Ti	P6_3 /mmc	(320)	(101)	32.3	7.05x10^{-4}	[0.08,0.31, 0.61]	898
Ti	P6_3 /mmc	(100)	(001)	44.8	7.44x10^{-4}	[0.08,0.31, 0.61]	898
Ti	P6_3 /mmc	(110)	(332)	76.02	1.15x10^{-3}	[0.08,0.31, 0.61]	898
Ti	P6_3 /mmc	(210)	(102)	20.03	1.25x10^{-3}	[0.08,0.31, 0.61]	898
Ti	P6_3 /mmc	(100)	(100)	26.88	1.70x10^{-3}	[0.08,0.31, 0.61]	898
Ti	P6_3 /mmc	(320)	(310)	96.91	1.70x10^{-3}	[0.08,0.31, 0.61]	898

$^{*}Ti_2Cu$	I4 /mmm	(320)	(100)	32.3	4.45x10^{-4}	[0.24,0.21, 0.55]	948
$^{*}Ti_2Cu$	I4 /mmm	(100)	(001)	8.96	8.59x10^{-4}	[0.24,0.21, 0.55]	948
$^{*}Ti_2Cu$	I4 /mmm	(100)	(102)	35.84	9.26x10^{-4}	[0.24,0.21, 0.55]	948
$^{*}Ti_2Cu$	I4 /mmm	(320)	(101)	32.3	1.42x10^{-3}	[0.24,0.21, 0.55]	948
$^{*}Ti_2Cu$	I4 /mmm	(100)	(111)	44.8	1.42x10^{-3}	[0.24,0.21, 0.55]	948
$^{*}Ti_2Cu$	I4 /mmm	(100)	(212)	71.68	1.42x10^{-3}	[0.24,0.21, 0.55]	948
$^{*}Ti_2Cu$	I4 /mmm	(110)	(112)	50.68	1.96x10^{-3}	[0.24,0.21, 0.55]	948
$^{*}Ti_2Cu$	I4 /mmm	(100)	(223)	98.55	2.03x10^{-3}	[0.24,0.21, 0.55]	948
$^{*}Ni_3Ti$	P6_3 /mmc	(332)	(100)	84.05	1.02x10^{-3}	[0.02,0.54, 0.44]	798
$^{*}Ni_3Ti$	P6_3 /mmc	(100)	(110)	71.68	2.01x10^{-3}	[0.02,0.54, 0.44]	798
Ti	Im3m	(320)	(211)	96.91	2.31x10^{-3}	[0.04,0.37, 0.59]	1048
$^{*}Ti_2Cu_3$	P4 /mmm	(111)	(112)	62.07	2.37x10^{-3}	[0.35,0.18, 0.47]	973
$^{*}Ti_2Cu_3$	P4 /mmm	(110)	(103)	50.68	2.39x10^{-3}	[0.35,0.18, 0.47]	973
$^{*}Cu_4Ti$	Pnma	(110)	(103)	76.02	2.39x10^{-3}	[0.38,0.20, 0.42]	923

Table 6.6. Predicted coherent second phases, denoted as SP in table, for NiTi (BCC_B2) matrix in Ni-Ti-Hf system. Composition and temperature represent mean value of those within the stability region of specific SP and matrix.

SP	**SP Space Group**	**Matrix Plane**	**SP Plane**	**Matching Area (Å^2)**	$(\epsilon_x^2 + \epsilon_y^2)$	**Composition (at. fraction) [Hf,Ni,Ti]**	**T (K)**
Ti	$Im\bar{3}m$	(320)	(211)	96.91	$2.30x10^{-3}$	[0.13,0.48,0.39]	1193

6.3.3 Ni-Ti-Hf-Al system

Table 6.7 shows the input parameters used during equilibrium thermodynamic calculations and the screening of the coherent second phases. Hf is found to substitute on the Ti sublattice while Al substitutes on both Ni and Ti sublattices in the Ni-Ti matrix.

Table 6.7. Input parameters for Ni-Ti-Hf-Al system

Equilibrium Thermodynamic Calculations	
Temperature Range	973K-1273K
Temperature Step	50 K
Composition range for Ni, Ti, Hf and Al (atomic fraction)	0-1
Composition Step (atomic fraction)	0.01
Screening Coherent Second Phases	
Matrix Phase	NiTi (B2)
Minimum fraction of matrix phase	0.5
Composition range of Ni in matrix (atomic fraction)	0.49-0.51
Composition range of Ti in matrix (atomic fraction)	0.15-0.51
Composition range of Hf in matrix (atomic fraction)	0.01-0.3
Composition range of Al in matrix (atomic fraction)	0.01-0.1
Maximum allowed strain	5%
Maximum allowed matching area	100 Å^2

The set of second phases which are coherent with NiTi (B2) in the Ni-Ti-Hf-Al system are reported in Table 6.8. We found $Ni_2Ti(Hf, Al)$ to be coherent with NiTi matrix in Ni-Ti-Hf-Al system. Ni_2TiAl has been characterized experimentally and shown to reduce the transformation temperature in this alloy system [52].

Table 6.8. Predicted coherent second phases, denoted as SP in table, for NiTi (BCC_B2) matrix in Ni-Ti-Hf-Al system. Composition and temperature represent mean value of those within the stability region of specific SP and matrix. * is used for coherent second phases which have been observed in prior experimental studies.

SP	**SP Space Group**	**Matrix Plane**	**SP Plane**	**Matching Area (Å^2)**	$(\epsilon_{\mathbf{x}}^{\mathbf{2}} + \epsilon_{\mathbf{y}}^{\mathbf{2}})$	**Composition (at. fraction) [Al,Hf,Ni,Ti]**	**T (K)**
$^{*}Ni_2Ti - Hf$	$Fm\bar{3}m$	(111)	(111)	62.07	$4.96x10^{-4}$	[0.10,0.05, 0.50,0.35]	1198
$^{*}Ni_2Ti - Hf$	$Fm\bar{3}m$	(110)	(110)	50.68	$4.96x10^{-4}$	[0.10,0.05, 0.50,0.35]	1198
$^{*}Ni_2Ti - Hf$	$Fm\bar{3}m$	(100)	(100)	35.83	$4.96x10^{-4}$	[0.10,0.05, 0.50,0.35]	1198
$^{*}Ni_2Ti - Al$	$Fm\bar{3}m$	(111)	(111)	62.07	$5.52x10^{-3}$	[0.10,0.05, 0.50,0.35]	1198
$^{*}Ni_2Ti - Al$	$Fm\bar{3}m$	(110)	(110)	50.68	$5.52x10^{-3}$	[0.10,0.05, 0.50,0.35]	1198
$^{*}Ni_2Ti - Al$	$Fm\bar{3}m$	(100)	(100)	35.83	$5.52x10^{-3}$	[0.10,0.05, 0.50,0.35]	1198

6.4 Discussion and software availability

As with all physics-based simulations, the CohPhaseFind is not without approximations. It uses Thermo-Calc within TC-python framework to determine phase equilibria for multi-component systems using high-throughput single point thermodynamic equilibrium calculations. The accuracy of phase equilibria in multi-component systems is limited by the thermodynamic databases used. In order to screen the coherent second phases, we estimate the lattice parameters of phases using MP database. We note that our estimated lattice parameters are obtained at 0 K using DFT calculations and we are using lattice parameters of perfect stoichiometric phases (ignoring the effect of solubility on lattice parameters)

which will not be the case in the experimental studies. Thus, our study provides only rough estimates of coherency strain. We use strain-based lattice matching to determine coherent interfaces. Our approach uses only lattice parameters to find the coherent interfaces and the significance of atomic packing is not considered.

CohPhaseFind is an open source Python package and available to download at https://github.itap.purdue.edu/StrachanGroup/CohPhaseFind [171]. The code is organized in two parts. Users first execute phase_eq_par.py to perform thermodynamic calculations that calculate phase equilibria for specified inputs. The output of phase_eq_par.py is stored in a JSON dictionary which serves as an input for coherent.py which screens for coherent second phases among the phases which coexist with user specified matrix phase. Ternary/Pseudo ternary phase diagrams and multi-phase stability regions can be plotted using phase_diagrams.py. The workflow of CohPhaseFind is as follows:

1. Read and parse the input file. Phase_eq_par.py takes a single input file, typically with extension *ini*. Input parameters for thermodynamic calculations are:
   (a) components for multi-phase equilibria calculations
   (b) Minimum and maximum temperatures and compositions (Default compositions range from 0 to 1)
   (c) Temperature and compositions interval for grid evaluation
   (d) Thermo-Calc thermodynamic database
   (e) Any additional phases to consider
   (f) The path to directory to save output files
2. Based on parameters in input file, we generate inputs on a composition and temperature grid corresponding to single point equilibria calculations to be performed in Thermo-Calc via TC-python framework. These single point equilibria calculations are performed in parallel to reduce the time and final results of thermodynamic calculations are collated in a single JSON dictionary. This JSON dictionary contains the name of the stable phases, their corresponding phase fractions, compositions and sub-

lattices' details. Sublattices' details includes all the possible sublattices along with their respective compositions for each phase.

3. The output JSON dictionary now passes to interactive Python script coherent.py which screen for coherent second phases. The sequence of tasks performed in coherent.py are as follows:

   (a) Filter relevant compositions and temperatures from output JSON based on user specifications. The user specifies the total number of stable phases *(n)* and a common matrix phase. Other filters include the minimum fraction of matrix phase and the range of matrix phase compositions. This filtered JSON dictionary is now the input for the next step.

   (b) We now find stoichiometric formulae for all the second phases based on sublattices' details as described in section 6.2.2. Phase equilibria details along with stoichiometric formulae are stored in JSON dictionary. Temperatures and compositions for which stoichiometric formulae could not be found stored in separate JSON dictionary.

   (c) The stoichiometric formulae found are matched with MP according to decision tree shown in Figure 6.3 and the description in section 6.2.2, following which MP task-id is now added to the JSON dictionary. Again, temperatures and compositions for which MP match could not be found stored in separate JSON dictionary.

   (d) The MP lattice parameters of all the second phases and the matrix phase are passed to the substrate analyzer package within pymatgen to find the matching plane and in-plane matching superlattice vectors for each pair, see section 6.2.2. Miller indices for matching planes are currently restricted to be between 0 to 3. Results of this analysis is stored in CSV file, key outputs can be seen in Table 6.2, section 6.3.1. Further filter is applied to determine coherent second phase based on user specified maximum allowed strain and matching area, these results are stored in final CSV file.

As a convenience, isothermal ternary or pseudo ternary phase diagrams and phase boundaries can be plotted using interactive python script phase_diagrams.py. Our repository includes an example calculation for finding coherent second phases in Ni-Ti-Al system. The details for running the example calculation can be found at https://github.itap.purdue.edu/StrachanGroup/CohPhaseFind/blob/master/README.md.

6.5 Conclusions

We developed an automated approach to identify possible coherent precipitates within a base multi-component system of interest by coupling the equilibrium thermodynamic calculations with the strain-based lattice matching between base matrix and coherent second phases. We demonstrate our tool by exploring coherent second phases in NiTi shape memory alloys. We discover the already-explored Ni3Ti precipitate in the Ni-Ti system, Ti_2Cu precipitate in the Ni-Ti-Cu system, Ni_2TiAl precipitate in the Ni-Ti-Al system and $Ni_2Ti(Hf, Al)$ precipitate in the Ni-Ti-Hf-Al system. Additionally, we discover coherent Ti (BCC and HCP) precipitates in NiTi; Ni_3Ti precipitate in Ni-Ti-Al; Ti (BCC and HCP), Cu, Ni_3Ti, Cu_3Ti_2, and Cu_4Ti to be coherent with NiTi matrix in Ni-Ti-Cu system. These precipitates have not been explored and might lead to interesting thermo-mechanical properties. CohPhaseFind is generally applicable and can be useful to design engineered alloys with coherent second phases for a range of applications.

7. CONCLUSIONS

This thesis explores the effect of epitaxial strains via appropriate substrate or coherent second phase on the tunability of martensitic transformation in SMAs using atomistic simulations. In chapter 3, we characterize the energetics of martensitic transformation in low density Mg-Sc alloys from disordered BCC austenite to disordered orthorhombic martensite. The energy difference between the austenite and martensite phases is predicted to be 11±1 meV/atom, consistent with the experimental reported low martensitic transformation temperature. A local ordering analysis based model explaining the origin of stacking faults in HCP ordering of the martensite phase is developed. We also explore the avenues to increase the transformation and operation temperature of Mg-Sc alloys to room temperature. In the first approach, we utilize the epitaxial strains on the (110) closest pack plane, corresponding to growing a thin film on a substrate. A compressive strain of 6.8% along [100] and tensile strain of 5.8% along $[0\bar{1}1]$ on the (110) plane increase the energy difference between austenite and martensite to 16.9 meV/atom, which can be expected to result in an increase in transformation temperature to 278 K compared to 173 K in bulk. The superlattice between Mg and Mg-Sc is found to be another avenue to increase the transformation temperature. Simulations reveal that Mg acts as a martensite stabilizer and increases the zero-temperature energy difference to 18.1 meV/atom for 50 at.% Mg. Such an energy difference can be expected to increase the transformation temperature to room temperature. Thus, our DFT simulations show that the martensitic transformation temperature can be increased to room temperature by appropriate substrate or coherent second phase and provide design guidelines for room temperature lightweight SMAs. Chapter 4 proposes and demonstrates a novel approach to induce reversible martensitic transformation in superlattices formed by two non-transforming metals, pure Mg (HCP) and stoichiometric MgLi (BCC). Our approach is quite general and can be extended to other materials. MgLi/Mg superlattices are predicted to undergo a martensitic transformation crystallographically equivalent to MgSc alloys and can be expected to result in finite temperature shape memory behavior. The energy difference between the austenite and martensite can be tuned from 4.9 meV/atom to 18.1 meV/atom, and the estimated transformation temperature ranges from 94 K to 347 K for a fraction of

the pure Mg between 40% to 75%. In chapter 5, the role of coherent nanoscale precipitates on the temperature- and stress-induced martensitic transformation in nanocrystalline samples is characterized for the first time with an atomic resolution which provides an understanding of the underlying detailed physics behind experimentally observed novel properties. In particular, we studied the effect of nanoscale spherical $Ni_{50}Al_{50}$ precipitates on stress- and temperature-induced martensitic phase transformation in nanocrystalline $Ni_{63}Al_{37}$ SMAs using multi-million-atoms MD simulations. While single-phase nanocrystals of $Ni_{63}Al_{37}$ exhibits degradation of the reverse transformation during cyclic loading and, eventually, incomplete reversible transformation within a few cycles, the presence of precipitates stabilizes the stress-strain response. This is consistent with the experimental observation of ultra-low fatigue observed in N-Ti-Cu alloys due to the coherent Ti_2Cu precipitates. The presence of precipitates significantly improves the reversibility of the transformation by acting as elastic zones that partially shield the martensitic transformation and drive the reverse transformation. A detailed analysis of the MD trajectories reveals that the martensitic transformation of the matrix induces ultra-large elastic deformation in some of the B2 precipitates to the point of resulting in a martensite-like atomic structure. While the remnant martensite fraction originating from poor reversibility determines the remnant strain for single-phase nanocrystalline $Ni_{63}Al_{37}$, irreversible plastic slip (grain boundary sliding) dominates for systems with nanoscale precipitates. Our large-scale MD simulations provide guidelines to design low-fatigue ultra-fine grain SMAs. The presence of a coherent second phase is found to have a strong effect on martensitic transformation in all these studies, however, only a small number of the possible martensitic matrix/precipitate combinations have been explored. Therefore, in chapter 6, we developed an automated approach to discover possible coherent precipitates in a given base multi-component system of interest as well as the composition and processing conditions required to achieve the desired nanostructure. Our open source software package, CohPhaseFind, couples high-throughput equilibrium thermodynamics calculations with strain-based lattice matching. We demonstrate CohPhaseFind to discover possible coherent precipitates in Ni-Ti, Ni-Ti-X (X=Al, Cu, and Hf), and Ni-Ti-Hf-Al alloys. CohPhaseFind identifies the previously reported precipitates and new ones that merit exploration.

REFERENCES

[1] K. Bhattacharya *et al.*, *Microstructure of martensite: why it forms and how it gives rise to the shape-memory effect*. Oxford University Press, 2003, vol. 2.

[2] K. Bhattacharya, S. Conti, G. Zanzotto, and J. Zimmer, "Crystal symmetry and the reversibility of martensitic transformations," *Nature*, vol. 428, no. 6978, pp. 55–59, 2004.

[3] H. Sehitoglu, L. Patriarca, and Y. Wu, "Shape memory strains and temperatures in the extreme," *Current Opinion in Solid State and Materials Science*, vol. 21, no. 2, pp. 113–120, 2017.

[4] J. Witkowska, A. Sowińska, E. Czarnowska, T. Płociński, T. Borowski, and T. Wierzchoń, "Niti shape-memory alloy oxidized in low-temperature plasma with carbon coating: Characteristic and a potential for cardiovascular applications," *Applied Surface Science*, vol. 421, pp. 89–96, 2017.

[5] W.-S. Chang and Y. Araki, "Use of shape-memory alloys in construction: A critical review," in *Proceedings of the Institution of Civil Engineers-Civil Engineering*, Thomas Telford Ltd, vol. 169, 2016, pp. 87–95.

[6] H. Kahn, M. Huff, and A. Heuer, "The tini shape-memory alloy and its applications for mems," *Journal of Micromechanics and Microengineering*, vol. 8, no. 3, p. 213, 1998.

[7] N. Choudhary and D. Kaur, "Shape memory alloy thin films and heterostructures for mems applications: A review," *Sensors and Actuators A: Physical*, vol. 242, pp. 162–181, 2016.

[8] E. A. Williams, G. Shaw, and M. Elahinia, "Control of an automotive shape memory alloy mirror actuator," *Mechatronics*, vol. 20, no. 5, pp. 527–534, 2010.

[9] D. J. Hartl and D. C. Lagoudas, "Aerospace applications of shape memory alloys," *Proceedings of the Institution of Mechanical Engineers, Part G: Journal of Aerospace Engineering*, vol. 221, no. 4, pp. 535–552, 2007.

[10] T. Duerig, A. Pelton, and D. Stöckel, "An overview of nitinol medical applications," *Materials Science and Engineering: A*, vol. 273, pp. 149–160, 1999.

[11] S. Langbein and A. Czechowicz, "Introduction to shape memory alloy actuators," in *Shape Memory Alloy Valves*, Springer, 2015, pp. 41–72.

[12] *WIRED News*. [Online]. Available: https://www.wired.com/story/how-nasa-tests-shapeshifting-plane-wings/.

[13] *NASA MARS EXPLORATION PROGRAM*. [Online]. Available: https://mars.nasa.gov/resources/3904/artists-concept-of-rover-on-mars/.

[14] *Grand View Research*. [Online]. Available: https://www.grandviewresearch.com/industry-analysis/shape-memory-alloys-market.

[15] J. M. Jani, M. Leary, A. Subic, and M. A. Gibson, "A review of shape memory alloy research, applications and opportunities," *Materials & Design (1980-2015)*, vol. 56, pp. 1078–1113, 2014.

[16] C. Grossmann, J. Frenzel, V. Sampath, T. Depka, and G. Eggeler, "Elementary transformation and deformation processes and the cyclic stability of niti and niticu shape memory spring actuators," *Metallurgical and Materials Transactions A*, vol. 40, no. 11, pp. 2530–2544, 2009.

[17] T. W. Duerig, K. Melton, and D. Stöckel, *Engineering aspects of shape memory alloys*. Butterworth-heinemann, 2013.

[18] Y. Ogawa, D. Ando, Y. Sutou, H. Somekawa, and J. Koike, "Martensitic transformation in a β-type mg–sc alloy," *Shape Memory and Superelasticity*, vol. 4, no. 1, pp. 167–173, 2018.

[19] R. Kainuma, H. Ohtani, and K. Ishida, "Effect of alloying elements on martensitic transformation in the binary nial (β) phase alloys," *Metallurgical and materials transactions A*, vol. 27, no. 9, pp. 2445–2453, 1996.

[20] Y. Liu, I. Houver, H. Xiang, L. Bataillard, and S. Miyazaki, "Strain dependence of pseudoelastic hysteresis of niti," *Metallurgical and materials transactions A*, vol. 30, no. 5, pp. 1275–1282, 1999.

[21] H. Y. Kim, S. Hashimoto, J. I. Kim, H. Hosoda, and S. Miyazaki, "Mechanical properties and shape memory behavior of ti-nb alloys," *materials Transactions*, vol. 45, no. 7, pp. 2443–2448, 2004.

[22] N. Ono, A. Tsukahara, R. Kainuma, and K. Ishida, "The properties of two-phase ni–al–fe shape memory alloys in the virgin and shape-memory-cycled states," *Materials Science and Engineering: A*, vol. 273, pp. 420–424, 1999.

[23] T. Omori, K. Ando, M. Okano, *et al.*, "Superelastic effect in polycrystalline ferrous alloys," *Science*, vol. 333, no. 6038, pp. 68–71, 2011.

[24] Y. Sutou, R. Kainuma, and K. Ishida, "Effect of alloying elements on the shape memory properties of ductile cu–al–mn alloys," *Materials Science and Engineering: A*, vol. 273, pp. 375–379, 1999.

[25] A. Ölander, "An electrochemical investigation of solid cadmium-gold alloys," *Journal of the American Chemical Society*, vol. 54, no. 10, pp. 3819–3833, 1932.

[26] W. J. Buehler, J. V. Gilfrich, and R. Wiley, "Effect of low-temperature phase changes on the mechanical properties of alloys near composition tini," *Journal of applied physics*, vol. 34, no. 5, pp. 1475–1477, 1963.

[27] F. E. Wang, W. J. Buehler, and S. J. Pickart, "Crystal structure and a unique"martensitic"transition of tini," *Journal of Applied Physics*, vol. 36, no. 10, pp. 3232–3239, 1965.

[28] M. I. Khan, A. Pequegnat, and Y. N. Zhou, "Multiple memory shape memory alloys," *Advanced Engineering Materials*, vol. 15, no. 5, pp. 386–393, 2013.

[29] K. Otsuka and X. Ren, "Physical metallurgy of ti–ni-based shape memory alloys," *Progress in materials science*, vol. 50, no. 5, pp. 511–678, 2005.

[30] X. Ren, N. Miura, J. Zhang, *et al.*, "A comparative study of elastic constants of ti–ni-based alloys prior to martensitic transformation," *Materials Science and Engineering: A*, vol. 312, no. 1-2, pp. 196–206, 2001.

[31] M. Zarinejad and Y. Liu, "Dependence of transformation temperatures of niti-based shape-memory alloys on the number and concentration of valence electrons," *Advanced Functional Materials*, vol. 18, no. 18, pp. 2789–2794, 2008.

[32] M. Zarinejad and Y. Liu, *Dependence of transformation temperatures of shape memory alloys on the number and concentration of valence electrons*, 2010.

[33] W. Tang, B. Sundman, R. Sandström, and C. Qiu, "New modelling of the b2 phase and its associated martensitic transformation in the ti–ni system," *Acta materialia*, vol. 47, no. 12, pp. 3457–3468, 1999.

[34] J. Frenzel, E. P. George, A. Dlouhy, C. Somsen, M.-X. Wagner, and G. Eggeler, "Influence of ni on martensitic phase transformations in niti shape memory alloys," *Acta Materialia*, vol. 58, no. 9, pp. 3444–3458, 2010.

[35] D. Mutter and P. Nielaba, "Simulation of structural phase transitions in niti," *Physical Review B*, vol. 82, no. 22, p. 224 201, 2010.

[36] X. Huang, G. J. Ackland, and K. M. Rabe, "Crystal structures and shape-memory behaviour of niti," *Nature materials*, vol. 2, no. 5, pp. 307–311, 2003.

[37] K. G. Vishnu and A. Strachan, "Phase stability and transformations in niti from density functional theory calculations," *Acta materialia*, vol. 58, no. 3, pp. 745–752, 2010.

[38] J. Frenzel, A. Wieczorek, I. Opahle, B. Maaß, R. Drautz, and G. Eggeler, "On the effect of alloy composition on martensite start temperatures and latent heats in ni–ti-based shape memory alloys," *Acta Materialia*, vol. 90, pp. 213–231, 2015.

[39] J. M. Ball and R. D. James, "Proposed experimental tests of a theory of fine microstructure and the two-well problem," *Philosophical Transactions of the Royal Society of London. Series A: Physical and Engineering Sciences*, vol. 338, no. 1650, pp. 389–450, 1992.

[40] J. Cui, Y. S. Chu, O. O. Famodu, *et al.*, "Combinatorial search of thermoelastic shape-memory alloys with extremely small hysteresis width," *Nature materials*, vol. 5, no. 4, pp. 286–290, 2006.

[41] D. Xue, P. V. Balachandran, J. Hogden, J. Theiler, D. Xue, and T. Lookman, "Accelerated search for materials with targeted properties by adaptive design," *Nature communications*, vol. 7, no. 1, pp. 1–9, 2016.

[42] S. Zhu, X. Yang, F. Hu, S. Deng, and Z. Cui, "Processing of porous tini shape memory alloy from elemental powders by ar-sintering," *Materials Letters*, vol. 58, no. 19, pp. 2369–2373, 2004.

[43] D. Li, X. Zhang, Z. Xiong, and Y.-W. Mai, "Lightweight niti shape memory alloy based composites with high damping capacity and high strength," *Journal of Alloys and Compounds*, vol. 490, no. 1-2, pp. L15–L19, 2010.

[44] D. Ping, Y. Mitarai, and F. Yin, "Microstructure and shape memory behavior of a ti–30nb–3pd alloy," *Scripta materialia*, vol. 52, no. 12, pp. 1287–1291, 2005.

[45] J. L. Pak, C. Lei, and C. Wayman, "Atomic ordering in ti v al shape memory alloys," *Materials Science and Engineering: A*, vol. 132, pp. 237–244, 1991.

[46] Y. Ogawa, D. Ando, Y. Sutou, and J. Koike, "A lightweight shape-memory magnesium alloy," *Science*, vol. 353, no. 6297, pp. 368–370, 2016.

[47] W. Zhao, E. Guo, K. Zhang, X. Tian, and C. Tan, "Martensite phase structure of mg-sc lightweight shape memory alloy and the effect of rare earth elements doping," *Scripta Materialia*, vol. 199, p. 113 863, 2021.

[48] S. T. Reeve, "Materials design with molecular dynamics: Novel properties in martensitic alloys through free energy landscape engineering," Ph.D. dissertation, Purdue University, 2018.

[49] R. R. Adharapurapu, F. Jiang, and K. S. Vecchio, "Aging effects on hardness and dynamic compressive behavior of ti–55ni (at.%) alloy," *Materials Science and Engineering: A*, vol. 527, no. 7-8, pp. 1665–1676, 2010.

[50] X. Meng, W. Cai, F. Chen, and L. Zhao, "Effect of aging on martensitic transformation and microstructure in ni-rich tinihf shape memory alloy," *Scripta materialia*, vol. 54, no. 9, pp. 1599–1604, 2006.

[51] Y. Koizumi, Y. Ro, S. Nakazawa, and H. Harada, "Niti-base intermetallic alloys strengthened by al substitution," *Materials Science and Engineering: A*, vol. 223, no. 1-2, pp. 36–41, 1997.

[52] J. Jung, G. Ghosh, and G. Olson, "A comparative study of precipitation behavior of heusler phase (ni2tial) from b2-tini in ni–ti–al and ni–ti–al–x (x= hf, pd, pt, zr) alloys," *Acta Materialia*, vol. 51, no. 20, pp. 6341–6357, 2003.

[53] D. H. Dai Hsu, "Design and development of niti-based precipitation-strengthened high-temperature shape memory alloys for actuator applications," Ph.D. dissertation, University of Florida, 2013.

[54] D. H. Dai Hsu, B. C. Hornbuckle, B. Valderrama, *et al.*, "The effect of aluminum additions on the thermal, microstructural, and mechanical behavior of nitihf shape memory alloys," *Journal of Alloys and Compounds*, vol. 638, pp. 67–76, 2015.

[55] H. Wang, Y. Hao, S. He, *et al.*, "Elastically confined martensitic transformation at the nano-scale in a multifunctional titanium alloy," *Acta Materialia*, vol. 135, pp. 330–339, 2017.

[56] C. Chluba, W. Ge, R. L. de Miranda, *et al.*, "Ultralow-fatigue shape memory alloy films," *Science*, vol. 348, no. 6238, pp. 1004–1007, 2015.

[57] H. Chen, Y.-D. Wang, Z. Nie, *et al.*, "Unprecedented non-hysteretic superelasticity of [001]-oriented nicofega single crystals," *Nature materials*, vol. 19, no. 7, pp. 712–718, 2020.

[58] P. Hua, M. Xia, Y. Onuki, and Q. Sun, "Nanocomposite niti shape memory alloy with high strength and fatigue resistance," *Nature Nanotechnology*, vol. 16, no. 4, pp. 409–413, 2021.

[59] K. Guda Vishnu and A. Strachan, "Shape memory metamaterials with tunable thermomechanical response via hetero-epitaxial integration: A molecular dynamics study," *Journal of Applied Physics*, vol. 113, no. 10, p. 103 503, 2013.

[60] S. T. Reeve, K. G. Vishnu, A. Belessiotis-Richards, and A. Strachan, "Tunability of martensitic behavior through coherent nanoprecipitates and other nanostructures," *Acta Materialia*, vol. 154, pp. 295–302, 2018.

[61] S. Desai, S. T. Reeve, K. G. Vishnu, and A. Strachan, "Tuning martensitic transformations via coherent second phases in nanolaminates using free energy landscape engineering," *Journal of Applied Physics*, vol. 127, no. 12, p. 125 112, 2020.

[62] S. T. Reeve, A. Belessiotis-Richards, and A. Strachan, "Harnessing mechanical instabilities at the nanoscale to achieve ultra-low stiffness metals," *Nature communications*, vol. 8, no. 1, pp. 1–7, 2017.

[63] S. T. Reeve, K. G. Vishnu, and A. Strachan, "Uncharacteristic second order martensitic transformation in metals via epitaxial stress fields," *Journal of Applied Physics*, vol. 127, no. 4, p. 045 107, 2020.

[64] J. Zhu, H.-H. Wu, X.-S. Yang, *et al.*, "Dissecting the influence of nanoscale concentration modulation on martensitic transformation in multifunctional alloys," *Acta Materialia*, vol. 181, pp. 99–109, 2019.

[65] J. Zhu, H.-H. Wu, Y. Wu, *et al.*, "Influence of ni4ti3 precipitation on martensitic transformations in niti shape memory alloy: R phase transformation," *Acta Materialia*, vol. 207, p. 116 665, 2021.

[66] T. Yu, Y. Gao, L. Casalena, P. Anderson, M. Mills, and Y. Wang, "H-phase precipitation and its effects on martensitic transformation in niti-hf high-temperature shape memory alloys," *Acta Materialia*, vol. 208, p. 116 651, 2021.

[67] J. Allison, D. Backman, and L. Christodoulou, "Integrated computational materials engineering: A new paradigm for the global materials profession," *Jom*, vol. 58, no. 11, pp. 25–27, 2006.

[68] E. Schrödinger, "An undulatory theory of the mechanics of atoms and molecules," *Physical review*, vol. 28, no. 6, p. 1049, 1926.

[69] M. Born and R. Oppenheimer, "Zur quantentheorie der molekeln," *Annalen der physik*, vol. 389, no. 20, pp. 457–484, 1927.

[70] M. L. Cohen and S. G. Louie, *Fundamentals of condensed matter physics*. Cambridge University Press, 2016.

[71] P. Hohenberg and W. Kohn, "Physical review, 136," *B864*, 1964.

[72] W. Kohn and L. J. Sham, "Self-consistent equations including exchange and correlation effects," *Physical review*, vol. 140, no. 4A, A1133, 1965.

[73] A. E. Mattsson, P. A. Schultz, M. P. Desjarlais, T. R. Mattsson, and K. Leung, "Designing meaningful density functional theory calculations in materials science—a primer," *Modelling and Simulation in Materials Science and Engineering*, vol. 13, no. 1, R1, 2004.

[74] R. O. Jones and O. Gunnarsson, "The density functional formalism, its applications and prospects," *Reviews of Modern Physics*, vol. 61, no. 3, p. 689, 1989.

[75] J. P. Perdew, K. Burke, and M. Ernzerhof, "Generalized gradient approximation made simple," *Physical review letters*, vol. 77, no. 18, p. 3865, 1996.

[76] J. E. Lennard-Jones, "Cohesion," *Proceedings of the Physical Society (1926-1948)*, vol. 43, no. 5, p. 461, 1931.

[77] P. M. Morse and E. C. G. Stueckelberg, "Diatomic molecules according to the wave mechanics i: Electronic levels of the hydrogen molecular ion," *Physical Review*, vol. 33, no. 6, p. 932, 1929.

[78] G. Purja Pun and Y. Mishin, "Development of an interatomic potential for the ni-al system," *Philosophical Magazine*, vol. 89, no. 34-36, pp. 3245–3267, 2009.

[79] F. H. Stillinger and T. A. Weber, "Computer simulation of local order in condensed phases of silicon," *Physical review B*, vol. 31, no. 8, p. 5262, 1985.

[80] S. Tripathi, K. G. Vishnu, M. S. Titus, and A. Strachan, "Tunability of martensitic transformation in mg-sc shape memory alloys: A dft study," *Acta Materialia*, vol. 189, pp. 1–9, 2020.

[81] A. R. Natarajan and A. Van der Ven, "First-principles investigation of phase stability in the mg-sc binary alloy," *Physical Review B*, vol. 95, no. 21, p. 214 107, 2017.

[82] K. J. Choi, M. Biegalski, Y. Li, *et al.*, "Enhancement of ferroelectricity in strained batio3 thin films," *Science*, vol. 306, no. 5698, pp. 1005–1009, 2004.

[83] L. Zhang, J. Chen, L. Fan, *et al.*, "Giant polarization in super-tetragonal thin films through interphase strain," *Science*, vol. 361, no. 6401, pp. 494–497, 2018.

[84] G. Kresse and J. Hafner, "Ab initio molecular dynamics for liquid metals," *Physical review B*, vol. 47, no. 1, p. 558, 1993.

[85] G. Kresse and J. Hafner, "Ab initio molecular-dynamics simulation of the liquid-metal–amorphous-semiconductor transition in germanium," *Physical Review B*, vol. 49, no. 20, p. 14 251, 1994.

[86] G. Kresse and J. Furthmüller, "Efficiency of ab-initio total energy calculations for metals and semiconductors using a plane-wave basis set," *Computational materials science*, vol. 6, no. 1, pp. 15–50, 1996.

[87] G. Kresse and J. Furthmüller, "Efficient iterative schemes for ab initio total-energy calculations using a plane-wave basis set," *Physical review B*, vol. 54, no. 16, p. 11 169, 1996.

[88] P. E. Blöchl, "Projector augmented-wave method," *Physical review B*, vol. 50, no. 24, p. 17 953, 1994.

[89] G. Kresse and D. Joubert, "From ultrasoft pseudopotentials to the projector augmented-wave method," *Physical review b*, vol. 59, no. 3, p. 1758, 1999.

[90] A. Zunger, S.-H. Wei, L. Ferreira, and J. E. Bernard, "Special quasirandom structures," *Physical review letters*, vol. 65, no. 3, p. 353, 1990.

[91] A. Van de Walle, P. Tiwary, M. De Jong, *et al.*, "Efficient stochastic generation of special quasirandom structures," *Calphad*, vol. 42, pp. 13–18, 2013.

[92] A. Van De Walle, M. Asta, and G. Ceder, "The alloy theoretic automated toolkit: A user guide," *Calphad*, vol. 26, no. 4, pp. 539–553, 2002.

[93] A. A. Maradudin, E. W. Montroll, G. H. Weiss, and I. Ipatova, *Theory of lattice dynamics in the harmonic approximation*. Academic press New York, 1963, vol. 3.

[94] A. Otero-de-la-Roza, D. Abbasi-Pérez, and V. Luaña, "Gibbs2: A new version of the quasiharmonic model code. ii. models for solid-state thermodynamics, features and implementation," *Computer Physics Communications*, vol. 182, no. 10, pp. 2232–2248, 2011.

[95] S. Barman, A. Chakrabarti, S. Singh, *et al.*, "Theoretical prediction and experimental study of a ferromagnetic shape memory alloy: Ga 2 mnni," *Physical Review B*, vol. 78, no. 13, p. 134 406, 2008.

[96] T. Roy and A. Chakrabarti, "Possibility of martensite transition in pt–y–ga (y= cr, mn, and fe) system: An ab-initio calculation of the bulk mechanical, electronic and magnetic properties," *Journal of Magnetism and Magnetic Materials*, vol. 401, pp. 929–937, 2016.

[97] Y. Wang, X. Yang, Y. Xue, and Y. Chen, "Exploration of magnetic shape memory alloys in ga2mo x (x= cr, mn, fe, co, and ni) systems: A first-principles study," *Journal of Applied Physics*, vol. 124, no. 8, p. 085 112, 2018.

[98] J. Chen, Y. Li, J. Shang, and H. Xu, "First principles calculations on martensitic transformation and phase instability of ni–mn–ga high temperature shape memory alloys," *Applied physics letters*, vol. 89, no. 23, p. 231 921, 2006.

[99] Y. Ye, C. T. Chan, and K. M. Ho, "Structural and electronic properties of the martensitic alloys tini, tipd, and tipt," *Physical Review B*, vol. 56, no. 7, p. 3678, 1997.

[100] T. Chakraborty, J. Rogal, and R. Drautz, "Unraveling the composition dependence of the martensitic transformation temperature: A first-principles study of ti-ta alloys," *Physical Review B*, vol. 94, no. 22, p. 224 104, 2016.

[101] E. Fisher and C. Renken, "Single-crystal elastic moduli and the hcp→ bcc transformation in ti, zr, and hf," *Physical review*, vol. 135, no. 2A, A482, 1964.

[102] *Materials Project Database*. [Online]. Available: https://materialsproject.org/.

[103] M. de Jong, L. Qi, D. L. Olmsted, A. van de Walle, and M. Asta, "Calculations of planar defect energies in substitutional alloys using the special-quasirandom-structure approach," *Physical Review B*, vol. 93, no. 9, p. 094 101, 2016.

[104] D. Sheppard, P. Xiao, W. Chemelewski, D. D. Johnson, and G. Henkelman, "A generalized solid-state nudged elastic band method," *The Journal of chemical physics*, vol. 136, no. 7, p. 074 103, 2012.

[105] T. Chakraborty, J. Rogal, and R. Drautz, "Martensitic transformation between competing phases in ti–ta alloys: A solid-state nudged elastic band study," *Journal of Physics: Condensed Matter*, vol. 27, no. 11, p. 115 401, 2015.

[106] S. Kibey, H. Sehitoglu, and D. Johnson, "Energy landscape for martensitic phase transformation in shape memory niti," *Acta Materialia*, vol. 57, no. 5, pp. 1624–1629, 2009.

[107] L. Freund and W. D. Nix, "A critical thickness condition for a strained compliant substrate/epitaxial film system," *Applied Physics Letters*, vol. 69, no. 2, pp. 173–175, 1996.

[108] J. Buschbeck, I. Opahle, M. Richter, *et al.*, "Full tunability of strain along the fcc-bcc bain path in epitaxial films and consequences for magnetic properties," *Physical review letters*, vol. 103, no. 21, p. 216 101, 2009.

[109] Y. Ogawa, Y. Sutou, D. Ando, and J. Koike, "Aging precipitation kinetics of mg-sc alloy with bcc+ hcp two-phase," *Journal of Alloys and Compounds*, vol. 747, pp. 854–860, 2018.

[110] S. Tripathi, M. S. Titus, and A. Strachan, "Martensitic transformation in superlattices of two non-transforming metals," *Journal of Applied Physics*, vol. 130, no. 16, p. 165 105, 2021.

[111] C.-x. Zhang, P.-l. Chen, H.-j. Chen, A.-j. SHI, and S.-k. GUANG, "Application and research progress of magnesium alloys in automobile industry," *Foundry Technology*, vol. 29, no. 4, p. 531, 2008.

[112] H. Furuya, N. Kogiso, S. Matunaga, and K. Senda, "Applications of magnesium alloys for aerospace structure systems," in *Materials science forum*, Trans Tech Publ, vol. 350, 2000, pp. 341–348.

[113] J. Deetz, "The use of wrought magnesium in bicycles," *JOM*, vol. 57, no. 5, pp. 50–53, 2005.

[114] H. Nabae, M. Hemmi, Y. Hirota, T. Ide, K. Suzumori, and G. Endo, "Super-low friction and lightweight hydraulic cylinder using multi-directional forging magnesium alloy and its application to robotic leg," *Advanced Robotics*, vol. 32, no. 9, pp. 524–534, 2018.

[115] G. K. Schwalfenberg and S. J. Genuis, "The importance of magnesium in clinical healthcare," *Scientifica*, vol. 2017, 2017.

[116] W. Xu, N. Birbilis, G. Sha, *et al.*, "A high-specific-strength and corrosion-resistant magnesium alloy," *Nature materials*, vol. 14, no. 12, pp. 1229–1235, 2015.

[117] G. S. Frankel, "Ready for the road," *Nature materials*, vol. 14, no. 12, pp. 1189–1190, 2015.

[118] B. Ham and X. Zhang, "High strength mg/nb nanolayer composites," *Materials Science and Engineering: A*, vol. 528, no. 4-5, pp. 2028–2033, 2011.

[119] S. Pathak, N. Velisavljevic, J. K. Baldwin, *et al.*, "Strong, ductile, and thermally stable bcc-mg nanolaminates," *Scientific reports*, vol. 7, no. 1, pp. 1–9, 2017.

[120] R.-z. Wu, Y.-d. Yan, G.-x. Wang, *et al.*, "Recent progress in magnesium–lithium alloys," *International Materials Reviews*, vol. 60, no. 2, pp. 65–100, 2015.

[121] G. Thompson, R. Banerjee, S. Dregia, and H. Fraser, "Phase stability of bcc zr in nb/zr thin film multilayers," *Acta materialia*, vol. 51, no. 18, pp. 5285–5294, 2003.

[122] P. Jacques, "Transformation-induced plasticity for high strength formable steels," *Current Opinion in Solid State and Materials Science*, vol. 8, no. 3-4, pp. 259–265, 2004.

[123] R. Zarnetta, R. Takahashi, M. L. Young, *et al.*, "Identification of quaternary shape memory alloys with near-zero thermal hysteresis and unprecedented functional stability," *Advanced Functional Materials*, vol. 20, no. 12, pp. 1917–1923, 2010.

[124] N. A. Zarkevich and D. D. Johnson, "Reliable thermodynamic estimators for screening caloric materials," *Journal of Alloys and Compounds*, vol. 802, pp. 712–722, 2019.

[125] N. A. Zarkevich and D. D. Johnson, "Stable atomic structure of niti austenite," *Physical Review B*, vol. 90, no. 6, p. 060 102, 2014.

[126] Z. Hou, J. Zhang, J. Li, *et al.*, "Phase transformation-induced strength softening in ti/ta nanostructured multilayers: Coherent interface vs phase boundary," *Materials Science and Engineering: A*, vol. 684, pp. 78–83, 2017.

[127] R. Salloom, D. Reith, R. Banerjee, and S. Srinivasan, "First principles calculations on the effect of interstitial oxygen on phase stability and β–α martensitic transformation in ti–nb alloys," *Journal of Materials Science*, vol. 53, no. 16, pp. 11 473–11 487, 2018.

[128] Z. Shi, M. Liu, D. Naik, and J. L. Gole, "Electrochemical properties of li–mg alloy electrodes for lithium batteries," *Journal of Power Sources*, vol. 92, no. 1-2, pp. 70–80, 2001.

[129] S. Tripathi, K. G. Vishnu, M. S. Titus, and A. Strachan, "Uncovering the role of nanoscale precipitates on martensitic transformation and superelasticity," *Acta Materialia* (under review),

[130] J. San Juan, M. L. Nó, and C. A. Schuh, "Nanoscale shape-memory alloys for ultrahigh mechanical damping," *Nature nanotechnology*, vol. 4, no. 7, pp. 415–419, 2009.

[131] L. Manosa, A. Planes, E. Vives, E. Bonnot, and R. Romero, "The use of shape-memory alloys for mechanical refrigeration," *Functional Materials Letters*, vol. 2, no. 02, pp. 73–78, 2009.

[132] P. B. Leal and M. A. Savi, "Shape memory alloy-based mechanism for aeronautical application: Theory, optimization and experiment," *Aerospace Science and Technology*, vol. 76, pp. 155–163, 2018.

[133] T. Umale, D. Salas, B. Tomes, R. Arroyave, and I. Karaman, "The effects of wide range of compositional changes on the martensitic transformation characteristics of nitihf shape memory alloys," *Scripta Materialia*, vol. 161, pp. 78–83, 2019.

[134] K. R. Morrison, M. J. Cherukara, H. Kim, and A. Strachan, "Role of grain size on the martensitic transformation and ultra-fast superelasticity in shape memory alloys," *Acta Materialia*, vol. 95, pp. 37–43, 2015.

[135] W.-S. Ko, S. B. Maisel, B. Grabowski, J. B. Jeon, and J. Neugebauer, "Atomic scale processes of phase transformations in nanocrystalline niti shape-memory alloys," *Acta Materialia*, vol. 123, pp. 90–101, 2017.

[136] D. Farkas, B. Mutasa, C. Vailhe, and K. Ternes, "Interatomic potentials for b2 nial and martensitic phases," *Modelling and Simulation in Materials Science and Engineering*, vol. 3, no. 2, p. 201, 1995.

[137] K. R. Morrison, M. J. Cherukara, K. G. Vishnu, and A. Strachan, "Role of atomic variability and mechanical constraints on the martensitic phase transformation of a model disordered shape memory alloy via molecular dynamics," *Acta materialia*, vol. 69, pp. 30–36, 2014.

[138] S. Plimpton, "Fast parallel algorithms for short-range molecular dynamics," *Journal of computational physics*, vol. 117, no. 1, pp. 1–19, 1995.

[139] P. Hirel, "Atomsk: A tool for manipulating and converting atomic data files," *Computer Physics Communications*, vol. 197, pp. 212–219, 2015.

[140] G. Voronoi, "Nouvelles applications des paramètres continus à la théorie des formes quadratiques. deuxième mémoire. recherches sur les parallélloèdres primitifs.," *Journal für die reine und angewandte Mathematik (Crelles Journal)*, vol. 1908, no. 134, pp. 198–287, 1908.

[141] P. M. Larsen, S. Schmidt, and J. Schiøtz, "Robust structural identification via polyhedral template matching," *Modelling and Simulation in Materials Science and Engineering*, vol. 24, no. 5, p. 055 007, 2016.

[142] A. Stukowski, "Visualization and analysis of atomistic simulation data with ovito–the open visualization tool," *Modelling and Simulation in Materials Science and Engineering*, vol. 18, no. 1, p. 015 012, 2009.

[143] H. Kim and A. Strachan, "Mechanical response of nanocrystalline platinum via molecular dynamics: Size effects in bulk versus thin-film samples," *Modelling and Simulation in Materials Science and Engineering*, vol. 23, no. 6, p. 065 012, 2015.

[144] K. Gall and H. Maier, "Cyclic deformation mechanisms in precipitated niti shape memory alloys," *Acta Materialia*, vol. 50, no. 18, pp. 4643–4657, 2002.

[145] S. Tripathi, L. C. Fan, M. S. Titus, and A. Strachan, "Automated approach to discover coherent precipitates in multi-component shape memory alloys," *Computational Materials Science*, vol. 197, p. 110 651, 2021.

[146] *1903 Wright Engine*. [Online]. Available: http://wright-brothers.org/Information_Desk/Just_the_Facts/Engines_&_Props/1903_Engine.htm.

[147] M. W. McFarland and A. G. Renstrom, "The papers of wilbur and orville wright," *Quarterly Journal of Current Acquisitions*, vol. 7, no. 4, pp. 22–34, 1950.

[148] L. S. Hobbs, *The Wright brothers' engines and their design*. Good Press, 2019.

[149] H. H. Lippincott, "Propulsion systems of the wright brothers," *The Wright Flyer-An Engineeering Perspective*, 1987.

[150] M. Perrut, P. Caron, M. Thomas, and A. Couret, "High temperature materials for aerospace applications: Ni-based superalloys and γ-tial alloys," *Comptes Rendus Physique*, vol. 19, no. 8, pp. 657–671, 2018.

[151] A. Wilm, "Drp 244554 (german patent) 1906," *Metallurgie*, vol. 8, p. 223, 1911.

[152] E. Hornbogen, "Hundred years of precipitation hardening," *Journal of light metals*, vol. 1, no. 2, pp. 127–132, 2001.

[153] Q. Wang, Z. Li, S. Pang, X. Li, C. Dong, and P. K. Liaw, "Coherent precipitation and strengthening in compositionally complex alloys: A review," *Entropy*, vol. 20, no. 11, p. 878, 2018.

[154] A. Musfirah and A. Jaharah, "Magnesium and aluminum alloys in automotive industry," *Journal of Applied Sciences Research*, vol. 8, no. 9, pp. 4865–4875, 2012.

[155] J. C. Williams and E. A. Starke Jr, "Progress in structural materials for aerospace systems," *Acta materialia*, vol. 51, no. 19, pp. 5775–5799, 2003.

[156] Y.-t. Wu, C. Li, Y.-f. Li, J. Wu, X.-c. Xia, and Y.-c. Liu, "Effects of heat treatment on the microstructure and mechanical properties of ni 3 al-based superalloys: A review," *International Journal of Minerals, Metallurgy and Materials*, vol. 28, no. 4, pp. 553–566, 2021.

[157] R. Eriş, M. V. Akdeniz, and A. O. Mekhrabov, "Atomic size effect of alloying elements on the formation, evolution and strengthening of γ -ni3al precipitates in ni-based superalloys," *Intermetallics*, vol. 109, pp. 37–47, 2019.

[158] A. van de Walle and M. Asta, "High-throughput calculations in the context of alloy design," *MRS Bulletin*, vol. 44, no. 4, pp. 252–256, 2019.

[159] O. Senkov, J. Miller, D. Miracle, and C. Woodward, "Accelerated exploration of multi-principal element alloys for structural applications," *Calphad*, vol. 50, pp. 32–48, 2015.

[160] G. Hautier, C. C. Fischer, A. Jain, T. Mueller, and G. Ceder, "Finding nature's missing ternary oxide compounds using machine learning and density functional theory," *Chemistry of Materials*, vol. 22, no. 12, pp. 3762–3767, 2010.

[161] K. Mathew, A. K. Singh, J. J. Gabriel, *et al.*, "Mpinterfaces: A materials project based python tool for high-throughput computational screening of interfacial systems," *Computational Materials Science*, vol. 122, pp. 183–190, 2016.

[162] Z. D. McClure and A. Strachan, "Expanding materials selection via transfer learning for high-temperature oxide selection," *JOM*, vol. 73, no. 1, pp. 103–115, 2021.

[163] J.-O. Andersson, T. Helander, L. Höglund, P. Shi, and B. Sundman, "Thermo-calc & dictra, computational tools for materials science," *Calphad*, vol. 26, no. 2, pp. 273–312, 2002.

[164] M. Hillert, *Phase equilibria, phase diagrams and phase transformations: their thermodynamic basis*. Cambridge university press, 2007.

[165] *Thermo-Calc software TCNI Superalloys/NI-alloys database version 8*. [Online]. Available: https://thermocalc.com/products/databases/nickel-based-alloys/.

[166] *AFLOW Database*. [Online]. Available: http://aflowlib.org/.

[167] A. Zur and T. McGill, "Lattice match: An application to heteroepitaxy," *Journal of applied physics*, vol. 55, no. 2, pp. 378–386, 1984.

[168] S. Saghaian, H. Karaca, H. Tobe, *et al.*, "High strength nitihf shape memory alloys with tailorable properties," *Acta Materialia*, vol. 134, pp. 211–220, 2017.

[169] F. Yang, D. Coughlin, P. J. Phillips, *et al.*, "Structure analysis of a precipitate phase in an ni-rich high-temperature nitihf shape memory alloy," *Acta Materialia*, vol. 61, no. 9, pp. 3335–3346, 2013.

[170] S. Jiang, Y. Zhang, L. Zhao, and Y. Zheng, "Influence of annealing on niti shape memory alloy subjected to severe plastic deformation," *Intermetallics*, vol. 32, pp. 344–351, 2013.

[171] Shivam Tripathi, Lok C. Fan, Michael S. Titus, and Alejandro Strachan, *CohPhaseFind*, Oct. 15, 2021. [Online]. Available: https://github.itap.purdue.edu/StrachanGroup/CohPhaseFind.

A. SUPPLEMENTARY FIGURES AND TABLES

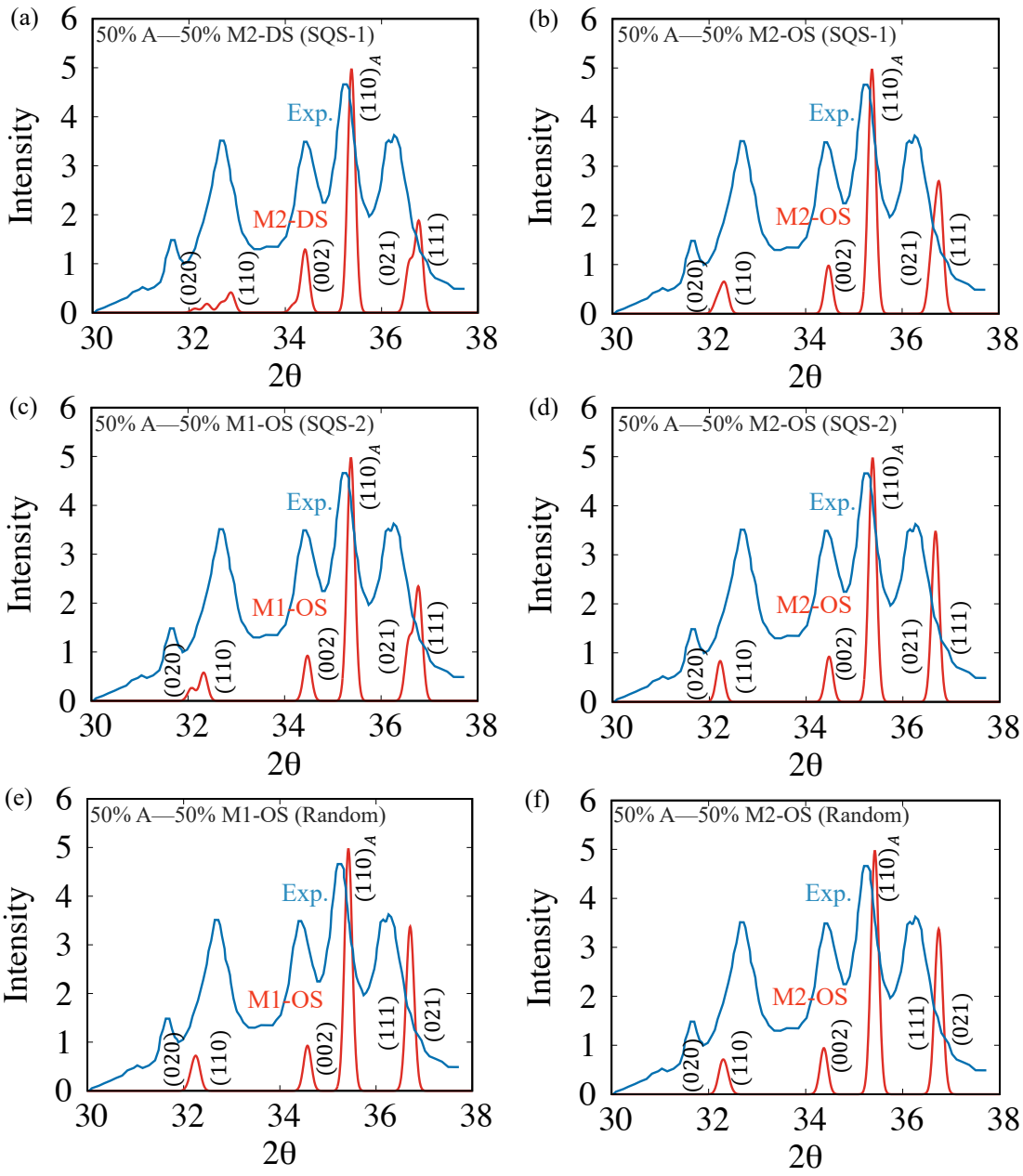

Figure A.1. XRD pattern for system with 50% A and (a) 50% M2-DS (SQS-1), (b) 50% M2-OS (SQS-1), (c) M1-OS (SQS-2), (d) M2-OS (SQS-2), (e) M1-OS (Random) and (f) M2-OS (Random) phases, where gaussian distribution with standard deviation of 0.08 is used for peak broadening. Blue curve shows XRD pattern from experiments [18] at -190 °C

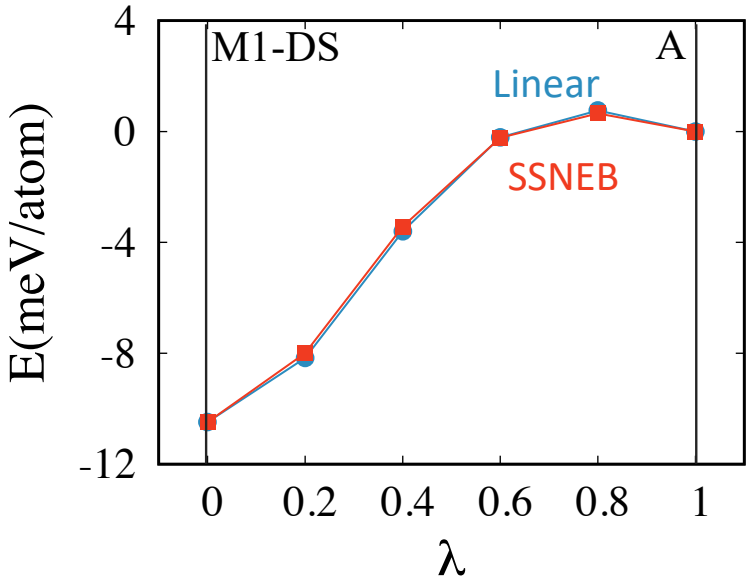

Figure A.2. Transformation pathway between A to M1-DS for SQS-1 using generalized solid state nudged elastic band (G-SSNEB) [104] and linear extrapolation

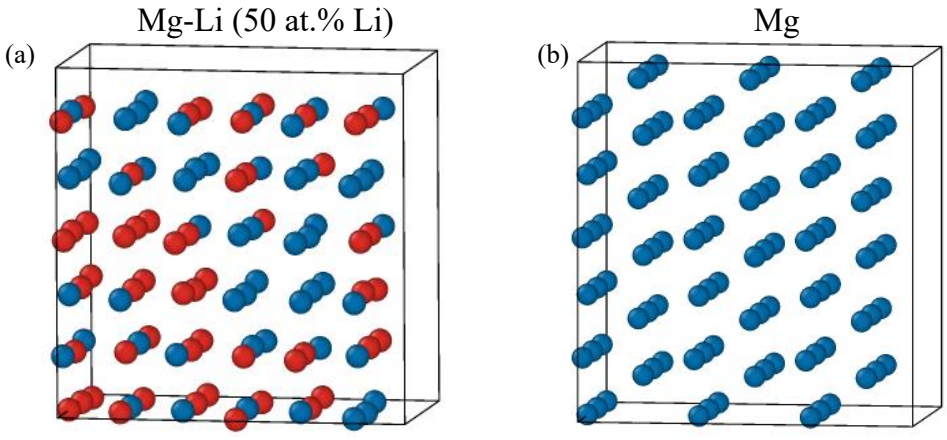

Figure A.3. Snapshots of relaxed structures of (a) Mg-50Li (at.%), and (b) pure Mg phases. Red and blue colors are used for Li and Mg atoms, respectively.

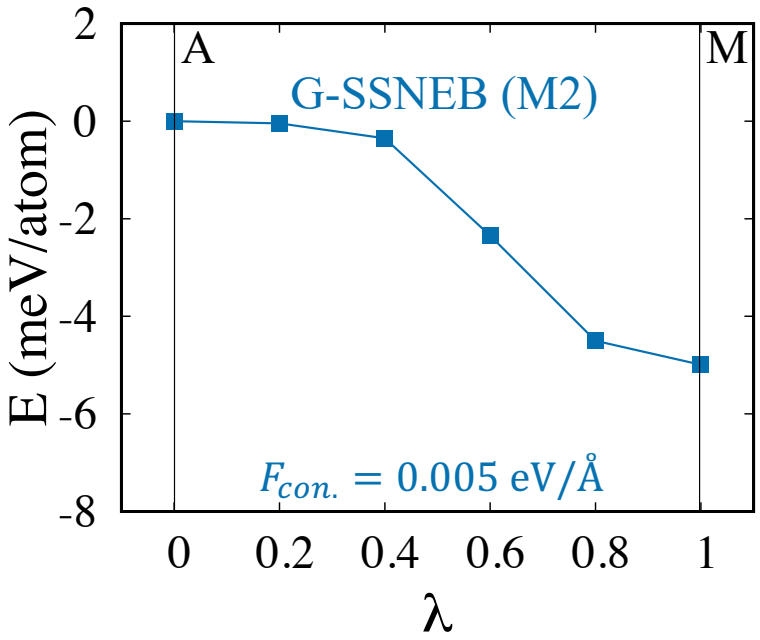

Figure A.4. Transform pathway from A to M2 (G-SSNEB) for nanolaminate containing 60% stoichiometric MgLi phase and 40% pure Mg phase with a force convergence criterion of $5X10^{-3}$ eV/Å.

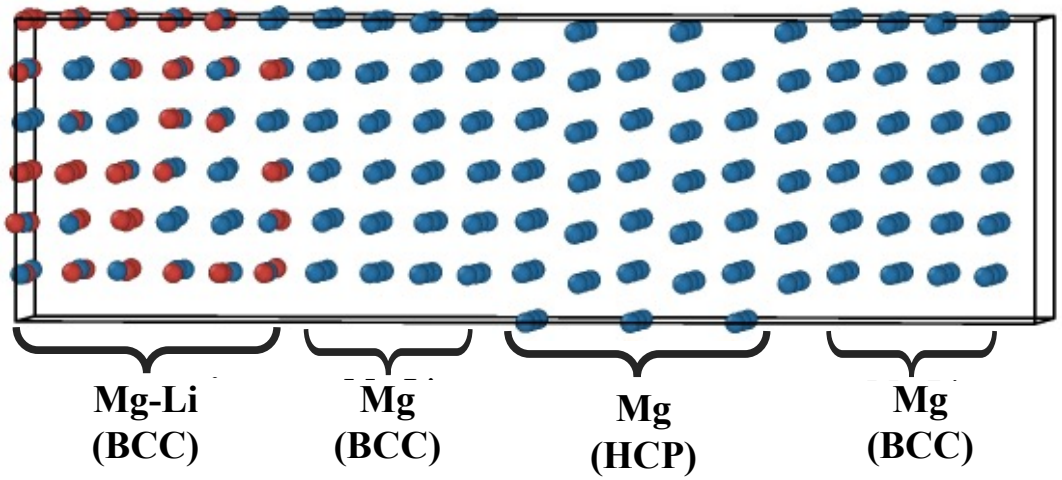

Figure A.5. Snapshot of initial structure of BCC 6Mg-Li/BCC 4Mg/HCP 6Mg/BCC 4Mg. Red and blue colors are used for Li and Mg atoms, respectively.

Table A.1. Grain index, Euler angles and grain size for all the grains. Grain size is taken as equivalent spherical diameter for same volume.

Grain Index	$\boldsymbol{\varphi}$**(°C)**	$\boldsymbol{\theta}$**(°C)**	$\boldsymbol{\Psi}$**(°C)**	**Grain Size (nm)**
1	37.9	124.5	151.5	33.1
2	66.4	87.7	43.9	29.8
3	240.4	135.8	109.3	29.8
4	185.7	78.7	111.5	38.1
5	272.3	138.6	305.7	29.8
6	86.9	49.4	89.7	28.6
7	238.8	140.7	311.9	23.9
8	290.4	37.8	36.2	34
9	50.8	138.8	324.8	33.1
10	173.8	160	234.6	31
11	204.1	86.8	140.5	36.6
12	180.1	44	86.2	31
13	131.7	112.7	13.4	36.6
14	240.3	122.7	68.5	40.2
15	111.8	19.4	265.7	27.2
16	166.4	68.7	153.6	31
17	182.4	26.6	267.7	33.1
18	270.8	86.2	333.6	29.8
19	12.6	103.8	48.6	37.4
20	250.4	125.7	172.3	42.7
21	99.3	69.4	291.1	32.1
22	182.9	57.5	95.2	29.8
23	332.6	54.4	310.7	34
24	197.6	116.4	337.3	23.9
25	289.2	87.4	220.4	33.1

26	76.8	86.4	255.4	31
27	117.1	96.4	212	28.6
28	112.8	81.4	220.6	23.9
29	10.3	119.2	101.1	31
30	184.5	152.3	141.9	37.4
31	311.3	31.5	228.2	32.1
32	21.7	115.2	271.3	39.6
33	321.1	95	18.9	31
34	223.9	91.8	256.5	27.2

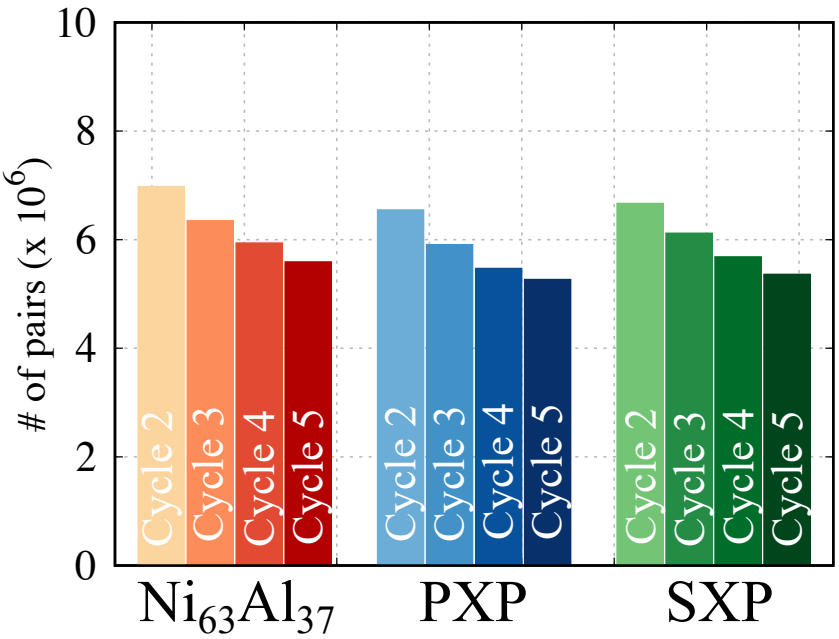

Figure A.6. Number of pairs of atoms undergoing irreversible atomic process in $Ni_{63}Al_{37}$, PXP and SXP for various loading/unloading cycles (Cycle-2 to Cycle-5) at 600 K.

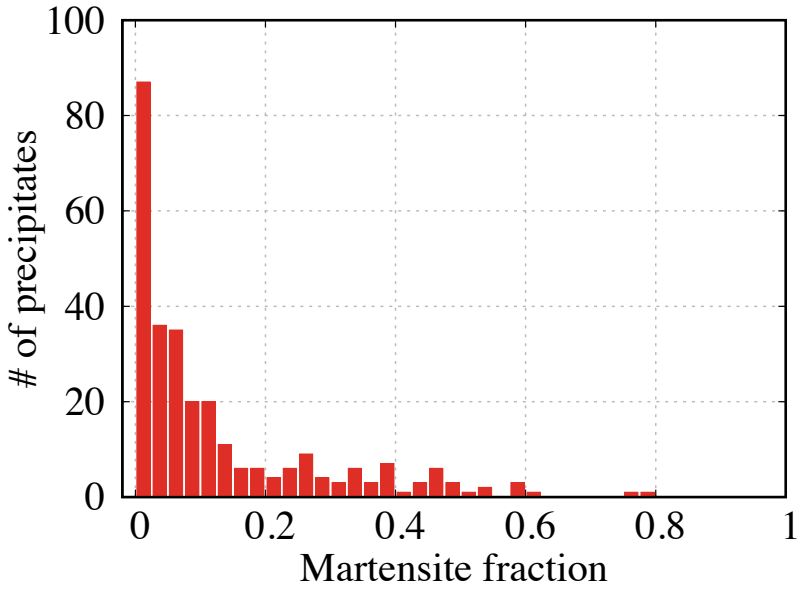

Figure A.7. Histogram of the identified martensite fraction in precipitates after fourth loading cycle of SXP.

VITA

Shivam Tripathi obtained his Ph.D. from the School of Materials Engineering at Purdue University in 2021 under the supervision of Prof. Alejandro Strachan and Prof. Michael S. Titus. Previously, he received his B.Tech in Materials Science and Engineering from the Indian Institute of Technology, Kanpur, where he graduated with the Shri Binay Kumar Sinha Award, which is given to the best undergraduate researcher working on the industrially relevant project from the entire graduating class.

During his Ph.D. at Purdue, Shivam used density functional theory and molecular dynamics based simulations to understand the tunability of martensitic transformation in shape memory alloys by incorporating a coherent second phase. Other scientific interests include thermal transport, complex concentrated alloys, and optical materials. Shivam has also been part of the experimental team during his Ph.D. and gained hands-on experience in various material fabrication and characterization methods.

In addition to Shivam's success as a researcher, including several publications and few awards during his Ph.D., Shivam has also developed several scientific tools, python notebooks, and other tutorials in the nanoHUB platform to facilitate the use and understanding of atomistic simulations to a wide range of users from undergraduate students to scientists. Following Purdue, he will join the Istituto Italiano di Tecnologia (IIT) as a post-doctoral researcher under the supervision of Prof. Michele Parrinello.

PUBLICATIONS

Journal articles:

- Shivam Tripathi, Md Mahbubul Islam, and Alejandro Strachan. "Phonon thermal transport in encapsulated copper hybrids." Journal of Applied Physics 125.4 (2019): 045106.
- Shivam Tripathi, Karthik Guda Vishnu, Michael S. Titus, and Alejandro Strachan. "Tunability of martensitic transformation in Mg-Sc shape memory alloys: A DFT study." Acta Materialia 189 (2020): 1-9.
- Shivam Tripathi, Lok C. Fan, Michael S. Titus, and Alejandro Strachan. "Automated approach to discover coherent precipitates in multi-component shape memory alloys." Computational Materials Science 197 (2021): 110651.
- Shivam Tripathi, Michael S. Titus, and Alejandro Strachan. "Martensitic transformation in superlattices of two non-transforming metals." Journal of Applied Physics 130.16 (2021): 165105.
- Shivam Tripathi, Karthik Guda Vishnu, Michael S. Titus, and Alejandro Strachan. "Uncovering the role of nanoscale precipitates on martensitic transformation and superelasticity ." Acta Materialia (under review).

Software tools:

- Random and special quasi random structure generator: Shivam Tripathi, Rileigh Anne Cotter, Sabir Utamsing, MD Mahbubul Islam, Mohsen B Kivy, Alejandro Strachan, https://nanohub.org/resources/sqsatat
- Coherent second phases in multi-component shape memory alloys (CohPhaseFind): Shivam Tripathi, Lok C. Fan, Michael S. Titus, Alejandro Strachan, https://github.itap.purdue.edu/StrachanGroup/CohPhaseFind